Intraplate basalt alkalinity modulated by a lithospheric mantle filter at the Dunedin Volcano (New Zealand)

Journal:	*Journal of Petrology*
Manuscript ID	JPET-Oct-20-0135.R2
Manuscript Type:	Original Manuscript
Date Submitted by the Author:	29-Jun-2021
Complete List of Authors:	Pontesilli, Alessio; Istituto Nazionale di Geofisica e Vulcanologia; University of Otago, Department of Geology Brenna, Marco; University of Otago, Department of Geology Ubide, Teresa; University of Queensland, School of Earth and Environmental Sciences Mollo, Silvio; Sapienza-Università di Roma, Dipartimento di Scienze della Terra, ; Istituto Nazionale di Geofisica e Vulcanologia Masotta, Matteo; Università di Pisa, Dipartimento di Scienze della Terra Caulfield, John; The University of Queensland, School of Earth and Environmental Sciences; Queensland University of Technology Central Analytical Research Facility Le Roux, Petrus; University of Cape Town, Department of Geological Sciences Nazzari, Manuela; Istituto Nazionale di Geofisica e Vulcanologia Scott, James; University of Otago, Department of Geology Scarlato, Piergiorgio; Istituto Nazionale di Geofisica e Vulcanologia
Keyword:	alkali basalts, Dunedin Volcano, thermobarometry, primary magma, lithospheric mantle filter

Intraplate basalt alkalinity modulated by a lithospheric mantle filter at the Dunedin Volcano (New Zealand)

Pontesilli A. [1, 2*], Brenna M. [2], Ubide T. [3], Mollo S. [1,4], Masotta M. [5], Caulfield J. [3,6], Le Roux P. [7], Nazzari M. [1], Scott J.M. [2], Scarlato P. [1]

[1] Istituto Nazionale di Geofisica e Vulcanologia, Via di Vigna Murata 605, 00143 Rome, Italy

[2] Department of Geology, University of Otago, PO Box 56, Dunedin 9054, New Zealand

[3] School of Earth and Environmental Sciences, The University of Queensland, Brisbane, QLD 4072, Australia

[4] Dipartimento di Scienze della Terra, Sapienza-Università di Roma, P.le Aldo Moro 5, 00185 Roma, Italy

[5] Dipartimento di Scienze della Terra, Università degli Studi di Pisa, Via S. Maria 53, 56126 Pisa, Italy

[6] Central Analytical Research Facility, Institute for Future Environments, Queensland University of Technology, 2 George Street, Brisbane, 4000, QLD, Australia

[7] Department of Geological Sciences, University of Cape Town, Rondebosch 7701, South Africa

Corresponding author:
Alessio Pontesilli
Istituto Nazionale di Geofisica e Vulcanologia,
Via di Vigna Murata 605,
00143 Rome, Italy
Email: alessio.pontesilli@ingv.it

ABSTRACT

Systematic variations in the crystal cargo and whole rock isotopic compositions of mantle-derived basalts in the intraplate Dunedin Volcano (New Zealand) indicate the influence of a complex mantle-to-crust polybaric plumbing system. Basaltic rocks define a compositional spectrum from low-alkali basalts through mid-alkali basalts to high-alkali basalts. High-alkali basalts display clinopyroxene crystals with sector (hourglass) and oscillatory zoning ($Mg\#_{61–82}$) as well as Fe-rich green cores ($Mg\#_{43–69}$), whereas low-alkali basalts are characterised by clinopyroxenes with unzoned overgrowths ($Mg\#_{69–83}$) on resorbed mafic cores ($Mg\#_{78–88}$), coexisting with reversely zoned plagioclase crystals ($An_{43–68}$ to $An_{60–84}$ from core to rim). Complex magma dynamics are indicated by distinctive compositional variations in clinopyroxene phenocrysts, with Cr-rich zones ($Mg\#_{74–87}$) indicating continuous recharge by more mafic magmas. Crystallisation of olivine, clinopyroxene and titanomagnetite occurred within a polybaric plumbing system extending from upper mantle to mid crustal depths (485–1059 MPa and 1147–1286 °C), whereas crystallisation of plagioclase with subordinate clinopyroxene and titanomagnetite proceeded towards shallower crustal levels. The compositions of high-alkali basalts and mid-alkali basalts resemble those of ocean island basalts and are characterised by FOZO-HIMU isotopic signatures ($^{87}Sr/^{86}Sr_i$ = 0.70277–0.70315, $^{143}Nd/^{144}Nd_i$ = 0.51286–0.51294, and $^{206}Pb/^{204}Pb$ = 19.348–20.265), whereas low-alkali basalts have lower incompatible element abundances and

isotopic compositions trending towards EMII ($^{87}Sr/^{86}Sr_i$ = 0.70327–70397, $^{143}Nd/^{144}Nd_i$ = 0.51282–0.51286, and $^{206}Pb/^{204}Pb$ = 19.278–19.793). High- and mid-alkali basalt magmas mostly crystallised in the lower crust, whereas low-alkali basalt magma recorded deeper upper mantle clinopyroxene crystallisation prior to eruption. The variable alkaline character and isotope composition may result from interaction of low-alkaline melts derived from the asthenosphere with melts derived from lithospheric mantle, possibly initiated by asthenospheric melt percolation. The transition to more alkaline compositions was induced by variable degrees of melting of metasomatic lithologies in the lithospheric mantle, leading to eruption of predominantly small-volume, high-alkali magmas at the periphery of the volcano. Moreover, the lithosphere imposed a filtering effect on the alkalinity of these intraplate magmas. As a consequence, the eruption of low-alkali basalts with greater asthenospheric input was concentrated at the centre of the volcano, where the plumbing system was more developed.

Keywords: alkali basalts; Dunedin Volcano; thermobarometry; primary magma; lithospheric mantle filter

INTRODUCTION

Understanding the petrological and geochemical characteristics of basaltic products in intraplate volcanic systems is crucial for constraining source regions and the processes responsible for primary melt segregation at mantle depths, as well as for elucidating the differentiation and evolution of continental alkaline magmas. Despite their limited volume compared to subalkaline rocks, alkaline basalts can provide significant insights on primary magma differentiation processes (e.g. Green, 1973; Morse, 1980; Farmer, 2003; Mallik & Dasgupta, 2012; Pilet et al., 2015; Brenna et al., 2021).

Significant compositional heterogeneity has been shown to characterise mantle-derived magmas erupted at intraplate volcanic systems, which include basanites, nephelinites, alkali basalts and transitional to subalkaline basalts (Cook et al., 2005; McGee et al., 2012; Boyce et al., 2015; Scott et al., 2020a). The mafic diversity represents the parental compositions of single or multiple liquid lines of descent and is ultimately responsible for the diversity of magma types characterizing alkaline suites (e.g. Wright, 1971; Panter et al., 1997; White et al., 2012; Lucassen et al., 2013; Brenna et al., 2014; Wolff, 2017). Such complexity results from processes occurring in the mantle source and in the volcanic plumbing system, which extends from the Moho to shallow crustal depths (e.g. Bondi et al., 2002; Brenna et al., 2015; Jankovics et al., 2015; Giacomoni et al., 2016; Kim et al., 2019). Reconstruction of mineral-melt equilibria is pivotal to understand the primary signature of basaltic magmas, as deep differentiation processes may occur in alkaline basalts at lithospheric to near-Moho depths (e.g., Wilson et al., 1995; Orejana et al., 2007; Smith et al., 2008; Re et al., 2017).

The Dunedin Volcano, in South Island, New Zealand, is a classic location in which some of the early concepts on liquid lines of descent of intraplate alkaline systems were originally proposed (Coombs & Wilkinson, 1969; Price & Chappell, 1975). Variable

fractionating assemblages and degrees of magma mixing/crustal contamination have been proposed to result in different evolutionary suites (Price & Taylor, 1973; Price & Chappell, 1975). Olivine, clinopyroxene and titanomagnetite are the main fractionating phases in magmas from the less silica undersaturated series, whereas stabilization of amphibole at higher pressures and melt-H_2O contents may account for the geochemical variability of the more silica undersaturated magmas (Price & Taylor, 1973). Amphibole is typically not observed in basaltic lavas at the Dunedin Volcano, although it is quite common in the more evolved products with undersaturated affinity and compositions ranging from mugearite to phonolite (Price & Chappell, 1975). It is likely that basaltic magmas were H_2O-undersaturated, although amphibole could have stabilised in intermediate magmas following crystallisation and water saturation. Different degrees of silica saturation and variable alkali contents characterise basanites to basalts, as well as the more evolved phonolites and trachytes (Coombs & Wilkinson, 1969; Price & Chappell, 1975; Coombs et al., 1986, 2008; Scott et al., 2020a). Multiple parental magma compositions have been postulated to account for the observed chemical variability of intermediate to evolved magmas, that include both silica saturated and undersaturated series (Coombs & Wilkinson, 1969), although the mechanisms modulating the compositional variability of mantle-derived magmas has remained largely unexplored.

In this study, we combine textural and mineral chemistry data with whole rock elemental and Sr-Nd-Pb isotopic compositions, with the aim of elucidating the magmatic processes that produced low- to high-alkali basalts, trachybasalts and basaltic trachyandesites at the Dunedin Volcano. Results from thermobarometric and geochemical models are used to better define the mechanisms controlling magma dynamics and constrain the volcanic plumbing architecture. In addition, we explore the melt generation processes taking place at

the asthenosphere-lithosphere transition and those responsible for the change in basalt alkalinity.

GEOLOGICAL OUTLINE

The Dunedin Volcano, with its estimated ~600 and ~150 km^3 of intruded and erupted materials, respectively, belongs to the wider Dunedin Volcanic Group (Reilly et al., 1972; Coombs et al., 1986; Scott et al., 2020a). This encompasses the vast volume of intrusive and volcanic rocks constituting the central volcanic edifice as well as scattered outlying centres distributed over ~8000 km^2 in East Otago. The outlying centres, formerly known as Waipiata Volcanics, are mostly monogenetic, and consist of lava flows, pyroclastic products, dykes, and sills of dominantly basanitic composition produced between 25 and 9 Ma (Coombs et al., 1986; Hoernle et al., 2006; Coombs et al., 2008; Scott et al., 2020a). The Dunedin Volcano itself represents by far the single most important centre, in which extensive and prolonged activity from 16 to 11 Ma (McDougall and Coombs, 1973; Hoernle et al. 2006; Coombs et al., 2008; Scott et al., 2020a) resulted in a composite volcano forming the current Otago Peninsula (Fig.1). A gravity anomaly surrounding the locality of Port Chalmers has been interpreted as the central area of the volcano (Reilly, 1972). The offshore occurrence of volcanic deposits in the vicinity of the Dunedin Volcano has been indicated by seismic studies (Gorman et al., 2013).

The erupted products span a wide compositional range from basanite to phonolite and trachyte, with the primitive magmas mainly forming lava flows and dykes and the differentiated end-members cropping out as lava domes or pyroclastic tuffs and breccias (Price & Coombs, 1975; Price et al., 2003). The basaltic rocks are estimated to be volumetrically dominant, although a few large phonolite and trachyte eruptions also occurred,

with estimated volumes of less than 20 km^3 (Price, 1972; Coombs et al., 1986; Martin, 2000; Price et al., 2003; Scott et al., 2020a). Significant accumulation of magmatic intrusions at lower to upper crustal depths has been inferred from geophysical and petrological xenolith-based studies (Godfrey et al., 2001; Price et al., 2003).

SAMPLING AND ANALYTICAL METHODS

Samples were selected to include the most primitive lavas and dykes cropping out at the Dunedin Volcano (Fig. 1). Petrographic features were first examined in thin section and samples further selected for microchemical investigation. Relative abundances of phenocrysts were estimated by measuring the phenocryst area in digitised images (Table 1). Microanalytical work focused on pre-eruptive processes recorded in minerals, hence thin sections were prepared from crystal-rich surfaces of the samples. In contrast, crystals were avoided when preparing aliquot samples for whole-rock geochemistry, which aimed to explore melt compositional variations of erupted melts.

Microchemical data were obtained by electron probe micro-analysis (EPMA) using a JEOL JXA 8200 with combined energy dispersive and wavelength dispersive systems (five spectrometers with twelve crystals) installed at the HP-HT (High Pressure - High Temperature) Laboratory of Experimental Volcanology and Geophysics of the Istituto Nazionale di Geofisica e Vulcanologia (INGV) in Rome, Italy. Carbon-coated thin sections were analysed under accelerating voltage and beam current of 15 kV and 10 nA, respectively. The beam size was 5 μm with a counting time of 20 and 10 s on peak and background positions, respectively. Corrections for inter-elemental effects were made using a ZAF (Z, atomic number; A, absorption; F, fluorescence) procedure. The following standards were adopted for the various major elements: jadeite (Si and Na), corundum (Al), augite (Ca), forsterite (Mg), andradite (Fe), rutile (Ti), orthoclase (K), barite (Ba), apatite (P), spessartine

(Mn) and JEOL Cr metal (Cr). Sodium and potassium were analysed first to minimize alkali migration. Analytical precision was measured through well-characterised synthetic oxides and minerals. Data quality was ensured by analysing test materials as unknowns following the method of Iezzi et al. (2014). Based on counting statistics, analytical uncertainties relative to their reported concentrations indicate that precision (2 standard deviations) is better than 9% for all elements analysed.

Trace element analyses of clinopyroxene crystals were performed by Laser Ablation Inductively Coupled Plasma Mass Spectrometry (LA-ICP-MS) at the University of Queensland Centre for Geoanalytical Mass Spectrometry, Radiogenic Isotope Facility (UQ RIF-lab). We used an ASI RESOlution 193 nm excimer UV ArF laser ablation system with a dual-volume Laurin Technic ablation cell and GeoStar Norris software, coupled to a Thermo iCap RQ quadruple mass spectrometer with Qtegra software. Ultrapure He was used as carrier gas, with Ar and trace amounts N_2 added just after the ablation cell to aid in plasma stabilization and analytical sensitivity. NIST612 glass reference material was used as calibration standard and Ca concentrations (previously analysed by EPMA) as internal standard. Accuracy and precision were monitored by analysing BHVO-2G standard as quality monitor, and these analyses are reported in Table S1 as a Supplementary Data. Precision (2 standard deviations) was better than 8% for all elements analysed, and accuracy was better than 5-10% and for all elements except Ni (better than 12%). Elemental maps were acquired following the line rastering technique of Ubide et al. (2015), using a spot size of 20 µm, and a rastering speed of 20 µm/s (more details on gas flows and instrument parameters in Ubide et al., 2019). Data reduction was carried out with Iolite v2.5 (Paton et al., 2011) in quantitative mode. Average compositional data were extracted from crystals and crystal zones using Monocle (Petrus et al., 2017).

Clean rock specimens were crushed into chips and ground in a tungsten carbide mill for whole rock analysis. Major elements were measured by X-Ray Fluorescence (XRF) at ALS Minerals in Brisbane through a Bruker S4 Pioneer system, along with loss on ignition, which was measured using standard furnace techniques, by calculating the difference in sample weights measured at 105 °C and 1000 °C. Fused disks made of dried sample powders and lithium tetraborate ($Li_2B_4O_7$) were dissolved in a mixture of HNO_3, HCl, and HF. Trace elements were measured by ICP-MS at ALS Minerals using a Perkin–Elmer Elan 9000 system. The quality of the whole rock data was checked against in-house standards and duplicates processed as unknowns by ALS Minerals (accuracy and precision reported in Table S2). Independent testing of data reproduction indicates that the method yielded satisfactory results, with precision (2 standard deviations) better than 9% for all elements with concentrations above 1 wt.% and better than 11% for most minor and trace elements.

All isotope data were obtained using a Nu instruments NuPlasma HR mass spectrometer in the MC-ICP-MS facility housed in the Department of Geological Sciences, University of Cape Town, Rondebosch, South Africa. The Sr, Nd, and Pb isotopic compositions of whole rock samples were measured using laboratory and analytical procedures reported in Harris et al. (2015). For each sample, a total of approximately 50 mg of rock powder was dissolved in a 4:1 HF/HNO_3 acid mixture in sealed Teflon beakers at 140 ºC, dried down after 48 h. Subsequently, conversion to nitrates was conducted in a concentrated HNO_3 solution in sealed Teflon beakers at 140 °C for 1 h. Sr, Nd, and Pb fractions for isotope analysis were isolated employing sequential column chemistry (Pin et al. 1994, 2014). Sr elemental fractions were analysed as 200 ppb 0.2% HNO_3 solutions, and all data were normalised to a value of 0.710255 for the bracketing analyses of NIST SRM987, adopted as the reference material. During analysis, Sr isotope data were corrected for Rb interference using the measured signal for ^{85}Rb and the natural $^{85}Rb/^{87}Rb$ ratio, while

instrumental mass fractionation was addressed using the exponential law and an $^{86}Sr/^{88}Sr$ value of 0.1194. The Nd elemental fractions were analysed as 50 ppb 2% HNO_3 solutions using a Nu Instruments DSN-100 desolvating nebuliser, and resulting data were normalised to a value of 0.512115 for bracketing analyses of Jndi-1 reference material, after Tanaka et al. (2000). All Nd isotope data were corrected for Sm and Ce interference using the measured signals for ^{147}Sm and ^{140}Ce along with natural isotopic abundances of Sm and Ce. Instrumental mass fractionation was addressed using the exponential law and a $^{146}Nd/^{144}Nd$ value of 0.7219. Pb elemental fractions were analysed as 50 ppb 2% HNO_3 solutions using Nu Instruments DSN-100 desolvating nebuliser. Aliquots of NIST SRM997 Tl standard were added to all standards and samples analysed to give ±10:1 Pb:Tl ratios. NIST SRM981 was adopted as the calibration standard, with $^{208}Pb/^{204}Pb$, $^{207}Pb/^{204}Pb$, and $^{206}Pb/^{204}Pb$ reference values of 36.7219, 15.4963 and 16.9405 (Galer and Abouchami, 1998), respectively. Frequent on-peak background measurements were used to correct all Pb isotope data for Hg interference. Instrumental mass fractionation of the measured Pb isotope ratios was corrected using the reference $^{205}Tl/^{203}Tl$ value of 2.3889 and the exponential law. For all isotopic ratios, the precision is given as 2σ errors in the last significant digits; accuracy was tested by using BHVO-2 as quality monitor against values after Weis et al. (2006). Accuracy is better than 0.1% for all isotopic ratios except $^{208}Pb/^{204}Pb$ and $^{206}Pb/^{204}Pb$, with accuracies slightly better than 0.2 and 0.5 %, respectively (Table S3).

ROCK CLASSIFICATION

The total alkali vs. silica (TAS) diagram (Le Maitre et al., 2002) shows that our samples are mostly basalts and trachybasalts (Fig. 2a). A few samples fall beyond these fields, and are classified as basanites, tephrites and basaltic trachyandesites (hawaiites). These

compositions correlate with olivine alkali basalts, basanites and nepheline trachyandesites or hawaiites as originally described by Coombs & Wilkinson (1969) and Price & Chappell (1975). In order to make a clearer distinction between samples characterised by different alkalinity (Table 1), whole rock compositions were classified to an alkali index [alkali index = $(Na_2O+K_2O)/SiO_2$ wt.%] (Fig. 2b) as follows: alkali index > 0.1 for high-alkali basalts, 0.1 ≥ to > 0.08 for mid-alkali basalts and ≤ 0.08 for low-alkali basalts. We adopted this alkali index as it best captures the distinction of whole rock compositions coupled with petrographic characteristics (see below). These compositions represent the overall range of the least evolved eruptive products at Dunedin Volcano (see Scott et al., 2020a for a complete data set). High-alkali basalts constitute the larger group of samples and display the broader compositional variations in terms of major elements (Fig. 2a, b), including basanites, alkali basalts, trachybasalts and less evolved mugearites, with SiO_2 and Mg# ranging from 46.2 to 51.2 wt.% and from 35 to 60, respectively. Mid-alkali basalts are dominantly basaltic in composition, with SiO_2 and Mg# ranging from 44.8 to 49.0 wt.% and from 41 to 63, respectively. Low-alkali basalts are the most Mg-rich compositions, with SiO_2 and Mg# ranging from 45.2 to 50.4 wt.% and from 52 to 66, respectively. High-alkali basalts dominate in the periphery of the Dunedin Volcano edifice, becoming more evolved (Table 1) towards its centre. Mid-alkali basalts are dominantly found towards the interior of the volcano, in the Otago Peninsula. Low-alkali basalts are exclusively found in the Otago Peninsula (Fig. 1).

PETROGRAPHY AND MINERAL CHEMISTRY

Petrography

Lavas and dykes are porphyritic and composed of mm-long phenocrysts of olivine, clinopyroxene and Fe-Ti oxides in a μm-sized groundmass consisting of olivine,

clinopyroxene, plagioclase, and Fe-Ti oxides (Fig. 3). A summary of phenocrysts occurrence and modal abundance by crystal population in each sample can be found in Table 1, where samples are distinguished as three main groups based on whole rock compositions and petrographic characteristics. Vesicularity is invariably very low (<1%) in all lava samples.

High-alkali basalts are characteristically porphyritic (phenocryst abundance ranging from 13 to 27 vol.%; Table 1) with clinopyroxene and olivine occurring both as single phenocrysts and as glomerocrysts (Fig. 3a, b). Fe-Ti oxides are found both as subordinate phenocrysts (usually with modal abundance < 1 vol.%) or as inclusions in clinopyroxene phenocrysts. Olivine crystals are euhedral to subhedral, with maximum lengths reaching 1 mm, and they contain scarce Fe-Ti oxide inclusions. Clinopyroxene occurs as euhedral to subhedral crystals, pale-pinkish to gray and usually not exceeding a few millimeters in length. This phase is typically characterised by complex zoning, showing prominent oscillatory and sector (hourglass) zones (Fig. 3b). Resorbed and typically small clinopyroxene cores of pale green color are occasionally found in some of the high-alkali basalts (see Table 1). Slightly more evolved high-alkali basalts (trachybasaltic in compositions) are petrographically similar to less evolved high-alkali basalts, although the phenocryst assemblage differs slightly with a lower abundance of olivine and a higher abundance of plagioclase (sometimes with sieve-textured cores) and clinopyroxenes with pale green cores (Fig. 3c; Table 1). The groundmass of high-alkali basalts is made up of plagioclase, clinopyroxene, oxides, and olivine, in order of decreasing abundance. Apatite and rare sulfide globules are accessory phases found as inclusions, with apatite also present in the groundmass. Rare spinel lherzolite xenoliths occur exclusively in high-alkali basalts (samples DVB1a, DVB1b, and DVB3).

Low-alkali basalts are highly porphyritic (33 to 47 vol.% phenocrysts; Table 1) and contain a mineral assemblage composed, in order of abundance, of clinopyroxene, olivine,

plagioclase, and oxides (Fig. 3d). Olivine phenocrysts are usually subhedral and large, up to a few millimeters in length, and show some alteration to red-brown oxides. Clinopyroxenes are large (up to several mm), subhedral to anhedral phenocrysts with either pinkish gray or pale gray cores, commonly overgrown by pinkish gray mantles and rims, but without oscillatory zonation (Fig. 3d). Pale gray clinopyroxene cores are typically rounded and contain few small oxide and apatite inclusions, whilst pinkish gray clinopyroxene cores are characterised by spongy textures (Fig. 3d, e). Plagioclase is always present as euhedral to subhedral phenocrysts, with maximum lengths of a few millimeters. Plagioclase phenocrysts commonly display rounded cores surrounded by sieve-textured mantles, overgrown by euhedral outer rims (Fig. 3f). The size of oxide phenocrysts does not exceed 0.5 mm. Tiny oxide inclusions are also common. The groundmass consists of clinopyroxene, olivine, plagioclase, and oxides.

Mid-alkali basalts are more heterogeneous in texture, showing characteristics intermediate between high- and low-alkali basalts, and phenocryst abundances ranging from 18 to 39 vol.% (Fig. 3g and Table 1). The modal content of plagioclase phenocrysts varies from 0 to ~15 vol.%. Olivine is found either as individual large subrounded phenocrysts (as in low- alkali basalts), small (around 1 mm) euhedral crystals, and mono- or bi-mineralic glomerocrysts (in association with clinopyroxene). Clinopyroxene is subhedral to euhedral, and commonly shows oscillatory and sector (hourglass) zoning. Glomerocrysts are also found, as for the case of high-alkali basalts. Large, unzoned, and more equant phenocrysts occur in association with pale gray rounded and resorbed cores (Fig. 3g, h), with lengths typically less than 1 mm.

Mineral chemistry

307 *Olivine*

308 Two distinct olivine populations have been identified on a compositional basis. Type 1
309 olivine is common in most of the samples and has homogeneous cores (Fig. 4a) with Mg-rich
310 compositions (Fo_{81-87}) and CaO > 0.15 wt.% (Fig. 5). Crystals commonly exhibit outer rims
311 with thicknesses of a few tens of microns and Fo-poor compositions (Fo_{55-75}). Type 2 olivine
312 is common in low-alkali basalts and, to a lesser extent, in mid- and high-alkali basalts. It is
313 characterised by relatively Fo-poor compositions (Fo_{73-81}) and CaO of 0.15-0.40 wt.% (Fig.
314 4a, Fig. 5). In some cases, type 2 crystals exhibit Fo enrichments from core to rim (Fig. 4a),
315 with only outer rim compositions that overlap those of olivine type 1 rims (Fo_{55-75}). Olivine
316 compositional data are included in Table S4.

317

318 *Clinopyroxene*

319 Clinopyroxene crystals have been categorised into four main populations on the basis
320 of textural and compositional characteristics: type 1 sector and oscillatory zoned
321 clinopyroxene crystals and mantles, type 2 green cores, type 3 resorbed relic cores, and type 4
322 unzoned clinopyroxene crystals and mantles (Table 1, Fig. 4b-e). Further distinctions relate to
323 Cr-rich zones and overgrowth rims not featuring disequilibrium textures and common across
324 all types of clinopyroxene phenocrysts.

325 Type 1 clinopyroxenes are sector and oscillatory zoned crystals (Fig. 4b) found in high-
326 alkali basalts and subordinately in mid–alkali basalts (Fig. 4b), whereas they are absent in
327 low-alkali basalts. Crystals have diopsidic to augitic compositions with $Wo_{42–52}En_{33–45}Fs_{9–30}$
328 (where Wo, En and Fs stand for wollastonite, enstatite and ferrosilite, respectively). The Mg–
329 number [Mg# = molar 100 × Mg / (Mg + Fe^{2+}) where Fe^{2+} expresses total iron] ranges from
330 65 to 82 and is inversely correlated with Al_{tot} (0.11–0.53 apfu) and Ti (0.02–0.14 apfu) (Fig.

6). The sum of Tschermak components (∑Ts = CaTi–Tschermak + CaFe–Tschermak + CaCr–Tschermak) decreases ($\sum Ts_{0.04–0.24}$) with increasing diopside content ($Di_{0.41–0.66}$), while slight changes in hedenbergite are observed ($Hd_{0.11–0.26}$). Sector and oscillatory zoning are associated with large variations in rare earth element (REE) abundances in type 1 clinopyroxenes (Fig. 7 and Fig. 8), with La, Eu and Yb of 3.9–17.8, 1.3–3.8, and 0.9–3.2 ppm, respectively. The same applies to some moderately compatible to incompatible elements such as Sr and Zr, with concentrations ranging from 69 to 246 ppm and from 51 to 326 ppm, respectively (Fig. 8). Cr and Ni display strong concentric zoning in clinopyroxene (Fig. 8), with Cr abundance up to 5000 ppm.

Type 2 clinopyroxenes are found in high- and mid-alkali basalts (Table 1) and are represented by unzoned green cores (Fig. 3c) with augitic compositions ($Wo_{43–46}En_{22–36}Fs_{18–37}$) and $Mg\#_{43–69}$ (Fig. 6). Concentrations of Al (0.03–0.23 apfu) and Ti (0.01–0.05 apfu) are invariably low. Tschermak ($\sum Ts_{0.01–0.10}$) and diopside ($Di_{0.32–0.55}$) components are also low, whereas hedenbergite ($Hd_{0.23–0.50}$) contents are markedly high (Fig. 7). REE abundances are consistently higher in the green cores with respect to types 1 and 3 (Fig. 7 and Fig. 8), with La and Yb contents of 7.0–24.9 ppm and 2.3–5.5 ppm, respectively. In contrast, Eu concentrations are lower (0.6–3.5 ppm). Zr (49–272 ppm) and Sr (70–148 ppm) abundances are comparable to those of other clinopyroxene populations (Fig. 7). Ni (5–70 ppm) and Cr (1–107 ppm) contents are invariably low (Fig. 7 and Fig. 8). The green cores are overgrown by mantles characterized by sector and oscillatory zoning, with diopsidic to augitic compositions ($Wo_{44–51}En_{36–44}Fs_{11–28}$), $Mg\#_{65–81}$, Al 0.12–0.47 apfu, Ti 0.02–0.12 apfu (Fig. 6) and clinopyroxene end–member components spanning: $\sum Ts_{0.05–0.22}$, $Di_{0.36–0.54}$ and $Hd_{0.24–0.46}$. The texture and composition of mantles overgrowing type 2 (green) clinopyroxene resemble type 1 crystals in the same samples, and are defined as type 1 mantles hereafter. Zoning in type 1 mantles is associated with variations in REE abundances, with La, Eu and Yb ranging

356 at 4–17, 1.8–3.2 and 1.8–2.8 ppm, respectively. Significant variations are observed also in Zr
357 (80–234 ppm), Sr (74–134 ppm), Cr (84–1143 ppm) and Ni (87–136 ppm) (Fig. 7).

358 Type 3 clinopyroxene cores exhibit the most magnesian compositions ($Wo_{44–49}En_{39–}$
359 $_{48}Fs_{7–15}$) among the studied phenocrysts and are found in low-alkali basalts and, to a minor
360 extent in some mid–alkali basalts. Type 3 crystals are represented by resorbed cores and an
361 overall uniform composition (Fig. 4d). The value of Mg# ranges from 78 to 88, whereas Al_{tot}
362 (0.17–0.33 apfu) and Ti (0.02–0.05 apfu) have very low concentrations (Fig. 6). Tschermak
363 ($\sum Ts_{0.08–0.15}$) and hedenbergite ($Hd_{0.09–0.16}$) components are low, whereas diopside is high
364 ($Di_{0.54–0.67}$). REE concentrations are the lowest observed, with La and Yb contents of 1.4–5.1,
365 0.6–1.4 and 0.5–3.1 ppm, respectively. Type 3 clinopyroxenes are also depleted in other
366 incompatible elements (e.g., Sr and Zr) and strongly enriched in compatible Cr (940–7362
367 ppm) and Ni (137–243 ppm). Type 3 resorbed cores are overgrown by more augitic mantle
368 compositions ($Wo_{43–51}En_{35–47}Fs_{8–19}$) that have $Mg\#_{69–83}$, Al 0.11–0.42 apfu and Ti (0.02–0.10
369 apfu. are lower in Diopside and higher in Tschermack and Hedenbergite components than the
370 resorbed cores, with $\sum Ts_{0.06–0.18}$, $Di_{0.40–0.55}$ and $Hd_{0.21–0.42}$. REE abundances are higher than in
371 resorbed cores, with La, Eu and Yb contents of 3–12 ppm, 1.0–2.1 ppm and 1.1–1.9 ppm,
372 respectively. Zr (47–77 ppm) and Sr (58–111 ppm) are higher than in the resorbed cores,
373 while mantle compositions are characterized by lower abundances of Cr (47–1415 ppm) and
374 Ni (87–136 ppm). Mantle compositions overgrowing type 3 cores are analogous to type 4
375 clinopyroxene crystals, and are similarly characterized by relatively uniform internal
376 compositions, with no sector and oscillatory zoning (Fig. 4; Fig. 6; Fig. 7). Therefore,
377 mantles overgrowing type 3 resorbed cores are defined as type 4 mantles hereafter.

378 Type 4 clinopyroxenes are found in low- and mid-alkali basalts and span a wide
379 compositional range ($Wo_{43–51}En_{35–47}Fs_{8–19}$), including Mg–rich compositions ($Mg\#_{69–84}$).
380 Type 4 clinopyroxenes display more chemical homogeneity with respect to type 1, with a

large number of unzoned crystals (Fig. 4e and Fig. 8). Al (0.10–0.51 ppm) and Ti (0.03–0.12 apfu) concentrations are lower than in type 1 clinopyroxenes (Fig. 7). Slightly higher diopside ($Di_{0.43–0.66}$) and lower Tschermak ($\sum Ts_{0.04–0.21}$) and hedenbergite ($Hd_{0.11–0.23}$) components distinguish type 4 from type 1 (Fig. 7). Type 4 clinopyroxenes are analogous to mantle compositions overgrowing type 3 resorbed cores, REE and incompatible element concentrations are generally intermediate between those found in types 1 and 3, with La, Eu, Yb, Sr, and Zr abundances of 1.9–11.1, 0.8–2.7, 0.7–2.9, 47–190, and 32–152 ppm, respectively. Conversely, Cr (47–3419 ppm) and Ni (2–170 ppm) concentrations in type 4 are, on average, lower than those measured in types 1 and 3 (Fig. 8).

Chromium–rich zones are mostly observed towards the rim of types 1 and 4. The Cr–rich zones have overall similar compositional features to each other regardless of clinopyroxene crystals they overgrow, with $Wo_{44–50}En_{35–48}Fs_{7–20}$ and $Mg\#_{74–87}$ (Fig. 6). In terms of major elements, Cr–rich zones resemble the compositions of type 3 resorbed cores, with high diopside ($Di_{0.48–0.66}$) and low hedenbergite ($Hd_{0.09–0.20}$) components. Nonetheless, Cr–rich zones are characterised by generally higher and more variable Al (0.15–0.41 apfu) and Ti (0.02–0.11 apfu) concentrations. The Tschermak ($\sum Ts_{0.06–0.21}$) components are comparable to those of types 1 and 4 clinopyroxenes (Fig. 7). In terms of trace elements, these crystal portions are strongly enriched in Cr (364–5727 ppm) and Ni (59–237 ppm). Incompatible trace element concentrations are higher, on average, than those in types 3 and 4, with La, Eu, Yb, Sr, and Zr contents of 1.7–15.3, 0.7–2.9, 0.6–2.5, 50.4–187.9, and 26.6–237.4 ppm (Fig. 7). This contrasts with type 1 crystals, which are typically enriched in the same elements with respect to Cr–rich zones (Fig. 8).

Overgrowth rims, observed in all types of clinopyroxene, display a broad compositional range, with $Wo_{42–51}En_{27–45}Fs_{13–33}$ and $Mg\#_{63–81}$. Al 0.06–0.44 apfu, Ti 0.03–0.13 apfu, and Tschermak components ($\sum Ts_{0.03–0.20}$) that resemble those of type 1 and type 4 (Fig. 6 and Fig.

7). The same applies to diopside ($Di_{0.45–0.64}$) and hedenbergite ($Hd_{0.16–0.30}$) contents. REE and other incompatible element concentrations are comparable to (or even higher than) those of type 2 green cores, with La, Eu, Yb, Sr, and Zr of 2.9–33.2 ppm, 0.7–2.9 ppm, 0.9–4.1 ppm, 1.0–5.5 ppm, 50–188 ppm, and 27–237 ppm (Fig. 7). Cr (13–2155 ppm) and Ni (52–158 ppm) contents are lower than those of type 1, 3, and 4, but they are invariably higher than compatible trace cations in type 2 (Fig. 7 and Fig. 8). Clinopyroxene major and trace element data are included in Table S5 and in Table S6, respectively.

Fe–Ti Oxides

Oxides consist of titanomagnetite and rare ilmenite. For titanomagnetite, total FeO (FeO^T) and TiO_2 are in the ranges of 61.3–71.6 wt.% and 15.6–25.4 wt.%, 59.7–68.4 wt.% and 19.8–29.3 wt.%, 56.7–67.9 wt.% and 21.2–30.5 wt.%, in high–, mid– and low–alkali basalts, respectively. A slight increase in ulvospinel (Usp) content is related to a decrease in alkalinity of the host rocks, with $Usp_{0.44–0.79}$ in high–alkali basalts, $Usp_{0.58–0.91}$ in mid–alkali basalts, and $Usp_{0.59–0.95}$ in low–alkali basalts (Fig. 9).

Ilmenite phenocrysts, which are rare and associated with titanomagnetite (but only in high– and low–alkali basalts), have FeO^T and TiO_2 of 41.7–51.4 wt.% and 39.7–54.3 wt.%, respectively. Oxide compositional data are included in Table S7.

Plagioclase

Plagioclase phenocrysts, although not present in all samples, cover a wide compositional range from bytownite to andesine (Fig.10). Three types of plagioclases have

been recognised on the basis of crystal composition (anorthite content) and texture (type of zoning). Type 1 plagioclase (Fig. 4f), characterising mid- and low-alkali basalts (Table 1), is typically reversely zoned. The anorthite (An) content of the crystal cores is $An_{43–68}$. Overgrowth rims develop around sieve–textured mantles with compositions of $An_{60–84}$ (Fig. 4f). Type 2 plagioclase (Fig. 4g) occurs in more evolved high–alkali basalts and is characterised by oscillatory zoning, usually accompanied by an overall decrease in anorthite ($An_{40–78}$; Fig.10) from core ($An_{53–78}$) to rim ($An_{40–67}$). Type 3 plagioclase is very rare and found only in the more mafic high–alkali basalts (Table 1). This type exhibits the most calcic composition ($An_{71–88}$) and is found in strongly resorbed crystals (Fig.10). FeO, MgO and TiO_2 do not show significant core to rim variations, ranging in all plagioclase types from 0.2–0.7, 0–0.2 and 0–0.2 wt.%, respectively. Plagioclase compositional data are included in Table S8.

WHOLE ROCK GEOCHEMISTRY

Major elements

Major element analyses for 22 basaltic samples are listed in Table 2 and compositions are shown in selected variation diagrams of major oxides vs. Mg# (Fig. 11). It is apparent that Al_2O_3, Na_2O and K_2O abundances increase progressively with decreasing Mg# from low- to high-alkali basalts. In contrast, CaO in high-alkali basalts is slightly lower than that measured in low- and mid-alkali basalts; this trend becomes more evident in comparison with Dunedin Volcano literature data (Fig. 11). TiO_2 and FeO^T contents do not show clear variations in basalts, but their concentrations decrease in more differentiated products (Mg# < 30). Low-alkali basalts are mostly hypersthene-normative, while mid- and high-alkali basalts are progressively more nepheline-normative (Table 2).

453

454 **Trace elements**

455 Trace element concentrations for the 22 samples are listed in Table 2 and data are
456 plotted in selected variation diagrams of trace elements vs. Mg# (Fig. 12). Cr and Ni
457 abundances are higher in low- and mid-alkali basalts than in high-alkali basalts. Sr, Zr and
458 REE abundances increase from low- to mid- to high-alkali basalts. No significant Eu
459 anomalies are evident in any of the samples. Primitive Mantle-normalised trace element
460 concentrations (Fig. 13a) strongly resemble those of ocean island basalts (OIB; e.g.
461 McDonough & Sun, 1995). An increase in incompatible trace element concentrations is
462 observed from low- to mid- to high-alkali basalts, and this trend is more pronounced for LILE
463 (Large Ion Lithophile Elements; e.g., Rb_N and Ba_N of 25–82 and 30–110, respectively),
464 HFSE (High Field Strength Elements; e.g., Nb_N and Th_N of 40–139 and 37–124,
465 respectively), and LREE (Light REE; e.g., La_N and Ce_N of 32–115 and 25–85, respectively).
466 HREE (Heavy REE; e.g., Yb_N of 3.6–6.9) and some selected LILE (e.g., Sr_N of 25–54) and
467 HFSE (e.g., Ti of 11–20) are more enriched in high-alkali basalts compared to low-alkali
468 basalts (Fig. 13a). Relative depletions in K and Ti are increasingly evident from low- to mid-
469 to high-alkali basalts. Low-alkali basalts and some mid-alkali basalts have positive Sr
470 anomalies [$Sr/Sr^* = Sr / (Pr^2 \times Nd^2)^{0.5}$] of 1.4–1.8 that are not observed in high-alkali basalts.
471 Chondrite–normalised REE patterns exhibit sub-parallel trends shifting towards REE
472 enrichments from low- to mid- to high-alkali basalts (Fig.13b). An increase in HREE/LREE
473 and a slight increase in MREE/LREE (where MREE is Medium REE) is observed from low-
474 to mid- to high-alkali basalts, with La_N/Yb_N and Nd_N/Yb_N of 9.2–21.1 and 4.7–8.1,
475 respectively (Fig. 13b).

476

477 **Sr, Nd and Pb isotopes**

478 Whole rock isotope data for Sr, Nd, and Pb were measured on a total of 12 samples
479 (Table 3). Sr and Nd isotope ratios have been corrected for an average age of 13 Ma from
480 published radiometric data of the Dunedin Volcano (Scott et al., 2020a). Whole rock Pb
481 concentrations are not sufficiently accurate (Table S2) to estimate initial ratios for Pb isotopic
482 ratios. The high-alkali basalts have $^{87}Sr/^{86}Sr_i$ of 0.70285–0.70315, $^{143}Nd/^{144}Nd_i$ of 0.51286–
483 0.51294, $^{206}Pb/^{204}Pb$ of 19.348–20.265, $^{207}Pb/^{204}Pb$ of 15.652–15.675, and $^{208}Pb/^{204}Pb$ of
484 39.309–39.727. This range overlaps with that determined for the mid-alkali basalts ($^{87}Sr/^{86}Sr_i$
485 of 0.70277–0.70315, $^{143}Nd/^{144}Nd_i$ of 0.51288–0.51292 and $^{206}Pb/^{204}Pb$ of 19.806–20.227,
486 $^{207}Pb/^{204}Pb$ of 15.658–15.686, and $^{208}Pb/^{204}Pb$ of 39.486–39.670). However, low-alkali
487 basalts have more radiogenic $^{87}Sr/^{86}Sr_i$ (0.70327–0.70397) and less radiogenic $^{143}Nd/^{144}Nd_i$,
488 (0.51282–0.51286), $^{206}Pb/^{204}Pb$ (19.278–19.793), $^{207}Pb/^{204}Pb$ (15.647–15.666), and
489 $^{208}Pb/^{204}Pb$ (39.088–39.474) (Fig. 14).

490 The isotopic compositions of high- and mid-alkali basalts have FOZO-HIMU affinities
491 (Fig. 14). HIMU stands for High-μ ($^{238}U/^{204}Pb$) and is used to define a source enriched in
492 radiogenic Pb (e.g., Stracke et al., 2005), whereas FOZO stands for "Focal Zone" (as
493 originally defined by Hart et al., 1992) to indicate the common "HIMU-type" component
494 found in most MORB and OIB settings (Stracke et al., 2005). Isotopic compositions for high-
495 and mid-alkali basalts are similar to previous literature data on Dunedin Volcano (Price et al.,
496 2003; Hoernle et al., 2006; Sprung et al., 2007; Timm et al., 2010; Scott et al., 2020). The
497 isotopic compositions are also consistent with the isotopic compositional range defined by
498 metasomatised mantle xenoliths from the Otago region (data from Scott et al., 2014a, b;
499 2016; McCoy-West et al., 2016; Dalton et al., 2017; Fig. 14). Notably, the isotopic
500 compositions of low-alkali basalts extend towards the compositional end-member EMII
501 (Enriched Mantle II as defined by Hart, 1988; Hart et al., 1992). This is best observed in

$^{87}Sr/^{86}Sr$ vs. $^{143}Nd/^{144}Nd$ (Fig. 14a) and $^{206}Pb/^{204}Pb$ vs. $^{208}Pb/^{204}Pb$ (Fig. 14d) diagrams. A similar (but less pronounced) increase in $^{87}Sr/^{86}Sr$ and $^{143}Nd/^{144}Nd$, and a slight decrease in $^{206}Pb/^{204}Pb$ and $^{208}Pb/^{204}Pb$ is also documented for some literature compositions, including one basaltic dyke from Allans Beach (locality of samples DVB8; Fig. 1 and Table 1) analysed by Sprung et al. (2007).

DISCUSSION

Mineral-melt equilibrium

Estimating the intensive variables controlling the crystallisation of minerals can be challenging, especially when coexisting glass is lacking due to abundant syn-eruptive crystallisation forming a crystalline groundmass, or post-eruptive modifications (e.g. Corsaro et al., 2013; Nazzari et al., 2019). A commonly adopted approach is to assume equilibrium between early-formed crystal cores and whole rock compositions as representative of the host magma (Putirka, 2008; Mollo et al., 2018; Palummo et al., 2020). However, the presence of antecrysts, which are argued to have segregated from recurrent magma injections may limit the effectiveness of this approach (e.g. Davidson et al., 2007; Ubide et al., 2014). To overcome issues with the use of whole rock compositions, we tested equilibrium conditions for phenocrysts in each rock sample after removing the compositional contribution of near-liquidus mineral phases (olivine and clinopyroxene; cf. Mollo et al., 2018) from the whole rock data. The proportions of phases removed from the whole rock compositions for each crystal type are included in Table 4. The theoretical equilibrium composition of the melt was further refined using a root mean square procedure, in which the putative range of melt compositions obtained was compared with the overall Dunedin Volcano data set of whole rock analyses (Scott et al., 2020a).

526 To test olivine–melt equilibrium, we adopted the conventional Fe-Mg exchange ($^{ol\text{-}melt}Kd_{Fe–Mg}$ = 0.30 ± 0.03) of Roeder and Emslie (1970), considered to be nearly constant over
527 a wide range of temperature, oxygen fugacity and bulk system composition (Fig. S1a). Type
528 1 olivine cores ($Fo_{81\text{-}87}$) are found to have equilibrated with melt compositions similar to
529 those of low-alkali basalts and the more primitive mid- and high-alkali basalts ($Mg\#_{55\text{-}67}$). In
530 contrast, type 2 olivine cores ($Fo_{74\text{-}82}$) have compositions indicating equilibrium with melts
531 ($Mg\#_{50\text{-}55}$) derived from low-alkali basalts and some mid-alkali basalts (Fig. S1a).
532 The equilibrium condition between clinopyroxene and melt was tested using the Fe-Mg
533 exchange ($^{cpx\text{-}melt}Kd_{Fe–Mg}$ = 0.28 ± 0.08) of Putirka (2008), in conjunction with more recent
534 models that rely on the difference (Δ) between measured vs. predicted diopside +
535 hedenbergite components (Putirka et al., 1996; Mollo et al., 2013; Mollo & Masotta, 2014), a
536 well as thermodynamically-predicted partition coefficients for Na (D_{Na}) and Ti (D_{Ti}) (Blundy
537 et al., 1995; Hill et al., 2011; Mollo et al., 2018, 2020). Type 1 clinopyroxene cores and type
538 1 mantles overgrowing type 2 cores from high-alkali basalts and some mid-alkali basalts
539 (Table 1 and Fig. S2a) equilibrated with melt compositions having $Mg\#_{35–53}$. In contrast, type
540 2 green cores were in equilibrium with more evolved melts ($Mg\#_{24–44}$) derived from high-
541 alkali basalts. Type 3 resorbed cores equilibrated with primitive melts ($Mg\#_{46–60}$) derived
542 from low-alkali basalts. Type 4 cores and type 4 mantles overgrowing type 3 cores
543 equilibrated with melts ($Mg\#_{44–56}$) derived from low- and mid-alkali basalts. Cr-rich zones
544 equilibrated with the more mafic compositions ($Mg\#_{46–60}$) in all basaltic samples. Overgrowth
545 rims encompass a wide compositional range, but are Mg-poor, Cr-poor and REE-rich relative
546 to types 1, 3 and 4 (Fig. 7); accordingly, they were in equilibrium with more differentiated
547 melts ($Mg\#_{30–44}$) (Fig. S2).
548 Plagioclase-melt equilibrium was assessed by comparing the An content of the analysed
549 crystals with that predicted by the An model of Putirka (2005) (Fig. S1c). Rare and highly
550

551 resorbed relic crystals (type 3) in primitive high-alkali basalts are not considered due to their
552 evident antecryst origin. Type 1 plagioclases do not appear to have equilibrated with melts
553 ($Mg\#_{52–66}$) derived from low- and mid-alkali basalts, whereas type 1 mantles were in
554 equilibrium with the same melt compositions. Type 2 plagioclases span a broad
555 compositional interval (Fig. 10), and only the more An-rich compositions are in equilibrium
556 with melts ($Mg\#_{35–43}$) from high-alkali basalts and a minority from mid-alkali basalts.
557 The attainment of equilibrium between titanomagnetite and the host melt was evaluated
558 through the Usp-based model of Aryaeva et al. (2018), in which the difference between
559 predicted and measured values of Usp (Fig. S1b) are minimised at *P–T* conditions obtained
560 by clinopyroxene-based barometry and thermometry (see below).
561
562 **Magma crystallisation conditions**
563 Only equilibrium mineral-melt pairs were used to determine magmatic crystallisation
564 conditions, and probability density functions were calculated to refine best estimates for
565 pressures, temperatures, melt H_2O contents, and oxygen fugacities (Fig. 15 and Fig. 16).
566 Probability density functions describe the relative probability of a random variable occurring
567 in the range of values in the investigated sample space. This helps defining an interval of
568 likelihood for the estimated crystallisation conditions, taken as one standard deviation above
569 and below the average value of the gaussian distribution. This treatment yields a refined
570 interpretation of large data sets by excluding outliers.
571 The crystallisation temperature of olivine was calculated with the Mg-thermometer
572 (error of ±26 °C) derived by Pu et al. (2017) and based on the original model of Beattie
573 (1993). Probability density functions indicate that type 1 and type 2 olivines equilibrated at
574 1180–1286 and 1134–1222 °C, respectively (Fig. 15a).

For clinopyroxene, the *P*-H_2O-independent thermometer (error of ±27 °C) of Putirka et al. (1996) was combined with the *T*-dependent barometer (error of ±130 MPa) of Putirka et al. (2003) specific to hydrous magmas, as well as the hygrometer (error of ±0.5 wt.% H_2O) of Perinelli et al. (2016). Type 1 clinopyroxene cores record crystallisation at 498–789 MPa, 1142–1186 °C, and 1.9–3.1 wt.% H_2O, while type 1 mantle compositions overgrowing type 2 cores record slightly shallower conditions: 423–754 MPa, 1120–1158 °C, and 2.3–3.3 wt.% H_2O (Fig. 16). The pressure estimates correspond to depths of 19–30 km for type 1 crystals and 16–27 km for type 1 mantles, assuming density stratigraphy of 2700 kg m^{-3} for the Haast Schist upper-/mid- crustal basement (Godfrey et al., 2001; Mortimer, 2004), ~3000 kg m^{-3} for gabbroic/ultramafic lower crustal lithologies between 20 and 30 km depth (Godfrey et al., 2001), and 3300 kg m^{-3} for the upper mantle. It is worth noting that type 1 crystals represent the main clinopyroxene population in peridotite-bearing high-alkali basalts and their crystallization pressure is close to close to the Moho depth of 25–30 km (Godfrey et al., 2001). Type 2 green cores formed at lower pressures, temperatures, and melt-H_2O contents of 351–693 MPa, 1074–1128°C, and 0.8–1.8 wt.%, respectively (Fig. 16), pointing to crystallisation at mid-to-lower crustal depths (13–25 km) and derivation from differentiated alkaline magmas. Type 3 resorbed cores recorded the deepest crystallisation conditions of 853–1059 MPa, 1209–1237 °C, and 2.5–3.5 wt.% H_2O, corresponding to the deep equilibration of low-alkali basalts and some mid-alkali basalts at 32–38 km of depth (i.e., the lithospheric mantle depth). Type 4 clinopyroxenes from low- and mid-alkali basalts saturated the magma at 532–808 MPa, 1152–1197 °C, and 2.5–3.3 wt.% H_2O, in close agreement with the formation of type 1 crystals. Similar conditions are recorded by type 4 mantle compositions overgrowing type 3 resorbed cores, crystallizing at 585–774 MPa, 1173–1202 °C and 2.6–3.4 wt.% H_2O. Deep crystallisation of clinopyroxene has often been observed in intraplate alkaline systems (e.g. Wilson et al., 1995; Smith et al., 2008; Re et al., 2017), and is

consistent with classic experimental crystallisation of mantle-derived alkaline magmas (Green & Hibberson, 1970; Sack et al 1987). The relatively low H_2O contents estimated for the basaltic magmas may explain the absence of amphibole in Dunedin Volcano mafic magmas (Price, 1973).

Cr-rich zones observed in clinopyroxene types 1 and 4 formed at conditions of 579–907 MPa, 1164–1208 °C, and 2.5–3.3 wt.% H_2O. The occurrence of concentric zones enriched in Cr and other compatible elements, and depleted in incompatible elements, has been identified as the fingerprint of mafic recharge in open magmatic plumbing systems (Ubide & Kamber, 2018). The common occurrence of Cr-rich zones in clinopyroxene crystals indicates persistent injections of fresh, hot mafic magmas during the entire evolution of alkali basalts. The similarity between melt-H_2O contents recorded by clinopyroxenes crystallised at greater depths (upper mantle to lower crust) and Cr-rich zones suggests that the concentration of H_2O was kept constant by recurrent mafic recharges (Fig. 17c). In contrast, crystal rims observed in all clinopyroxene types recorded slightly cooler and shallower crystallisation conditions of 381–691 MPa and 1131–1175 °C, although they indicate similar melt water contents of 1.9–3.1 wt.% H_2O.

The titanomagnetite-based oxygen barometer (error of ± 0.2 log unit) of Ariskin & Nikolaev (1996) indicates an overall highly variable melt redox state relative to the FMQ (fayalite-magnetite-quartz) buffer that is variable from ΔFMQ-2.78 to ΔFMQ+0.45 within a thermal range of 1140–1180 °C (Fig. 15b). High-alkali basalts show slightly more oxidizing conditions (from ΔFMQ-0.97 to ΔFMQ+0.53) than mid-alkali basalts (from ΔFMQ-1.87 to ΔFMQ+0.03) and low-alkali basalts (from ΔFMQ-2.18 to ΔFMQ-0.50) (fig. 15c). These conditions are also confirmed by the titanomagnetite-ilmenite model of Andersen & Lindsley (1985) (Fig. 15c).

For plagioclase, An contents are positively correlated with temperature and melt-H_2O content, therefore it is difficult to isolate the effect of each variable. This causes circular dependency in the application of H_2O-dependent thermometers and *T*-dependent hygrometers, in which the input *T* is a proxy for the estimates of H_2O and *vice versa* (cf. Mollo et al., 2011). To overcome this issue, the activity of An in the melt phase (${}^{melt}a_{An}$) was calculated using the thermodynamically derived coefficients of Glazner (1984). Then, ${}^{melt}a_{An}$ was used as input parameter in the thermodynamic Eqn. (28) of Namur et al. (2012), in order to derive the temperature (${}^{melt}T_{sat}$) at which the melt was saturated with plagioclase. Once ${}^{melt}T_{sat}$ was known, the melt-H_2O content was determined by applying the hygrometer of Putirka (2008) [Eqn. (25b) with error of ±1.1 wt.% H_2O] and compared to clinopyroxene-derived melt-H_2O contents in order to refine plagioclase-based temperature estimates based on the H_2O-dependent thermometer of Putirka et al. (2008) [Eqn. (24a) with error of ±36 °C]. Plagioclase-based models set the saturation of type 1 cores at 1028–1094 °C with a melt-H_2O content of 1.8–3.0 wt.%. Higher crystallisation temperatures of 1065–1123°C are found for type 1 mantles (Fig. 15d), although the melt-H_2O content remains almost constant at 1.4–3.0 wt.% (Fig. 15e). The entrainment of type 1 plagioclases in more mafic low- and mid-alkali basalts magmas is responsible for crystal core resorption and further development of An-rich mantle compositions (e.g., Streck, 2008; Cashman & Blundy, 2013). On the other hand, type 2 plagioclases recorded a lower temperature of 1054–1096°C and melt-H_2O content of 1.4–2.2 wt.%, confirming co-saturation with type 2 clinopyroxene.

A synthesis of crystallisation conditions for the different crystalline phases and types used to define probability density functions described above (Fig. 15 and Fig. 16), is included in Table 4.

Dunedin Volcano plumbing system

649 Many volcanological studies have described the variety and complexity of the eruptive
650 products from the Dunedin Volcano (Marshall, 1906; Benson & Turner, 1940; Benson, 1941,
651 1942; Allen, 1974; Price & Coombs, 1975) and have debated the possible liquid lines of
652 descent and mechanisms controlling magma differentiation (Coombs & Wilkinson, 1969;
653 Price & Taylor, 1973; Price & Chappell, 1975; Coombs et al., 2008). Nevertheless, little
654 attention has been given to the plumbing system geometry and the magma dynamics that
655 control such compositional differentiation. In Fig. 17, we present a schematic reconstruction
656 of the plumbing system architecture of the Dunedin Volcano based on the estimated
657 crystallisation conditions for the different basalt types. Peripheral eruptive products are made
658 up of mafic high-alkali basalts with $Mg\#_{60}$ and a phenocryst cargo exclusively made of type 1
659 clinopyroxene and Fo-rich type 1 olivine. Type 1 clinopyroxene crystallised in the lower
660 crust down to Moho depths, with no storage of peripheral high-alkali basalts at upper crustal
661 levels, as supported by absence of plagioclase phenocrysts that are inferred to be related to
662 magma degassing in eruptions around the centre of the edifice (Fig. 17). Cr-rich zones in
663 clinopyroxenes are evidence for the persistent injection of more mafic, hotter magmas at
664 depth (Ubide and Kamber, 2018; Ubide et al., 2019). The frequent occurrence of
665 clinopyroxene and olivine glomerocrysts are interpreted to indicate provenance from a crystal
666 mush, possibly disrupted by frequent magma recharge events (Seaman, 2000; Murphy et al.,
667 2000; Bachmann et al., 2002), and sector ("hourglass") zoning in type 1 crystals testify to
668 dynamic crystallization under moderate degrees of undercooling (Ubide et al., 2019; Masotta
669 et al., 2020). Evidence of magma mixing phenomena are more significant in high- and mid-
670 alkali basalt around the central part of the Dunedin Volcano edifice. However, the occurrence
671 of distinct phenocryst associations in Dunedin Volcano undifferentiated magmas, namely,
672 type 1 mantles on type 2 clinopyroxene cores in high-alkali basalts, and type 4 mantles on
673 type 3 clinopyroxene cores in mid- and low-alkali basalts, indicates mixing of overall similar

basaltic magmas. Plagioclase minor element contents in low-alkali basalts are homogeneous between crystal zones (not shown), unlike cases with obvious open system processes (e.g. crustal contamination, Coote et al., 2018). Therefore, it can be concluded that mixing did not significantly modify the composition of the poorly differentiated magmas or that it was at the origin of the transition between magmas with different alkaline character.

While most peripheral high-alkali basalts are exclusively characterized by type 1 clinopyroxene crystals, the occurrence of type 2 clinopyroxene green cores in high- and mid-alkali basalts indicate entrainment from more evolved and plagioclase-saturated magmas towards more internal sectors of the volcano (Fig. 1, Table 1). Green clinopyroxene cores have frequently been reported in alkaline continental systems (e.g. Brooks & Printzlau, 1978; Duda & Schmincke, 1985; Dobosi & Fodor, 1992; Aulinas et al., 2010; Marzoli et al., 2015), and are often interpreted as former constituents of evolved, highly crystalline stalled magmas, entrained by the ascending, hotter and more mafic magmas (e.g. Bedard et al., 1988; Ubide et al., 2014; Crossingham et al., 2018), although clinopyroxenes with metamorphic origin have also been reported (Jankovics et al., 2016) as well as green augitic cores related to metasomatic processes by melts percolating through the lithosphere (Pilet et al., 2002). Mineral-melt equilibrium models indicate crystallization of the green cores from melts consanguineous with high-alkali basalts (Table 4). The lack of crustal xenoliths in the Dunedin Volcano basalts and low Al, Sr and Eu contents in type 2 clinopyroxenes (Fig. 6 and Fig. 7) indicate that the green cores are likely to be derived from differentiated alkaline magmas co-saturated with plagioclase at mid-lower crustal depths (13-25 km), in a fashion similar to that documented for intraplate settings of Canary Islands (Spain, Aulinas et al., 2010), Noun Plain (Cameroon Volcanic Line; Ziem à Bidias et al., 2021) and Ulleung Island (South Korea, Brenna et al., 2014). Type 2 cores are overgrown by sector and oscillatory

zoned mantles with type 1 composition, indicating entrainment of the differentiated crystals by later basaltic magmas.

Low-alkali basalts are exclusively found in the central part of the edifice, where the eruptive products exhibit significant compositional variability and a maximum cumulative thickness (Coombs et al., 2008). These basalts are characterised by distinctive Sr, Nd, Pb isotopic compositions (Fig. 15) and by type 3 clinopyroxene resorbed cores, which equilibrated below the Moho depth (25-30 km according to Godfrey et al., 2001; Fig. 18). The crystallisation of type 4 clinopyroxenes in low- and mid-alkali basalts reflects ascent of magmas to lower crustal levels. Type 3 resorbed cores are overgrown by mantles whose composition and texture closely resemble type 4 crystals observed in the same samples. These, along with Cr-rich zones overgrowing both type 3 and type 4 clinopyroxene crystals, denote a continuous transfer of magma throughout the plumbing system (Fig. 17).

Magma storage near the Moho is consistent with the petrology of a suite of mafic magmatic cumulates and gabbroic-syenitic inclusions found in tephriphonolitic to phonolitic breccias around the centre of the Dunedin Volcano (Price et al., 2003). Known as the Port Chalmers Breccia, this is one of the most volumetrically important volcaniclastic units, and the diversity of the entrained xenoliths suggested the presence of a plumbing system extending through the whole crustal thickness, although no barometric constrains were available (Price et al., 2003).

Resorption of type 1 (An-poor) plagioclase cores and overgrowing (An-rich) mantles in low-alkali basalts imply magma recharge across the entire plumbing system, as magmas are transferred from the deeper storage depths towards shallower crustal levels (Fig. 17). At shallow crustal conditions, the abundant segregation of clinopyroxene and plagioclase is

721 responsible for the origin of highly differentiated trachytic and phonolitic endmembers
722 (Coombs & Wilkinson, 1969; Price & Chappell, 1975).

723

724 **Factors controlling the degree of alkalinity**

725 Different degrees of alkalinity and trace element compositions in Dunedin Volcano
726 basaltic rocks, coupled with varying phenocryst cargoes and distinct isotopic signatures, raise
727 the question of whether this variability represents a primary characteristic or is related to
728 processes affecting a single parental liquid. Consanguineous alkali to subalkali basalts with
729 geochemical and isotopic similarities to those from this study have been documented within
730 several volcanic fields in New Zealand (Dunedin Volcanic Group outlying flows, Scott et al.,
731 2020a; Canterbury area, Hoernle et al., 2006; Sprung et al., 2007; Timm et al., 2010;
732 Waiareka-Deborah Volcanic field; Hoernle et al., 2006, 2010; Scott et al., 2020b), Campbell
733 Island (Hoernle et al., 2006; Panter et al., 2006) and in the North Island (Auckland Volcanic
734 Field, McGee et al., 2013; Hopkins et al., 2020; South Auckland Volcanic Field, Cook et al.,
735 2005). Magmas with affinities ranging from alkaline to subalkaline are commonplace in
736 many intraplate volcanic systems worldwide, which are also characterised by comparable
737 trends in isotopic compositions. Some examples are in West Antartica (Panter et al., 2018),
738 South Korea (Brenna et al., 2014), Australia (Price et al., 1997; Elburg & Soesoo, 1999;
739 Crossingham et al., 2018) and Northwestern China (Xu et al., 2005). These compositional
740 intervals have been interpreted to reflect: 1) intrinsic variability of the source lithology (e.g.
741 Price et al., 1997; Cook et al., 2005; Xu et al., 2005; Hoernle et al., 2006; Sprung et al.,
742 2007); 2) different degrees of interaction of mantle-derived magmas with a metasomatised
743 subcontinental lithospheric mantle (SCLM; e.g. McGee et al., 2013; Panter et al., 2018); and
744 3) assimilation of crustal material by magmas derived from partial melting of a
745 metasomatised SCLM (Panter et al., 2006).

Assimilation-fractional crystallisation processes are difficult to reconcile with the compositional variation observed among basaltic products of this study. Low-alkali basalts are characterised by slightly higher SiO_2 concentrations than mid- and high-alkali basalts (Fig. 2a), but their incompatible element abundances are systematically lower (Fig. 13), contrary to what might be expected in scenarios controlled by crystal fractionation and crustal assimilation. Moreover, if crustal assimilation is responsible for the variation in isotopic compositions, then more differentiated low-alkali basalts, characterized by the lowest Mg# (DVB5b, DVB8a; Table 1) should be expected to be the most contaminated rocks. However, the most radiogenic sample (DVB5a; Table 3) exhibits the highest Mg# and lowest abundance of incompatible elements (Table 2).

Mantle processes

Isotopic trends depicted by high-, mid-, and low-alkali basalts are characterised by increasing $^{87}Sr/^{86}Sr$ and decreasing $^{143}Nd/^{144}Nd$, $^{206}Pb/^{204}Pb$, and $^{208}Pb/^{204}Pb$, extending from FOZO-HIMU values to an EMII signature (Fig. 14). Subalkaline basalts commonly display less negative K anomalies (e.g., Hoernle et al., 2006; Scott et al., 2020b), low La_N/Yb_N ratios (Cook et al., 2005) and are typically less enriched in LILE and LREE compared to their more alkaline counterparts. The presence of EMII-like domains in the source of alkaline magmatism in the SW pacific has been previously attributed to the enrichment of SCLM by subduction-related fluids (Zhang et al., 2001; Panter et al., 2006; Sprung et al., 2007). However, an extensive sample suite of mantle xenoliths from the Otago region lack an EMII-like signature. The metasomatised peridotites have been shown to have isotopic compositions that strongly overlap with those of Zealandia alkaline mafic magmas, in the ranges: $^{87}Sr/^{86}Sr$ of 0.7027–0.7033, $^{143}Nd/^{144}Nd > 0.5126$, $^{206}Pb/^{204}Pb$ of 19.2–20.4, and $^{207}Pb/^{204}Pb$ of 15.55–

15.68 (Scott et al., 2014a, b; McCoy-West et al. 2016; Dalton et al. 2017; Scott et al., 2020a; Fig. 14). The FOZO-HIMU isotopic characteristics of mid- and high-alkali basalts, such as $^{87}Sr/^{86}Sr$ of 0.7028–0.7032, $^{143}Nd/^{144}Nd > 0.51285$, $^{206}Pb/^{204}Pb$ of 19.6–20.3, and $^{207}Pb/^{204}Pb$ of 15.65–15.68 (Fig. 14), as well as their alkali-rich and OIB-like compositions (e.g. negative K and Ti anomalies and enrichments in LILE and LREE relative to Primitive Mantle, Fig. 13a) are consistent with derivation from a SCLM source. The underlying SCLM has been interpreted as either including recycled subducted material or featuring signatures previously inherited from a Cretaceous metasomatic event by subduction-related carbonatitic fluids (Panter et al., 2018; Scott et al., 2020a). Indeed, most data from the compilation of Scott et al. (2020a) on the Dunedin Volcano (see Fig. 14) and the outlying flows of the larger Dunedin Volcanic Group cluster in a relatively restricted isotopic space, suggesting that the geochemical signature of high- and mid-alkali basalts is largely representative of magmatism in the Otago region (Fig. 14). This is hypothesised to be derived from a metasomatised lithospheric mantle source, in agreement with previous interpretations of FOZO-HIMU magmatism in the South Island (Sprung et al., 2007; Scott et al., 2014a, b, 2016; McCoy-West et al., 2016; Dalton et al., 2017; for a review, see Scott et al., 2020a).

In order to test whether the metasomatised lithospheric mantle is a possible source of Dunedin Volcano magmas, we performed partial melting models based on the non-modal batch melting equations of Shaw (1970, 1979). To model melting of a metasomatically enriched SCLM, we followed the method applied by Scott et al. (2016), by adapting the peridotite composition to that of xenolith samples from the Dunedin Volcano (Scott et al., 2014a). We include major element modelling, using an amphibole composition based on the nearby Kakanui Mineral Breccia (Fulmer et al., 2010), with experimentally constrained melting modes from Medard & Schmidt (2008). The relevance of hydrous phases in a possible lithospheric mantle source of alkaline magmas is corroborated by the occurrence of

amphibole and phlogopite in mantle xenoliths from several localities across the South Island (Kakanui, Fulmer et al., 2010; Alpine Dyke Swarm, Scott et al., 2016; Westland Dyke Swarm, Serre et al., 2020a). The modelling approach is explained in the Supplementary Material Text S1 and complete details of melting models, including starting compositions, partition coefficients and partial melt compositions are included in Table S9.

Modelling results indicate that partial melts produced at low degrees of melting (between 5 and 10%) closely approximate the compositions of Dunedin Volcano high-alkali basalts (Fig. 13). At higher degrees of melting (15%; Fig. 13) the trace element compositions of mid-alkali basalts are also reproduced, except that LREE/HREE ratios are slightly higher (Fig. 13b). Increasing the degree of melting (up to 20%), generates modelled concentrations of LILE and major elements that seem to closely match those of the low-alkali basalts (Fig. 13a; Table S9), except for HREE contents and Ti anomaly. A relationship between Dunedin Volcano mantle-derived magmas is suggested by geochemical characteristics indicating a progressive variation from low- to mid- to high-alkali basalts (Fig. 11; Fig. 12; Fig. 13). However, variable degrees of partial melting of a single source cannot explain the differences in isotopic compositions between low-alkali basalts from those of mid- and high-alkali basalts (Fig. 14), hence invoking a sub-lithospheric source. Moreover, the similarities in trace element composition between high- and low-alkali basalts cannot be explained by partial melting of similar lithologies in both the lithosphere and the asthenosphere, as hydrous phases are not thermally stable at sub-lithospheric depths (Frost, 2006).

To test the possible involvement of asthenospheric melts, variable partial melting processes have been modelled assuming a source with the composition of an EMII-like fertile peridotite (spinel lherzolite). Details of the modelling approach are included in the Supplementary Material Text S1, with all input data and results included in Table S9. Modelled melt compositions at 5–10% melting are depleted in LILE and LREE with respect

to those derived from similar melting degrees of a metasomatised SCLM (Fig. 18a). Low-alkali, high-Mg# melts (SiO_2 = 51.6 wt.%, Mg# = 69, $Na_2O + K_2O$ = 2.2 wt.%) are modelled to mix with the alkali-rich, Mg-poor melts formed from metasome melting in the SCLM, resembling high-alkali basalts (SiO_2 = 45.1 wt.%, Mg# = 58, $Na_2O + K_2O$ = 5.5 wt.%; Fig. 18b, c). Since some low-alkali basalts are characterized by high estimated modal contents of clinopyroxene crystals (Table 1), we considered the possibility that small amounts of clinopyroxene crystals were entrained as antecrysts (e.g. Ubide et al., 2014) in our modelling approach. Accordingly, we corrected for accumulation of 10% clinopyroxene in the low-alkali basalts during percolation and mixing with the metasomatic melts. Accumulation of >10% crystals would result in unreasonably high Mg#, and is unlikely since large crystals were avoided during sample preparation for whole rock analysis.

Mineral-scale investigations have proven crucial in exploring the petrogenesis of crystal-rich rocks, and revealed the potential difficulties in the interpretations of whole-rock geochemistry (e.g. Ginibre et al., 2007; Jankovics et al., 2012, 2013; Ubide et al., 2014; Batki et al., 2018). Dunedin Volcano basalts are variably porphyritic but their geochemical characteristics are consistent with those of mantle-derived alkaline basaltic rocks in the region (see Hoernle et al., 2006; Sprung et al. 2007; Scott et al., 2016; Scott et al., 2020a, b). Uncertainties in our adopted whole-rock compositions correction scheme may arise from possible antecrystic entrainment abundances and some degree of magmatic recharge and mixing (e.g. Reubi et al., 2002; Eichelberger et al., 2006; Wanke et al., 2020). Nonetheless, entrapment of antecrystic material and open system processes cannot explain the first order whole-rock geochemical variability observed at Dunedin Volcano and the broader Otago region. The consistent contrasts in isotopic characteristics of alkaline and subalkaline magmas in the region cannot be related to open system processes. These have previously been ruled out (see also Hoernle et al., 2006; Sprung et al., 2007; Scott et al., 2020a) and are

difficult to reconcile with homologous crystal entrainment on a regional scale. Magmatic recharge and hybridization between mafic magmas having similar compositions are unlikely to affect bulk chemistry to a large degree (e.g. Armienti et al., 2007; Mollo et al., 2018). In spite of the complex intracrystalline variations and multiple crystal populations, different basalt types (e.g. low vs high alkali basalts) are characterized by distinct crystalline populations (Table 1), suggesting hybridization among the different basalts is likely unimportant. Given the distinct isotopic character of high-alkali and low-alkali magmas this process would also require sourcing from different mantle domains and cannot explain variable crystal content. In this context, future detailed investigations of the crystal cargo isotopic record (Coote et al., 2018; Xing & Wang, 2020) could be crucial in refining our understanding and detailing the petrogenetic history of Otago magmas.

Our model produces magmas with the same trace element contents of low-alkali basalts, provided that 20-40% of SCLM-derived liquids are mixed with the asthenospheric melts (Fig. 18). The primary isotopic composition of the asthenospheric melt, determined through major and trace element models, does not directly match with an EMII source, as it depends on the mixing proportions with the SCLM-derived melts. Fig. 14 shows that the primary melt composition extends further towards the EMII reservoir (Hart et al., 1992) compared with the isotopic composition of low-alkali basalts. We therefore propose that the observed isotopic trend of basalts from Dunedin Volcano reflects an increasing interaction between EMII-like partial melts (60–80%) derived from a fertile asthenospheric source and previously metasomatised SCLM material (20–40%) (Fig. 14; Fig. 17; Fig.18c). Involvement of an EMII-like component in the generation of mafic magmas in the South Island has previously been proposed for “high-silica basalts” in the Canterbury area (Hoernle et al., 2006; Sprung et al. 2007; Timm et al., 2010), the Waiareka-Deborah products (Timm et al., 2010) and Lookout eruptions (McCoy-West et al., 2010). The EMII character has mainly

been explained by the involvement of an EMII-like SCLM component and/or crustal contamination (Sprung et al., 2007; McCoy-West et al., 2010; Timm et al., 2010). Here we provide the first quantitative evaluation supporting an asthenospheric origin for the EMII-like component.

Low-alkali basalt isotopic signatures can thus be related to the presence of fertile domains in the asthenosphere beneath the Otago region, perhaps caused by subduction-recycled lithospheric material (e.g. Loubet et al., 1988; Willbold & Stracke, 2010). Intraplate volcanism in eastern Australia and New Zealand may have been triggered by past subduction causing stagnating slabs at the Mantle Transition Zone (MTZ) to release fluids and promote melting in fertile regions of the asthenosphere (Mather et al., 2020), similar to the mechanism proposed for northeast China by Yang & Faccenda (2020). Interaction between asthenospheric melts and SCLM can explain the geochemical signatures of low-alkali basalts. Additionally, LREE/HREE of low-alkali basalts are lower than those characterizing high- and mid-alkali basalts and this suggests that garnet lherzolite is an unlikely source lithology for the EMII-like melts. As a consequence, melt generation is expected at conditions between the lithosphere-asthenosphere boundary (estimated at ~70 km depth; Scott et al., 2014a) and the upper stability limit of garnet in lherzolite (estimated to be at 85 km on average; e.g. Robinson & Wood, 1998; Klemme, 2004). Subalkaline liquids produced by variable degrees of lherzolite partial melting (typically 5–20%; Hirose & Kushiro, 1993) may have percolated through the lithosphere, where metasomatic veins are the most readily fusible lithologies, thus representing favourable pathways for the ascending magmas (e.g. Pilet, 2015). Melting of the metasomatised SCLM may have been initiated by a perturbation of the thermal state of the lithosphere due to percolation of asthenospheric melts (Pilet, 2015). This is inferred to have produced high- and mid-alkali basalts with FOZO-HIMU isotopic compositions typical of the lithospheric mantle in the region (Fig.14). High-alkali basalts equilibrated at relatively

reducing conditions (from ΔFMQ-0.97 to ΔFMQ+0.53), although the oxygen fugacity was higher than that estimated for low-alkali basalts (from ΔFMQ-2.18 to ΔFMQ-0.50; Fig.15c; Table 4), supporting derivation of alkali-rich melts from amphibole-bearing metasomes in the lithosphere, where Fe^{3+} is more abundant relative to typical mantle phases (e.g. Dyar et al., 1993).

Magma differentiation processes

To better constrain the origin and potential consanguinity of the more evolved rocks (i.e., from trachybasalt to mugearite; Fig. 2a) with the more mafic basalts from Dunedin Volcano, a set of mass balance calculations based on the least-square approach of Stormer & Nicholls (1977) was performed. We tested and quantified the mineral assemblage that reproduces high-alkali basalts with $Mg\#_{40}$ (Table 1), starting from either high- or mid-alkali basalts. Because of the lack of basalts with $Mg\#_{40}$ and EMII-like isotopic compositions in either our dataset or in literature data (Fig.14), low-alkali basalts were not considered in the fractionation modelling. Rayleigh fractional crystallisation (FC; cf. Rollinson, 1993 and references therein) was used to model the trace element evolution by fractionation of olivine, clinopyroxene and titanomagnetite in the same proportions as mass balance calculations. Plagioclase was excluded due to the lack of Eu anomaly in the rock samples. Complete details of major and trace element modelling, including starting magma compositions, observed and predicted fractionating assemblages, mineral and bulk partition coefficients, and residual melt compositions are reported in Table S10 and modelling results are also illustrated in Fig. S3. Through this approach, we conclude that both mid- and high-alkali basalts are parental compositions of trachybasalts and mugearites, although mid-alkali basalts require greater extents of olivine and clinopyroxene fractionation to reproduce the major

element compositions of more evolved magmas (Table S10). Modelled mid-alkali basalts have lower concentrations of LILE and LREE and strong Ti depletions when compared with modelled high-alkali basalts (Fig. S3). Although the reconstruction of the liquid lines of descent at Dunedin Volcano is beyond the scope of this work, derivation of tephrites to phonolites (Fig. 2a) would be more easily reconciled by starting from high-alkali basalt parental magmas, ultimately produced by low degrees of melting of the metasomatised SCLM source.

Implications for intraplate volcanism

Intraplate basaltic suites commonly display subalkaline to alkaline compositional trends that are explained as primary features by 1) variations in the mantle source lithology; 2) lithospheric versus asthenospheric origin; and 3) variable degrees of partial melting (e.g. Cook et al., 2005; Needham et al., 2011; McGee et al., 2012; Lee et al., 2021). Many authors have recognised the importance of the SCLM in potentially influencing the distribution and composition of alkaline magmatism in New Zealand (e.g., Panter et al., 2006; Sprung et al., 2007; Timm et al., 2010; Scott et al., 2014b). However, there is no consensus on the mechanism(s) responsible for the generation of magmas and for their compositional variability, and there is no supporting evidence for mantle plumes or lithospheric detachments in the region (e.g. Finn et al., 2005; Hoernle et al., 2006).

Dunedin Volcano high- and mid-alkali basalts have isotopic and trace element compositions indicating provenance from a metasomatised lithospheric mantle, matching the FOZO-HIMU isotopic composition of the lithosphere. However, low-alkali basalts from this study and subalkaline basalts from elsewhere in Zealandia (Cook et al., 2005; Needham et al., 2011; McGee et al., 2012; Scott et al., 2020b) do not conform to a SCLM source but rather

point to the involvement of an EMII source, possibly representing fertile domains in the asthenosphere (Fig. 17). Mid-alkali basalts with intermediate major and trace element compositions can be explained by higher degrees of melting of metasomatised SCLM material (Fig. 13) or by more limited contributions of asthenospheric melts, as mid-alkali basalts are frequently found in association with low-alkali basalts. Accordingly, it is inferred that abundant volumes of asthenospheric melt percolated through the lithosphere towards the centre of the Dunedin Volcano edifice, locally promoting high degrees of metasome melting (Fig. 17). Conversely, low degrees of melting produced high-alkali basalts towards the periphery of the volcano, in response to a more limited infiltration of asthenospheric melts, which did not reach the surface. The mantle-derived, more alkaline outlying flows in the Otago region, mostly erupted at monogenetic centres (Scott et al., 2020a), may be explained by this decrease in melt percolation through the lithosphere. The prolonged volcanic activity of the Dunedin Volcano (16-11 Ma), as well as the outlying flows in the Otago region (25-9 Ma) and the coexistence of HIMU-like and EM-like magmas may be related to the indirect influence of subducted slabs that caused destabilization of a volatile-enriched mantle transition zone (Mather et al., 2020). Previously subducted sediments can explain hydration of the mantle transition zone as well as the EM geochemical signatures of magmas (Yang & Faccenda; 2020). HIMU-like signatures may relate to a similar process involving subduction of older carbonate-rich sediments, and are more common in Eastern Australia and New Zealand in the volcanic centres located to the south of an ideal divide at 33°S (Mather et al., 2020). Rising melt pockets percolated through the lithosphere, forming HIMU-like metasomatic veins (Pilet et al., 2015). Subsequent percolation of the younger EMII-like melts may have promoted voluminous magma production.

The formation of a composite volcanic system in the middle of an intraplate monogenetic field, could be related to either lateral variation in mantle fertility and/or in melt

968 interconnectivity in the overlying lithosphere (e.g. Canon-Tapia & Walker, 2004). The
969 compositional variability of basaltic magmas erupted at Dunedin Volcano can thus be
970 explained as the result of the "filtering" effect of the lithospheric mantle. Asthenospheric melt
971 percolation in the lithosphere influences the composition of rising melts, together with the
972 degree of wall-rock interaction and the extent of partial melting of the metasomatic
973 lithologies (e.g. Navon & Stolper, 1987; Vernieres et al., 1997; Brunelli & Seyler, 2010; Lee
974 et al., 2021). Multi-stage magma ascent and differentiation at upper mantle to lower crustal
975 levels have been interpreted to characterize intraplate volcanoes with low magma supply rates
976 (e.g. Stroncik et al., 2008). Stagnation at shallower levels and subsequent differentiation to
977 intermediate-evolved magmas were likely spatially constrained towards the centre of the
978 Dunedin Volcano, and temporally related to periods of higher magma supply rates.

979

980 **CONCLUSIONS**

981 The Dunedin Volcano developed in an intraplate setting and is characterised by a
982 spectrum of relatively primitive eruptive products ranging from low- to mid- to high-alkali
983 basalts. Low-alkali basalts typically have more radiogenic Sr and less radiogenic Nd and Pb
984 (EMII component) than high- and mid-alkali basalts. Different petrological features of these
985 basalts reflect diverse magma storage conditions in the lithosphere and complex dynamics
986 involving mafic recharge and mixing during the stalling and transfer of magmas. The crystal
987 cargoes of high-alkali basalts record crystallisation at lower crustal depths (19 - 30 km)
988 followed by eruption bypassing storage reservoirs in the shallow crust. In contrast, low-alkali
989 basalts underwent polybaric crystallisation in a plumbing system that extended from the
990 lithospheric mantle to the upper crust. Mafic relic clinopyroxene cores carried by these
991 magmas recorded interaction of the primary magma with the lithospheric mantle. Mid-alkali

basalts have transitional properties between high- and low-alkali basalts. Major and trace element compositions of minerals and whole rocks, as well as Sr-Nd-Pb isotopic characteristics of the eruptives indicate that the sources of the Dunedin Volcano basalts are likely to have been located within the lithospheric and asthenospheric mantle. It is envisaged that asthenospheric EMII-like melts infiltrated and thermally perturbed the metasomatised lithospheric mantle to generate high- to mid-alkali basalt with increasing degrees of melting of metasomes. In contrast, rare low-alkali basalts appear to have had limited interaction with the lithospheric mantle filter and therefore largely retain asthenospheric characteristics. The mantle lithosphere is therefore likely to have modulated the alkaline character of this intraplate basaltic province. Higher rates of localised asthenospheric magma production in the central part of the system are likely to have produced low-alkali basalts that bypassed the lithospheric filter. Volumetrically more abundant asthenospheric melts percolating the lithosphere allowed greater degrees of lithospheric melting, forming mid-alkali basalts. More peripheral eruptions, as well as regionally dispersed volcanoes, were fed by melts (high-alkali basalts) produced by lower extents of lithospheric (metasome) melting, possibly related to thermal disturbance following minor asthenospheric melt percolation.

FUNDING

Marco Brenna acknowledges support from the University of Otago Research Committee. Teresa Ubide is supported by a Foundation Research Excellence Award from The University of Queensland (UQ-FREA RM2019001828).

ACKNOWLEDGEMENTS

We would like to express our gratitude James D.L. White, Mike Palin and Rachael Baxter for discussions on the Dunedin Volcano. Brent Pooley helped with sample preparation. This paper is dedicated to the memory of the late P. Armienti, who has been and continues to be inspirational to the scientific community. We thank George F. Cooper, Szabolcs Harangi, Kurt S. Panter and Richard C. Price for thoughtful reviews that greatly helped to improve the manuscript and Gerhard Wörner for the editorial work.

1022 **REFERENCES**

1023 Abouchami, W. & Galer, S. J. G. (1998). Practical Application of Lead Triple Spiking
1024 for Correction of Instrumental Mass Discrimination. Mineralogical Magazine; **62A**; no. 1;
1025 491-492.

1026 Adam, J. & Green, T. (2006). Trace element partitioning between mica- and
1027 amphibole-bearing garnet lherzolite and hydrous basanitic melt: 1. Experimental results and
1028 the investigation of controls on partitioning behaviour. *Contributions to Mineralogy and*
1029 *Petrology* **152**, 1–17.

1030 Andersen, D. J. & Lindsley, D. H. (1985). New (and final!) models for the Ti-
1031 magnetite/ilmenite geothermometer and oxygen barometer. Abstract AGU 1985 Spring
1032 Meeting Eos Transactions. American Geophysical Union 66, 18, 416.

1033 Armienti, P., Innocenti, F. & Orazio, M. (2007). Mount Etna pyroxene as tracer of
1034 petrogenetic processes and dynamics of the feeding system. Special Paper of the Geological
1035 Society of America 418, 265–2418.

1036 Armienti, P., Perinelli, C. & Putirka, K. D. (2013). A New Model to Estimate Deep-
1037 level Magma Ascent Rates, with Applications to Mt. Etna (Sicily, Italy). Journal of Petrology
1038 54, 795–813.

1039 Aryaeva, N. S., Koptev-Dvornikov, E. V. & Bychkov, D. A. (2018). A Liquidus
1040 Thermobarometer for Modeling of the Magnetite–Melt Equilibrium. Moscow University
1041 Geology Bulletin 73, 177–186.

1042 Aulinas, M., Gimeno, D., Fernandez-Turiel, J. L., Font, L., Perez-Torrado, F. J.,
1043 Rodriguez-Gonzalez, A. & Nowell, G. M. (2010). Small-scale mantle heterogeneity on the

1044 source of the Gran Canaria (Canary Islands) Pliocene–Quaternary magmas. Lithos 119, 377–
1045 392.

1046 Bachmann, O., Dungan, M. A. & Lipman, P. W. (2002). The Fish Canyon Magma
1047 Body, San Juan Volcanic Field, Colorado: Rejuvenation and Eruption of an Upper-Crustal
1048 Batholith. Journal of Petrology 43, 1469–1503.

1049 Batki, A., Pál-Molnár, E., Jankovics, M. É., Kerr, A. C., Kiss, B., Markl, G., Heincz, A.
1050 & Harangi, S. (2018). Insights into the evolution of an alkaline magmatic system: An in situ
1051 trace element study of clinopyroxenes from the Ditrău Alkaline Massif, Romania. Lithos
1052 300–301, 51–71.

1053 Beattie, P. (1993). Olivine-melt and orthopyroxene-melt equilibria. Contributions to
1054 Mineralogy and Petrology 115, 103–111.

1055 Bédard, J. H. J., Francis, D. M. & Ludden, J. (1988). Petrology and pyroxene chemistry
1056 of Monteregian dykes: the origin of concentric zoning and green cores in clinopyroxenes
1057 from alkali basalts and lamprophyres. Canadian Journal of Earth Sciences 25, 2041–2058.

1058 Benson, W.N., (1941). The basic igneous rocks of eastern Otago and their tectonic
1059 environment, Part 1. Transactions of the Royal Society of New Zealand. 71:208-222.

1060 Benson, W.N. (1942). The basic igneous rocks of eastern Otago and their tectonic
1061 environment, Part II. Transactions of the Royal Society of New Zealand. 72:85–118.

1062 Benson, W. N. (1968). Dunedin District. 1: 50000. New Zealand Geological Survey
1063 miscellaneous series map, 1, 1-18.

1064 Benson, W. N. & Turner, F. J. (1940). Mugearites in the Dunedin district. Transactions
1065 of the Royal Society of New Zealand, 70, 188-199

Blundy, J. D., Falloon, T. J., Wood, B. J. & Dalton, J. A. (1995). Sodium partitioning between clinopyroxene and silicate melts. Journal of Geophysical Research: Solid Earth 100, 15501–15515.

Bondi, M., Morten, L., Nimis, P., Rossi, P. L. & Tranne, C. A. (2002). Megacrysts and mafic–ultramafic xenolith-bearing ignimbrites from Sirwa Volcano, Morocco: phase petrology and thermobarometry. Mineralogy and Petrology 75, 203–221.

Boyce, J. A., Nicholls, I. A., Keays, R. R. & Hayman, P. C. (2015). Variation in parental magmas of Mt Rouse, a complex polymagmatic monogenetic volcano in the basaltic intraplate Newer Volcanics Province, southeast Australia. Contributions to Mineralogy and Petrology 169, 11.

Brenna, M., Price, R., Cronin, S. J., Smith, I. E. M., Sohn, Y. K., Kim, G. B. & Maas, R. (2014). Final Magma Storage Depth Modulation of Explosivity and Trachyte–Phonolite Genesis at an Intraplate Volcano: a Case Study from Ulleung Island, South Korea. Journal of Petrology 55, 709–747.

Brenna, M., Nakada, S., Miura, D., Toshida, K., Ito, H., Hokanishi, N. & Nakai, S. (2015). A trachyte–syenite core within a basaltic nest: filtering of primitive injections by a multi-stage magma plumbing system (Oki-Dōzen, south-west Japan). Contributions to Mineralogy and Petrology 170, 22.

Brenna, M., Ubide, T., Nichols, A. R. L., Mollo, S. & Pontesilli, A. (2021). Anatomy of Intraplate Monogenetic Alkaline Basaltic Magmatism. Crustal Magmatic System Evolution. American Geophysical Union (AGU), 79–103.

Brooks, C. K. & Printzlau, I. (1978). Magma mixing in mafic alkaline volcanic rocks: the evidence from relict phenocryst phases and other inclusions. Journal of Volcanology and Geothermal Research 4, 315–331.

Brunelli, D. & Seyler, M. (2010). Asthenospheric percolation of alkaline melts beneath the St. Paul region (Central Atlantic Ocean). Earth and Planetary Science Letters 289, 393–405.

Cañón-Tapia, E. & Walker, G. P. L. (2004). Global aspects of volcanism: the perspectives of "plate tectonics" and "volcanic systems." Earth-Science Reviews 66, 163–182.

Cashman, K. & Blundy, J. (2013). Petrological cannibalism: the chemical and textural consequences of incremental magma body growth. Contributions to Mineralogy and Petrology 166, 703–729.

Choi, S. H., Kwon, S.-T., Mukasa, S. B. & Sagong, H. (2005). Sr–Nd–Pb isotope and trace element systematics of mantle xenoliths from Late Cenozoic alkaline lavas, South Korea. *Chemical Geology* **221**, 40–64.

Coltorti, M., Bonadiman, C., Hinton, R. W., Siena, F. & Upton, B. G. J. (1999). Carbonatite Metasomatism of the Oceanic Upper Mantle: Evidence from Clinopyroxenes and Glasses in Ultramafic Xenoliths of Grande Comore, Indian Ocean. Journal of Petrology 40, 133–165.

Cook, C., Briggs, R. M., Smith, I. E. M. & Maas, R. (2005). Petrology and Geochemistry of Intraplate Basalts in the South Auckland Volcanic Field, New Zealand: Evidence for Two Coeval Magma Suites from Distinct Sources. Journal of Petrology 46, 473–503.

Coombs, D. S. & Wilkinson, J. F. G. (1969). Lineages and Fractionation Trends in Undersaturated Volcanic Rocks from the East Otago Volcanic Province (New Zealand) and Related Rocks. Journal of Petrology 10, 440–501.

Coombs, D. S., Cas, R. A., Kawachi, Y., Landis, C. A., McDonough, W. F., & Reay, A. (1986). Cenozoic volcanism in north, east and central Otago. Royal Society of New Zealand Bulletin, 23, 278-312.

Coombs, D. S., Adams, C. J., Roser, B. P. & Reay, A. (2008). Geochronology and geochemistry of the Dunedin Volcanic Group, eastern Otago, New Zealand. New Zealand Journal of Geology and Geophysics 51, 195–218.

Coote, A., Shane, P., Stirling, C. & Reid, M. (2018). The origin of plagioclase phenocrysts in basalts from continental monogenetic volcanoes of the Kaikohe-Bay of Islands field, New Zealand: implications for magmatic assembly and ascent. Contributions to Mineralogy and Petrology 173, 14.

Crossingham, T. J., Ubide, T., Vasconcelos, P. M., Knesel, K. M. & Mallmann, G. (2018). Temporal constraints on magma generation and differentiation in a continental volcano: Buckland, eastern Australia. Lithos 302–303, 341–358.

Dalpé, C. (1994). Partition coefficients for rare-earth elements between calcic amphibole and Ti-rich basanitic glass at 1.5 GPa, 1,100°C. Mineralogical Magazine, 58, 207-208.

Dalton, H. B., Scott, J. M., Liu, J., Waight, T. E., Pearson, D. G., Brenna, M., Roux, P. L. & Palin, J. M. (2017). Diffusion-zoned pyroxenes in an isotopically heterogeneous mantle lithosphere beneath the Dunedin Volcanic Group, New Zealand, and their implications for intraplate alkaline magma sources. Lithosphere 9, 463–475.

Davidson, J. P., Morgan, D. J., Charlier, B. L. A., Harlou, R. & Hora, J. M. (2007). Microsampling and Isotopic Analysis of Igneous Rocks: Implications for the Study of Magmatic Systems. Annual Review of Earth and Planetary Sciences 35, 273–311.

1136 Dobosi, G. & Fodor, R. V. (1992). Magma fractionation, replenishment, and mixing as
1137 inferred from green-core clinopyroxenes in Pliocene basanite, southern Slovakia. Lithos 28,
1138 133–150.

1139 Duda, A. & Schmincke, H.-U. (1985). Polybaric differentiation of alkali basaltic
1140 magmas: evidence from green-core clinopyroxenes (Eifel, FRG). Contributions to
1141 Mineralogy and Petrology 91, 340–353.

1142 Dyar, M. D., Mackwell, S. J., McGuire, A. V., Cross, L. R. & Robertson, J. D. (1993).
1143 Crystal chemistry of Fe3+ and H+ in mantle kaersutite: Implications for mantle
1144 metasomatism. *American Mineralogist*. GeoScienceWorld **78**, 968–979.

1145 Eichelberger, J. C., Izbekov, P. E. & Browne, B. L. (2006). Bulk chemical trends at arc
1146 volcanoes are not liquid lines of descent. Lithos 87, 135–154.

1147 Elburg, M. A. & Soesoo, A. (1999). Jurassic alkali-rich volcanism in Victoria
1148 (Australia): lithospheric versus asthenospheric source. Journal of African Earth Sciences 29,
1149 269–280.

1150 Elkins, L. J., Gaetani, G. A. & Sims, K. W. W. (2008). Partitioning of U and Th during
1151 garnet pyroxenite partial melting: Constraints on the source of alkaline ocean island basalts.
1152 *Earth and Planetary Science Letters* **265**, 270–286.

1153 Farmer, G. L. (2003). Continental Basaltic Rocks. Treatise on Geochemistry 3, 659.

1154 Frost, D. J. (2006). The Stability of Hydrous Mantle Phases. *Reviews in Mineralogy*
1155 *and Geochemistry*. GeoScienceWorld **62**, 243–271.

1156 Fujimaki, H., Tatsumoto, M. & Aoki, K. (1984). Partition coefficients of Hf, Zr, and
1157 ree between phenocrysts and groundmasses. *Journal of Geophysical Research: Solid Earth*
1158 **89**, B662–B672.

Fulmer, E. C., Nebel, O. & Westrenen, W. van (2010). High-precision high field strength element partitioning between garnet, amphibole and alkaline melt from Kakanui, New Zealand. *Geochimica et Cosmochimica Acta* **74**, 2741–2759.

Finn, C. A., Müller, R. D. & Panter, K. S. (2005). A Cenozoic diffuse alkaline magmatic province (DAMP) in the southwest Pacific without rift or plume origin. Geochemistry, Geophysics, Geosystems 6.

Gaina, C., Müller, D. R., Royer, J.-Y., Stock, J., Hardebeck, J. & Symonds, P. (1998). The tectonic history of the Tasman Sea: A puzzle with 13 pieces. Journal of Geophysical Research: Solid Earth 103, 12413–12433.

Galer, S. J. G. & Abouchami, W. (1998). Practical Application of Lead Triple Spiking for Correction of Instrumental Mass Discrimination. Mineralogical Magazine 62A, 491–492.

Garrison, J. M., Sims, K. W. W., Yogodzinski, G. M., Escobar, R. D., Scott, S., Mothes, P., Hall, M. L. & Ramon, P. (2017). Shallow-level differentiation of phonolitic lavas from Sumaco Volcano, Ecuador. Contributions to Mineralogy and Petrology 173, 6.

Giacomoni, P. P., Coltorti, M., Bryce, J. G., Fahnestock, M. F. & Guitreau, M. (2016). Mt. Etna plumbing system revealed by combined textural, compositional, and thermobarometric studies in clinopyroxenes. Contributions to Mineralogy and Petrology 171, 34.

Ginibre, C., Wörner, G. & Kronz, A. (2007). Crystal Zoning as an Archive for Magma Evolution. Elements. GeoScienceWorld 3, 261–266.

Glazner, A. F. (1984). Activities of olivine and plagioclase components in silicate melts and their application to geothermometry. Contributions to Mineralogy and Petrology 88, 260–268.

1182 Godfrey, N. J., Davey, F., Stern, T. A. & Okaya, D. (2001). Crustal structure and
1183 thermal anomalies of the Dunedin Region, South Island, New Zealand. Journal of
1184 Geophysical Research: Solid Earth 106, 30835–30848.

1185 Gorman, A. R. *et al.* (2013). Quaternary shelf structures SE of the South Island, imaged
1186 by high-resolution seismic profiling. *New Zealand Journal of Geology and Geophysics*.
1187 Taylor & Francis **56**, 68–82.

1188 Green, D. H. (1973). Experimental melting studies on a model upper mantle
1189 composition at high pressure under water-saturated and water-undersaturated conditions.
1190 Earth and Planetary Science Letters 19, 37–53.

1191 Green, D. H. & Hibberson, W. (1970). Experimental duplication of conditions of
1192 precipitation of high-pressure phenocrysts in a basaltic magma. Physics of the Earth and
1193 Planetary Interiors **3**, 247–254.

1194 Green, T. H., Blundy, J. D., Adam, J. & Yaxley, G. M. (2000). SIMS determination of
1195 trace element partition coefficients between garnet, clinopyroxene and hydrous basaltic
1196 liquids at 2–7.5 GPa and 1080–1200°C. *Lithos* **53**, 165–187.

1197 Harris C., P le Roux, R Cochrane, L Martin, AR Duncan, JS Marsh, AP le Roex, C
1198 Class (2015) The oxygen isotope composition of Karoo and Etendeka picrites: High δ18O
1199 mantle or crustal contamination? Contributions to Mineralogy and Petrology, 170, 1-24

1200 Hart, S. R. (1988). Heterogeneous mantle domains: signatures, genesis and mixing
1201 chronologies. Earth and Planetary Science Letters 90, 273–296.

1202 Hart, S. R., Hauri, E. H., Oschmann, L. A. & Whitehead, J. A. (1992). Mantle Plumes
1203 and Entrainment: Isotopic Evidence. Science 256, 517–520.

Hauri, E. H. & Hart, S. R. (1993). ReOs isotope systematics of HIMU and EMII oceanic island basalts from the south Pacific Ocean. Earth and Planetary Science Letters 114, 353–371.

Hill, E., Blundy, J. D. & Wood, B. J. (2011). Clinopyroxene–melt trace element partitioning and the development of a predictive model for HFSE and Sc. Contributions to Mineralogy and Petrology 161, 423–438.

Hirose, K. & Kushiro, I. (1993). Partial melting of dry peridotites at high pressures: Determination of compositions of melts segregated from peridotite using aggregates of diamond. Earth and Planetary Science Letters **114**, 477–489.

Hoernle, K. et al. (2006). Cenozoic intraplate volcanism on New Zealand: Upwelling induced by lithospheric removal. Earth and Planetary Science Letters 248, 350–367.

Hoke, L., Poreda, R., Reay, A., Weaver, S.D., 2000. The subcontinental mantle beneath southern New Zealand, characterised by helium isotopes in intraplate basalts and gas-rich springs. Geochimica et Cosmochimica Acta, 64: 2489- 2507.

Hopkins, J. L. et al. (2020). Auckland Volcanic Field magmatism, volcanism, and hazard: a review. New Zealand Journal of Geology and Geophysics. Taylor & Francis 0, 1–22.

Iezzi, G., Mollo, S., Shahini, E., Cavallo, A. & Scarlato, P. (2014). The cooling kinetics of plagioclase feldspar as revealed by electron-microprobe mapping. American Mineralogist 99, 898–907.

Jankovics, M. É., Harangi, S., Kiss, B. & Ntaflos, T. (2012). Open-system evolution of the Füzes-tó alkaline basaltic magma, western Pannonian Basin: Constraints from mineral textures and compositions. Lithos 140–141, 25–37.

1227 Jankovics, M. É., Dobosi, G., Embey-Isztin, A., Kiss, B., Sági, T., Harangi, S. &
1228 Ntaflos, T. (2013). Origin and ascent history of unusually crystal-rich alkaline basaltic
1229 magmas from the western Pannonian Basin. Bulletin of Volcanology 75, 749.

1230 Jankovics, M. É., Harangi, S., Németh, K., Kiss, B. & Ntaflos, T. (2015). A complex
1231 magmatic system beneath the Kissomlyó monogenetic volcano (western Pannonian Basin):
1232 evidence from mineral textures, zoning and chemistry. Journal of Volcanology and
1233 Geothermal Research 301, 38–55.

1234 Jankovics, M. É., Taracsák, Z., Dobosi, G., Embey-Isztin, A., Batki, A., Harangi, S. &
1235 Hauzenberger, C. A. (2016). Clinopyroxene with diverse origins in alkaline basalts from the
1236 western Pannonian Basin: Implications from trace element characteristics. Lithos 262, 120–
1237 134.

1238 Kim, J., Park, J.-W., Lee, M. J., Lee, J. I. & Kyle, P. R. (2019). Evolution of Alkalic
1239 Magma Systems: Insight from Coeval Evolution of Sodic and Potassic Fractionation
1240 Lineages at The Pleiades Volcanic Complex, Antarctica. Journal of Petrology 60, 117–150.

1241 Kinzler, R. J. (1997). Melting of mantle peridotite at pressures approaching the spinel
1242 to garnet transition: Application to mid-ocean ridge basalt petrogenesis. *Journal of*
1243 *Geophysical Research: Solid Earth* **102**, 853–874.

1244 Kinzler, R. J. & Grove, T. L. (1992). Primary magmas of mid-ocean ridge basalts 1.
1245 Experiments and methods. *Journal of Geophysical Research: Solid Earth* **97**, 6885–6906.

1246 Klemme, S. (2004). The influence of Cr on the garnet–spinel transition in the Earth's
1247 mantle: experiments in the system MgO–Cr2O3–SiO2 and thermodynamic modelling. *Lithos*
1248 **77**, 639–646.Larter, R. D., Cunningham, A. P., Barker, P. F., Gohl, K. & Nitsche, F. O.
1249 (2002). Tectonic evolution of the Pacific margin of Antarctica 1. Late Cretaceous tectonic
1250 reconstructions. Journal of Geophysical Research: Solid Earth 107, EPM 5-1-EPM 5-19.

Le Maitre, R.W., Streckeisen, A., Zanettin, B., Le Bas, M.J., Bonin, B., Bateman, P., Bellieni, G., Dudek, A., Efremova, S., Keller, J. and Lameyre, J. (Eds.). (2002). Igneous rocks: a classification and glossary of terms: recommendations of the International Union of Geological Sciences Subcommission on the Systematics of Igneous Rocks. Cambridge University Press

Lee, W., Lee, H., Kim, D., Kim, J., Oh, J., Song, J.-H., Kim, C. H., Park, C. H. & Stuart, F. M. (2021). Trace element and helium isotope geochemistry of the Cenozoic intraplate volcanism in the East Sea (Sea of Japan): Implications for lithosphere-asthenosphere interaction. Lithos 388–389, 106075.

Lemarchand, F., Villemant, B. & Calas, G. (1987). Trace element distribution coefficients in alkaline series. *Geochimica et Cosmochimica Acta* **51**, 1071–1081.

Lindsley, D. H. (1983). Pyroxene thermometry. American Mineralogist 68, 477–493.

Loubet, M., Sassi, R. & Di Donato, G. (1988). Mantle heterogeneities: a combined isotope and trace element approach and evidence for recycled continental crust materials in some OIB sources. Earth and Planetary Science Letters 89, 299–315.

Lucassen, F., Pudlo, D., Franz, G., Romer, R. L. & Dulski, P. (2013). Cenozoic intra-plate magmatism in the Darfur volcanic province: mantle source, phonolite-trachyte genesis and relation to other volcanic provinces in NE Africa. International Journal of Earth Sciences 102, 183–205.

Mahood, G. A. & Stimac, J. A. (1990). Trace-element partitioning in pantellerites and trachytes. *Geochimica et Cosmochimica Acta* **54**, 2257–2276.

1272 Mallik, A. & Dasgupta, R. (2012). Reaction between MORB-eclogite derived melts and
1273 fertile peridotite and generation of ocean island basalts. Earth and Planetary Science Letters
1274 329–330, 97–108.

1275 Marshall, P. (1906). The Geology of Dunedin, (New Zealand). Quarterly Journal of the
1276 Geological Society 62, 381–424.

1277 Martin, U. (2000). Eruptions and deposition of volcaniclastic rocks in the Dunedin
1278 volcanic complex, Otago Peninsula, New Zealand. Thesis, University of Otago.

1279 Marzoli, A., Aka, F. T., Merle, R., Callegaro, S. & N'ni, J. (2015). Deep to shallow
1280 crustal differentiation of within-plate alkaline magmatism at Mt. Bambouto volcano,
1281 Cameroon Line. Lithos 220–223, 272–288.

1282 Masotta, M., Pontesilli, A., Mollo, S., Armienti, P., Ubide, T., Nazzari, M. & Scarlato,
1283 P. (2020). The role of undercooling during clinopyroxene growth in trachybasaltic magmas:
1284 Insights on magma decompression and cooling at Mt. Etna volcano. Geochimica et
1285 Cosmochimica Acta 268, 258–276.

1286 Mather, B. R., Müller, R. D., Seton, M., Ruttor, S., Nebel, O. & Mortimer, N. (2020).
1287 Intraplate volcanism triggered by bursts in slab flux. Science Advances. American
1288 Association for the Advancement of Science 6, eabd0953.

1289 McCoy-West, A. J., Baker, J. A., Faure, K. & Wysoczanski, R. (2010). Petrogenesis
1290 and Origins of Mid-Cretaceous Continental Intraplate Volcanism in Marlborough, New
1291 Zealand: Implications for the Long-lived HIMU Magmatic Mega-province of the SW Pacific.
1292 *Journal of Petrology*. Oxford Academic **51**, 2003–2045.

McCoy-West, A. J., Bennett, V. C. & Amelin, Y. (2016). Rapid Cenozoic ingrowth of isotopic signatures simulating "HIMU" in ancient lithospheric mantle: Distinguishing source from process. Geochimica et Cosmochimica Acta 187, 79–101.

McDonough, W. F. & Sun, S. -s. (1995). The composition of the Earth. Chemical Geology 120, 223–253.

McDougall, I. & Coombs, D. S. (1973). Potassium-argon ages for the Dunedin volcano and outlying volcanics. *New Zealand Journal of Geology and Geophysics*. Taylor & Francis **16**, 179–188.

McGee, L. E., Millet, M.-A., Smith, I. E. M., Németh, K. & Lindsay, J. M. (2012). The inception and progression of melting in a monogenetic eruption: Motukorea Volcano, the Auckland Volcanic Field, New Zealand. Lithos 155, 360–374.

McGee, L. E., Smith, I. E. M., Millet, M.-A., Handley, H. K. & Lindsay, J. M. (2013). Asthenospheric Control of Melting Processes in a Monogenetic Basaltic System: a Case Study of the Auckland Volcanic Field, New Zealand. Journal of Petrology 54, 2125–2153.

McKenzie, D. a. N. & O'Nions, R. K. (1991). Partial Melt Distributions from Inversion of Rare Earth Element Concentrations. *Journal of Petrology*. Oxford Academic **32**, 1021–1091.

Médard, E. & Schmidt, M. W., (2008). Composition of low degree hydrous melts of fertile spinel- or garnet-bearing lherzolite. Geochimica et Cosmochimica Acta 72 (12S) A617.

Médard, E., Schmidt, M. W. & Schiano, P. (2004). Liquidus surfaces of ultracalcic primitive melts: formation conditions and sources. *Contributions to Mineralogy and Petrology* **148**, 201–215.

1316 Mollo, S., Blundy, J., Scarlato, P., De Cristofaro, S. P., Tecchiato, V., Di Stefano, F.,
1317 Vetere, F., Holtz, F. & Bachmann, O. (2018). An integrated P-T-H2O-lattice strain model to
1318 quantify the role of clinopyroxene fractionation on REE+Y and HFSE patterns of mafic
1319 alkaline magmas: Application to eruptions at Mt. Etna. Earth-Science Reviews 185, 32–56.

1320 Mollo, S. & Masotta, M. (2014). Optimizing pre-eruptive temperature estimates in
1321 thermally and chemically zoned magma chambers. Chemical Geology 368, 97–103.

1322 Mollo, S., Putirka, K., Misiti, V., Soligo, M. & Scarlato, P. (2013). A new test for
1323 equilibrium based on clinopyroxene–melt pairs: Clues on the solidification temperatures of
1324 Etnean alkaline melts at post-eruptive conditions. Chemical Geology 352, 92–100.

1325 Mollo, S., Ubide, T., Di Stefano, F., Nazzari, M. & Scarlato, P. (2020).
1326 Polybaric/polythermal magma transport and trace element partitioning recorded in single
1327 crystals: A case study of a zoned clinopyroxene from Mt. Etna. *Lithos* **356–357**, 105382.

1328 Morse, S. A. (1980). Basalts and phase diagrams: an introduction to the quantitative use
1329 of phase diagrams in igneous petrology. Springer-Verlag.

1330 Mortimer, N. (2004). New Zealand's Geological Foundations. Gondwana Research 7,
1331 261–272.

1332 Murphy, M. D., Sparks, R. S. J., Barclay, J., Carroll, M. R. & Brewer, T. S. (2000).
1333 Remobilization of Andesite Magma by Intrusion of Mafic Magma at the Soufriere Hills
1334 Volcano, Montserrat, West Indies. Journal of Petrology 41, 21–42.

1335 Namur, O., Charlier, B., Toplis, M.J., Vander Auwera, J., 2012. Prediction of
1336 plagioclase-melt equilibria in anhydrous silicate melts at 1-atm. Contrib Mineral Petrol 163,
1337 133–150. https://doi.org/10.1007/s00410-011-0662-z

Navon, O. & Stolper, E. (1987). Geochemical Consequences of Melt Percolation: The Upper Mantle as a Chromatographic Column. The Journal of Geology. The University of Chicago Press 95, 285–307.

Nazzari, M., Di Stefano, F., Mollo, S., Scarlato, P., Tecchiato, V., Ellis, B., Bachmann, O. & Ferlito, C. (2019). Modeling the Crystallisation and Emplacement Conditions of a Basaltic Trachyandesitic Sill at Mt. Etna Volcano. Minerals 9, 126.

Needham, A. J., Lindsay, J. M., Smith, I. E. M., Augustinus, P. & Shane, P. A. (2011). Sequential eruption of alkaline and sub-alkaline magmas from a small monogenetic volcano in the Auckland Volcanic Field, New Zealand. Journal of Volcanology and Geothermal Research 201, 126–142.

Orejana, D., Villaseca, C. & Paterson, B. A. (2007). Geochemistry of mafic phenocrysts from alkaline lamprophyres of the Spanish Central System: implications on crystal fractionation, magma mixing and xenoliths entrapment within deep magma chambers. European Journal of Mineralogy 19, 817–832.

Palummo, F., Mollo, S., Astis, G. D., Stefano, F. D., Nazzari, M. & Scarlato, P. (2020). Petrological and geochemical modeling of magmas erupted at Vulcano Island in the period 54–8 ka: Quantitative constraints on the sub-volcanic architecture of the plumbing system. Lithos 374–375, 105715.

Panter, K. S., Kyle, P. R. & Smellie, J. L. (1997). Petrogenesis of a Phonolite–Trachyte Succession at Mount Sidley, Marie Byrd Land, Antarctica. Journal of Petrology 38, 1225–1253.

Panter, K. S., Blusztajn, J., Hart, S. R., Kyle, P. R., Esser, R. & Mcintosh, W. C. (2006). The Origin of HIMU in the SW Pacific: Evidence from Intraplate Volcanism in Southern New Zealand and Subantarctic Islands. Journal of Petrology 47, 1673–1704.

1362 Panter, K. S. et al. (2018). Melt Origin across a Rifted Continental Margin: a Case for
1363 Subduction-related Metasomatic Agents in the Lithospheric Source of Alkaline Basalt, NW
1364 Ross Sea, Antarctica. Journal of Petrology 59, 517–558.

1365 Paton, C., Hellstrom, J., Paul, B., Woodhead, J. & Hergt, J. (2011). Iolite: Freeware for
1366 the visualisation and processing of mass spectrometric data. Journal of Analytical Atomic
1367 Spectrometry 26, 2508–2518.

1368 Perinelli, C., Mollo, S., Gaeta, M., De, C. S. P., Palladino, D. M., Armienti, P.,
1369 Scarlato, P. & Putirka, K. D. (2016). An improved clinopyroxene-based hygrometer for
1370 Etnean magmas and implications for eruption triggering mechanisms. American Mineralogist
1371 101, 2774–2777.

1372 Petrus, J. A., Chew, D. M., Leybourne, M. I. & Kamber, B. S. (2017). A new approach
1373 to laser-ablation inductively-coupled-plasma mass-spectrometry (LA-ICP-MS) using the
1374 flexible map interrogation tool 'Monocle.' Chemical Geology 463, 76–93.

1375 Pilet, S., Baker, M. B. & Stolper, E. M. (2008). Metasomatized Lithosphere and the
1376 Origin of Alkaline Lavas. Science 320, 916–919.

1377 Pilet, S. (2015). Generation of low-silica alkaline lavas: Petrological constraints,
1378 models, and thermal implications. Geological Society of America Special Papers. Geological
1379 Society of America, 281–304.

1380 Pin, C., Briot D, Bassin, C., Poitrasson, F. (1994). Concominant Separation of
1381 strontium and samarium–neodymium for isotopic analysis in silicate samples, based on
1382 specific extraction chromatography. Analytical Chimica Acta, 298, 209–217

1383 Pin, C., Gannoun, A. and Dupont, A. (2014). Rapid, simultaneous separation of Sr, Pb,
1384 and Nd by extraction chromatography prior to isotope ratios determination by TIMS and MC-
1385 ICP-MS. Journal of Analytical Atomic Spectrometry, 2014, 29, 1858-1870

1386 Price, R. C. (1972). Geochemical investigations of the alkalic rocks of the Dunedin
1387 volcano, East Otago, New Zealand. Thesis, University of Otago.

1388 Price, R. C. & Chappell, B. W. (1975). Fractional crystallisation and the petrology of
1389 Dunedin volcano. Contributions to Mineralogy and Petrology 53, 157–182.

1390 Price, R. C., Cooper, A. F., Woodhead, J. D. & Cartwright, I. (2003). Phonolitic
1391 Diatremes within the Dunedin Volcano, South Island, New Zealand. Journal of Petrology 44,
1392 2053–2080.

1393 Price, R. C., Gray, C. M. & Frey, F. A. (1997). Strontium isotopic and trace element
1394 heterogeneity in the plains basalts of the Newer Volcanic Province, Victoria, Australia.
1395 Geochimica et Cosmochimica Acta 61, 171–192.

1396 Price, R. C. & Taylor, S. R. (1973). The geochemistry of the Dunedin Volcano, East
1397 Otago, New Zealand: Rare earth elements. Contributions to Mineralogy and Petrology 40,
1398 195–205.

1399 Pu, X., Lange, R. A. & Moore, G. (2017). A comparison of olivine-melt thermometers
1400 based on DMg and DNi: The effects of melt composition, temperature, and pressure with
1401 applications to MORBs and hydrous arc basalts. American Mineralogist 102, 750–765.

1402 Putirka, K. (1999). Clinopyroxene+liquid equilibria to 100 kbar and 2450K.

1403 Contributions to Mineralogy and Petrology 135, 151–163.

1404 Putirka, K. D. (2005). Igneous thermometers and barometers based on plagioclase +
1405 liquid equilibria: Tests of some existing models and new calibrations. American Mineralogist
1406 90, 336–346.

1407 Putirka, K. D. (2008). Thermometers and Barometers for Volcanic Systems. Reviews in
1408 Mineralogy and Geochemistry 69, 61–120.

1409 Putirka, K. D., Mikaelian, H., Ryerson, F. & Shaw, H. (2003). New clinopyroxene-
1410 liquid thermobarometers for mafic, evolved, and volatile-bearing lava compositions, with
1411 applications to lavas from Tibet and the Snake River Plain, Idaho. American Mineralogist 88,
1412 1542–1554.

1413 Putirka, K., Johnson, M., Kinzler, R., Longhi, J. & Walker, D. (1996).
1414 Thermobarometry of mafic igneous rocks based on clinopyroxene-liquid equilibria, 0–30
1415 kbar. Contributions to Mineralogy and Petrology 123, 92–108.

1416 Re, G., Palin, J. M., White, J. D. L. & Parolari, M. (2017). Unravelling the magmatic
1417 system beneath a monogenetic volcanic complex (Jagged Rocks Complex, Hopi Buttes, AZ,
1418 USA). Contributions to Mineralogy and Petrology 172, 94.

1419 Reubi, O., Nicholls, I. A. & Kamenetsky, V. S. (2003). Early mixing and mingling in
1420 the evolution of basaltic magmas: evidence from phenocryst assemblages, Slamet Volcano,
1421 Java, Indonesia. Journal of Volcanology and Geothermal Research 119, 255–274.

1422 Rhodes, J. M., Dungan, M. A., Blanchard, D. P. & Long, P. E. (1979). Magma mixing
1423 at mid-ocean ridges: Evidence from basalts drilled near 22° N on the Mid-Atlantic Ridge.
1424 Tectonophysics 55, 35–61.

1425 Robinson, J. A. C. & Wood, B. J. (1998). The depth of the spinel to garnet transition at
1426 the peridotite solidus. *Earth and Planetary Science Letters* **164**, 277–284.

Roeder, P. L. & Emslie, R. F. (1970). Olivine-liquid equilibrium. Contributions to Mineralogy and Petrology 29, 275–289.

Rollinson, H. R. (1993). *Using Geochemical Data: Evaluation, Presentation, Interpretation*. Routledge.

Sack, R. O., Walker, D. & Carmichael, I. S. E. (1987). Experimental petrology of alkalic lavas: constraints on cotectics of multiple saturation in natural basic liquids. *Contributions to Mineralogy and Petrology* **96**, 1–23.

Scott, J. M., Hodgkinson, A., Palin, J. M., Waight, T. E., van der Meer, Q. H. A. & Cooper, A. F. (2014a). Ancient melt depletion overprinted by young carbonatitic metasomatism in the New Zealand lithospheric mantle. Contributions to Mineralogy and Petrology 167, 963.

Scott, J. M., Waight, T. E., Meer, Q. H. A. van der, Palin, J. M., Cooper, A. F. & Münker, C. (2014b). Metasomatized ancient lithospheric mantle beneath the young Zealandia microcontinent and its role in HIMU-like intraplate magmatism. Geochemistry, Geophysics, Geosystems 15, 3477–3501.

Scott, J. M., Brenna, M., Crase, J. A., Waight, T. E., van der Meer, Q. H. A., Cooper, A. F., Palin, M. J., Le Roux, P. & Münker, C. (2016). Peridotitic Lithosphere Metasomatized by Volatile-bearing Melts, and its Association with Intraplate Alkaline HIMU-like Magmatism. Journal of Petrology 57, 2053–2078.

Scott, J. M., Pontesilli, A., Brenna, M., White, J. D. L., Giacalone, E., Palin, J. M. & Roux, P. J. le (2020a). The Dunedin Volcanic Group and a revised model for Zealandia's alkaline intraplate volcanism. New Zealand Journal of Geology and Geophysics 0, 1–20.

Scott, J. M., White, J. D. L. & Roux, P. J. le (2020b). Intraplate volcanism on the Zealandia Eocene-Early Oligocene continental shelf: the Waiareka-Deborah Volcanic Field, North Otago. *New Zealand Journal of Geology and Geophysics*. Taylor & Francis **0**, 1–19.

Seaman, S. J. (2000). Crystal Clusters, Feldspar Glomerocrysts, and Magma Envelopes in the Atascosa Lookout Lava Flow, Southern Arizona, USA: Recorders of Magmatic Events. Journal of Petrology 41, 693–716.

Self, S. & Gunn, B. M. (1976). Petrology, volume and age relations of alkaline and saturated peralkaline volcanics from Terceira, Azores. Contributions to Mineralogy and Petrology 54, 293–313.

Serre, S. H., Meer, Q. H. A. van der, Waight, T. E., Scott, J. M., Münker, C., Thomsen, T. B. & Roux, P. J. le (2020). Petrogenesis of amphibole megacrysts in lamprophyric intraplate magmatism in southern New Zealand. *New Zealand Journal of Geology and Geophysics*. Taylor & Francis **63**, 489–509.

Smith, I. E. M., Blake, S., Wilson, C. J. N. & Houghton, B. F. (2008). Deep-seated fractionation during the rise of a small-volume basalt magma batch: Crater Hill, Auckland, New Zealand. Contributions to Mineralogy and Petrology 155, 511–527.

Spath, A., Le Roex, A. P. & Opiyo-Akech, N. (2001). Plume–lithosphere interaction and the origin of continental rift-related alkaline volcanism—the Chyulu Hills Volcanic Province, southern Kenya. Journal of Petrology 42, 765–787.

Sprung, P., Schuth, S., Münker, C. & Hoke, L. (2007). Intraplate volcanism in New Zealand: the role of fossil plume material and variable lithospheric properties. Contributions to Mineralogy and Petrology 153, 669–687.

1471 Stormer, J. C. & Nicholls, J. (1978). XLFRAC: a program for the interactive testing of
1472 magmatic differentiation models. Computers & Geosciences **4**, 143–159.

1473 Stracke, A., Hofmann, A. W. & Hart, S. R. (2005). FOZO, HIMU, and the rest of the
1474 mantle zoo. Geochemistry, Geophysics, Geosystems 6 , Q05007,
1475 doi:10.1029/2004GC000824.

1476 Streck, M. J. (2008). Mineral Textures and Zoning as Evidence for Open System
1477 Processes. Reviews in Mineralogy and Geochemistry 69, 595–622.

1478 Stroncik, N. A., Klügel, A. & Hansteen, T. H. (2008). The magmatic plumbing system
1479 beneath El Hierro (Canary Islands): constraints from phenocrysts and naturally quenched
1480 basaltic glasses in submarine rocks. Contributions to Mineralogy and Petrology 157, 593.

1481 Tanaka T, et al. (2000) JNdi-1: a neodymium isotopic reference in consistency with
1482 LaJolla neodymium. Chemical Geology, 168, 279–281

1483 Timm, C., Hoernle, K., Werner, R., Hauff, F., den Bogaard, P. van, White, J.,
1484 Mortimer, N. & Garbe-Schönberg, D. (2010). Temporal and geochemical evolution of the
1485 Cenozoic intraplate volcanism of Zealandia. Earth-Science Reviews 98, 38–64.

1486 Ubide, T., Galé, C., Larrea, P., Arranz, E. & Lago, M. (2014). Antecrysts and their
1487 effect on rock compositions: The Cretaceous lamprophyre suite in the Catalonian Coastal
1488 Ranges (NE Spain). Lithos 206–207, 214–233.

1489 Ubide, T. & Kamber, B. S. (2018). Volcanic crystals as time capsules of eruption
1490 history. Nature Communications 9, 1–12.

1491 Ubide, T., McKenna, C. A., Chew, D. M. & Kamber, B. S. (2015). High-resolution LA-
1492 ICP-MS trace element mapping of igneous minerals: In search of magma histories. Chemical
1493 Geology 409, 157–168.

1494 Ubide, T., Mollo, S., Zhao, J., Nazzari, M. & Scarlato, P. (2019). Sector-zoned
1495 clinopyroxene as a recorder of magma history, eruption triggers, and ascent rates.
1496 Geochimica et Cosmochimica Acta 251, 265–283.

1497 van der Meer, Q. H. A., Storey, M., Scott, J. M. & Waight, T. E. (2016). Abrupt spatial
1498 and geochemical changes in lamprophyre magmatism related to Gondwana fragmentation
1499 prior, during and after opening of the Tasman Sea. Gondwana Research 36, 142–156.

1500 Vernières, J., Godard, M. & Bodinier, J.-L. (1997). A plate model for the simulation of
1501 trace element fractionation during partial melting and magma transport in the Earth's upper
1502 mantle. Journal of Geophysical Research: Solid Earth 102, 24771–24784.

1503 Walter, M. J. (1998). Melting of Garnet Peridotite and the Origin of Komatiite and
1504 Depleted Lithosphere. Journal of Petrology 39, 29–60.

1505 Wanke, M., Clynne, M. A., von Quadt, A., Vennemann, T. W. & Bachmann, O. (2019).
1506 Geochemical and petrological diversity of mafic magmas from Mount St. Helens.
1507 Contributions to Mineralogy and Petrology 174, 10.

1508 Wass, S. Y. & Rogers, N. W. (1980). Mantle metasomatism—precursor to continental
1509 alkaline volcanism. Geochimica et Cosmochimica Acta **44**, 1811–1823.

1510 Weaver, S. D., Smith, I. E. M., Sewell, R. J., Gamble, J. A. & Pankhurst, R. J. (1989).
1511 New Zealand intraplate volcanism: isotope geochemistry. In: Johnson, R. W. (ed.) Intraplate
1512 volcanism in eastern Australia and New Zealand. Cambridge: Cambridge University Press,
1513 185–187.

1514 Weis, D. et al. (2006). High-precision isotopic characterization of USGS reference
1515 materials by TIMS and MC-ICP-MS. Geochemistry, Geophysics, Geosystems 7 , Q08006,
1516 doi:10.1029/2006GC001283.

White, J. C., Espejel-García, V. V., Anthony, E. Y. & Omenda, P. (2012). Open System evolution of peralkaline trachyte and phonolite from the Suswa volcano, Kenya rift. Lithos 152, 84–104.

Willbold, M. & Stracke, A. (2010). Formation of enriched mantle components by recycling of upper and lower continental crust. Chemical Geology 276, 188–197.

Wilson, M., Downes, H. & Cebriá, J.-M. (1995). Contrasting Fractionation Trends in Coexisting Continental Alkaline Magma Series; Cantal, Massif Central, France. Journal of Petrology 36, 1729–1753.

Wolff, J. A. (2017). On the syenite-trachyte problem. Geology 45, 1067–1070.

Wright, J. B. (1971). The phonolite-trachyte spectrum. Lithos 4, 1–5.

Xing, C.-M. & Wang, C. Y. (2020). Periodic Mixing of Magmas Recorded by Oscillatory Zoning of the Clinopyroxene Macrocrysts from an Ultrapotassic Lamprophyre Dyke. Journal of Petrology 61.

Xu, Y.-G., Ma, J.-L., Frey, F. A., Feigenson, M. D. & Liu, J.-F. (2005). Role of lithosphere–asthenosphere interaction in the genesis of Quaternary alkali and tholeiitic basalts from Datong, western North China Craton. Chemical Geology 224, 247–271.

Yang, J. & Faccenda, M. (2020). Intraplate volcanism originating from upwelling hydrous mantle transition zone. Nature. Nature Publishing Group 579, 88–91.

Zack, T. and Brumm, R. (1998). Ilmenite/liquid partition coefficients of 26 trace elements determined through ilmenite/clinopyroxene partitioning in garnet pyroxene. In: 7th International Kimberlite Conference. Gurney, J.J., Gurney, J.L., Pascoe, M.D. and Richardson, S.H. (Editors), Red Roof Design, Cape Town. 986-988.

Ziem à Bidias, L. A., Chauhan, H., Mekala, R. M. & Rao, N. V. C. (2021). Green core clinopyroxenes from basanites of Petpenoun volcanoes, Noun Plain, Cameroon volcanic line: chemistry and genesis. Bulletin of Volcanology 83, 13.

Figure captions

Fig. 1. Satellite photo of the Dunedin Volcano with sample locations and outlines of volcanic outcrops. Base image from Google Earth, Landsat, Copernicus, DigitalGlobe.

Fig. 2. Chemical classification of Dunedin Volcano basalts. (a) Total alkalis vs silica (TAS) classification (Le Maitre et al., 2002) of high-, mid-, and low-alkali basalts from this study. Literature whole rock compositions from Scott et al. (2020a) are plotted for comparison. (b) Alkali index [$(Na_2O+K_2O)/SiO_2$] vs. Mg# [molar 100 × Mg / (Mg + Fe^T)] diagram, used as criteria for classification of low-, mid-, and high-alkali basalts.

Fig. 3. Representative thin section photomicrographs in plane-polarised light (PPL) and cross-polarised light (XPL) of eruptive products at Dunedin Volcano. (a) High-alkali basalt (sample DVB1a) with main phenocryst assemblage including olivine, clinopyroxene and subordinate titanomagnetite, in a groundmass of plagioclase, clinopyroxene, titanomagnetite, and minor olivine (PPL) and (b) glomerocryst of clinopyroxene with prominent sector (hourglass) and oscillatory zoning (XPL). (c) High-alkali basalt (sample DVB2c) with clinopyroxene and plagioclase phenocrysts, in a groundmass of abundant plagioclase, clinopyroxene, and titanomagnetite (PPL). (d) Low-alkali basalt (sample DVB5b) with phenocrysts of light grey cores and pink clinopyroxene crystals, olivine, plagioclase, and titanomagnetite, with plagioclase crystals displaying sieve-textured mantles, in a groundmass of plagioclase, clinopyroxene, olivine and titanomagnetite (PPL). (e) Large clinopyroxene crystals in low-alkali basalt (sample DVB7) display either patchy interiors and/or patchy

overgrowth rims. Light grey cores are recognizable by low birefringence, have more homogeneous interiors and resorbed inner rims (XPL). (f) Plagioclase phenocrysts in low-alkali basalt (sample DVB5a) with resorbed cores and sieve-textured mantle (XPL). (g) Mid-alkali basalt (sample DVB4a) with similar textural features to LABs, with a phenocryst assemblage of clinopyroxene with either pink or grey cores, plagioclase with resorbed interiors, olivine and titanomagnetite, in a groundmass made by the same phase assemblage (PPL). (h) Large clinopyroxene crystal with homogeneous interior and patchy overgrowths in a mid-alkali basalt (sample DVB4c) (XPL).

Fig. 4. Backscattered electron (BSE) photomicrographs of main phenocryst types from high-, mid-, and low-alkali basalts at Dunedin Volcano. (a) Olivine crystals from low-alkali basalt sample DVB5b, including darker type 1 Fo-rich olivine, sharing same compositional features as olivine from high-alkali basalts, along with brighter type 2 Fo-poor olivine. (b) Clinopyroxene type 1 in high-alkali basalt sample DVB1b showing oscillatory and sector (hourglass) zoning. A dark (Mg and Cr-rich) band (Cr-recharge zone) is overgrown by a brighter (Al and Ti-rich) rim. (c) Green clinopyroxene resorbed core type 2, overgrown by type 1 zoned mantle in high-alkali basalt sample DVB2c. (d) Mg- and Cr-rich clinopyroxene resorbed type 3 core from low-alkali basalt sample DVB5a, overgrown by mantle having clinopyroxene type 4 mantle, a darker Cr-recharge zone and a brighter overgrowth rim. (e) Uniform clinopyroxene type 4 in mid-alkali basalt sample DVB4a. (f) An-poor resorbed core, overgrown by an almost euhedral An-rich rim, in low-alkali basalt sample DVB5b. (g) Plagioclase crystal with oscillatory zoning and An content decreasing towards the rim (type 2) from high-alkali basalt sample DVB4d. (h) Titanomagnetite phenocryst from mid-alkali basalt sample DVB2b.

Fig. 5. Compositional characterization of olivine phenocrysts in the Dunedin Volcano. Type 1 olivines have unzoned to normally zoned forsterite-rich compositions (Fo_{81-87}), while

type 2 crystals are unzoned to inversely zoned with forsterite-poor compositions (Fo_{73-81}), and rim compositions of both olivine types have the lowest forsterite contents (Fo_{55-75}).

Fig. 6. Compositional characterization of clinopyroxene phenocrysts in basaltic rocks of the Dunedin Volcano in Al+Ti (apfu: atoms per formula units) vs. Mg# [molar 100 × Mg / (Mg + Fe^T)] compositional space, including frequency histograms.

Fig. 7. Compositional variations of selected major elements, end-member components and trace elements in clinopyroxene populations in basaltic rocks of the Dunedin Volcano. Note that the scale for Cr is logarithmic, due to the very large variations in the abundance of this element (Mg# [molar 100 × Mg / (Mg + Fe^T)]; Hd: Hedenbergite; ∑Ts: CaTi-Tschermak + CaFe-Tschermak + CaCr-Tschermak).

Fig. 8. Laser ablation inductively coupled plasma mass spectrometry (LA-ICP-MS) trace element maps of clinopyroxene populations in basaltic rocks of the Dunedin Volcano. Selected trace element concentrations are shown with cool-warm colour scales. The maps are quantitative for clinopyroxene and semi-quantitative for other phases (inclusions and groundmass). (a) Type 1 clinopyroxene, characterised by oscillatory and sector (hourglass) zoning, with La and Zr enrichments in prism sectors. Oscillatory zoning determines large variations in Sc, Zr and La. A prominent Cr-rich zone is also evident, corresponding to a darker (diopside-rich) growth horizon in the BSE photomicrograph. (b) Green core clinopyroxene (type 2), characterised by low abundances of Cr, Ni, and Sc, and high abundances of Zr and La. The green core is overgrown by a type 1 zoned mantle, displaying large variations in Sc, Zr and La. The crystal also features a Cr-rich zone towards the crystal outer rim, also enriched in Ni. (c) Mafic resorbed core (type 3) enriched in diopside and compatible trace elements, overgrown by a titanaugitic type 4 mantle, uniform in composition and relatively poor in Zr and La, and then a Cr- rich zone. (d) Type 4 clinopyroxene, showing

faint core to rim zoning. Cr increases in the outer interior and inner rim of the crystal, whereas Ni shows an overall decrease from core to overgrowth rim.

Fig. 9. Chemical classification of Fe-Ti oxide phenocrysts in Dunedin Volcano high-, mid- and low-alkali basalt samples.

Fig. 10. Compositional classification of plagioclase phenocrysts in Dunedin Volcano basaltic samples, plotted in terms of relative proportions of Anorthite, Albite and Orthoclase components.

Fig. 11. Selected major elements vs. Mg# variation diagrams for Dunedin Volcano whole rock data. Literature data from Scott et al. (2020a) are shown for comparison.

Fig. 12. Selected trace elements vs. Mg# variation diagrams for Dunedin Volcano whole rock data. Literature data from Scott et al., 2020a are shown for comparison.

Fig. 13. (a) Primitive mantle normalised extended element plot for basaltic rocks of the Dunedin Volcano. Primitive mantle normalization values are from McDonough & Sun (1995). (b) Chondrite normalised REE plots for basaltic rocks of the Dunedin Volcano. Data normalised to chondrite CI of McDonough & Sun (1995). Results of non-modal batch melting models of metasomatised lithospheric mantle are shown with labels indicating extent of partial melting (%) (further details in text and Table S9).

Fig. 14. Isotopic compositions of whole rocks from this study. Literature data from Scott et al. (2014a, 2014b, 2020a). HIMU and FOZO (young-HIMU) isotopic compositional fields are from Stracke et al. (2005), EMII fields are from Hart (1988) and Hart et al. (1992). Mixing lines between high- and mid-alkali basalts (sample DVB1a) and the hypothetical EMII-like composition of the asthenospheric mantle source (Table S9) are shown with 10% step mixing marks.

Fig. 15. (a) Probability density functions (PDF) of olivine-based temperature estimates calculated with the model of Pu et al. (2017). PDF represent the relative likelihood of the sample having a certain temperature value. (b) Temperature vs. fO_2 for oxide phenocrysts calculated with the model of Aryaeva et al. (2018). (c) PDF of oxygen fugacity estimates are expressed as log units above and below the Fayalite-Magnetite-Quartz (FMQ) buffer. (d) Plagioclase-based temperature calculated with the model of Putirka (2005). (e) Melt-H_2O contents estimated for melts in equilibrium with plagioclase phenocrysts by using the model of Putirka (2005).

Fig. 16. (a) Probability density functions (PDF) of clinopyroxene-based temperature and (b) pressure estimates obtained using the thermobarometer of Putirka et al. (2003). (c) Melt-H_2O contents equilibrium with clinopyroxene have been estimated using the model of Perinelli et al. (2016).

Fig. 17. Schematic representation of the complex plumbing system envisaged for the Dunedin Volcano. Different clinopyroxene types are distinguished according to the colour legend, while no colour distinctions are made for olivine and plagioclase crystals. Inset BSE photomicrographs and trace elements maps display the main textural features of low-, mid-, and high-alkali basalts. From left to right, higher degrees of interaction between asthenospheric derived melts and the lithospheric mantle generate peripheral high-alkali basalts. The increasing petrographic complexity of the crystalline cargo, with clinopyroxene green core type 2 and plagioclase type 2 from high- and mid-alkali basalts indicates the increasing development of the plumbing system at middle crustal depths, in the central sectors of the Dunedin Volcano. To the right, the central area of the volcano where low- and mid-alkali basalts were erupted, displays more complex mantle to crust pathways, fed by inputs of asthenosphere-derived EMII-like melts.

Fig. 18. Fertile peridotite partial melting and interaction model between the asthenospheric melts and the lithospheric wall-rock, aimed at reproducing the hypothesised asthenospheric mantle-derived primary magma, responsible for the EMII-like signature of low-alkali basalts at Dunedin Volcano. Interaction is best simulated by mixing the products of 5-10% lherzolite partial melting with 20-40% of the metasomatised lithospheric mantle melt (5% degree of partial melting), considering entrainment of 10% excess clinopyroxene in the resulting magma after interaction. (a) Primitive mantle normalised trace element concentrations of low-alkali basalts (averaged composition), SCLM-derived melt (as in Fig. 14a), fertile peridotite melt and mixed melt (dashed lines every 10% step of mixing; yellow field defines 20-40% mixing interval). (b) Total Alkali vs Silica (Le Maitre et al., 2002) plot and (c) alkali index [$(Na_2O + K_2O)/SiO_2$] vs Mg# display major element compositions of the primary magmas reconstructed for the Dunedin Volcano and the mixed magmas at 20%, 30% and 40% of lithospheric contribution. Further details in text and Table S9.

Table 1. Summary of modal abundances (estimated maximum) and occurrence of phenocryst types in basaltic rocks of the Dunedin Volcano, including whole rock Mg# and sampling localities.

Table 2. Major and trace element compositions (in wt.% and ppm units, respectively) of basalts from the Dunedin Volcano. Mg# [molar 100 × $Mg/(Mg+Fe^T)$ on molar basis], alkali index [$(Na_2O+K_2O)/SiO_2$], and CIPW normative distinction between silica-saturated (qz-norm), transitional (hy-norm) and critically silica-undersaturated (ne-norm) basalts (CIPW norms calculated assuming $Fe^{3+}/Fe^T = 0.85$).

Table 3. Sr, Nd and Pb isotopic compositions of basaltic rocks from the Dunedin Volcano. Initial ratios for Sr and Nd isotopic compositions are age-corrected at 13 Ma.

Table 4. Summary of crystallisation conditions estimated on the basis of thermometers, barometers, hygrometers and oxygen barometers for the different crystal populations in basaltic rocks of the Dunedin Volcano. Listed amounts of crystals have been used to model equilibrium melt compositions by subtracting them from whole rock compositions, in order to attain equilibrium between each crystal type and whole rock compositions. In each sample, mineral compositions removed are represented by the average of crystal core compositions in the sample. Further details on thermobarometry and mineral-melt equilibria in text.

Fig. S1. Crystal-melt equilibrium criteria for olivine, titanomagnetite, and plagioclase in basaltic rocks of the Dunedin Volcano. (a) Mg-Fe equilibrium plots for olivine crystals (after Rhodes, 1979), with Kd(Fe-Mg) after Roeder & Emslie (1970). (b) Titanomagnetite ulvospinel measured vs. predicted component, as calculated with the model of Aryaeva et al. (2018). (c) Plagioclase measured vs. predicted (Putirka, 2005) anorthite concentration.

Fig. S2. Crystal-melt equilibrium criteria for clinopyroxene in basaltic rocks of the Dunedin Volcano. (a) Mg-Fe equilibrium plots (after Rhodes, 1979), with Kd(Fe-Mg) after Putirka (2008). (b) Measured vs. predicted (Putirka, 1999) DiHd components after Mollo et al. (2013). (c) Measured Na concentration vs. predicted with the model of Blundy et al. (1995). (d) Measured vs. predicted Ti concentration with the model of Mollo et al., (2018).

Fig. S3. Primitive mantle normalised plot (Macdonough & Sun, 1995) derived by Rayleigh fractional crystallisation (FC) equation. Starting compositions for high-alkali basalt (sample DVB6) and mid-alkali basalt (sample DVB2a) for FC models are shown along with differentiated (low Mg#) high-alkali basalts compositions and modelling results (amount of residual liquid F, chosen on the basis of major elements modeling). Further details in text and Table S10.

			clinopyroxene				olivine		plagioclase			Ilmenite	Titanomagnetite	modal abundances (%)			
sample	Mg#	locality	type 1	type 2	type 3	type 4	type 1	type 2	An-cores	type 1	type 2			cpx	ol	pl	ox
		Low Alkali Basalt															
DVB5b	54	Hoopers Inlet			x	x	x	x		x		x	x	27	4	9	1
DVB5a	66	Hoopers Inlet, below Varleys Hill			x	x	x	x		x		x	x	24	7	6	1
DVB5c	53	Hoopers Inlet, below Varleys Hill			x	x	x			x			x	20	6	9	<1
DVB7	65	Sandymount			x	x	x	x		x		x	x	28	6	13	<1
DVB8a	52	Allans Beach			x	x	x	x		x			x	18	4	10	1
		Mid Alkali Basalt															
DVB4a	52	Harbour cone (bottom)			x	x	x	x		x			x	16	7	16	<1
DVB4b	54	Harbour cone (bottom)				x	x	x		x			x	15	3	9	<1
DVB4c	52	Harbour cone (bottom)				x	x			x			x	9	3	9	1
DVb8c	40	Allans Beach	x			x					x		x	10		16	<1
DVB2a	62	St. Clair (second beach)	x	x			x		x					13	8	1	
DVB2b	63	St. Clair (second beach)	x	x			x						x	6	12		<1
DVB1c	63	Swampy Smt.	x				x							17	7		
		High Alkali Basalt															
DVB6	56	Mt. Holmes	x	x			x		x			x	x	12	8	1	<1
DVB9	38	Sandymount Rd.	x	x									x	13		13	1
DVB8d	34	Allans Beach															
DVB8b	52	Allans Beach	x	x			x			x		x	x	15	3	4	1
DVB4d	43	Harbour cone (top)	x	x				x			x			10		12	
DVB10	43	Waitati	x	x				x			x		x	11	1	15	<1
DVB1a	59	Swampy Smt.	x				x							13	6		
DVB1b	59	Swampy Smt.	x				x							12	6		
DVB3	54	Taiaroa Head	x				x						x	8	4		<1
DVB2c	35	St. Clair (second beach)	x	x							x		x	11		9	1

Table 1. Summary of modal abundances (estimated maximum) and occurrence of phenocrysts types in basaltic rocks of the Dunedin Volcano, including whole rock Mg# and sampling localities.

	DVB5b	DVB5a	DVB5c	DVB7	DVB8a	DVB4a	DVB4b	DVB4c	DVb8c	DVB2a	DVB2b	DVB1c	DVB6	DVB9	DVB8d	DVB8b	DVB4d	DVB10	DVB1a	DVB1b	DVB3	DVB2c
SiO_2	47.84	46.53	48.20	44.79	50.47	45.91	45.38	45.65	48.80	44.84	44.16	45.69	45.54	47.15	49.45	49.16	50.60	50.05	46.13	46.18	46.85	51.08
TiO_2	2.39	2.15	2.41	2.51	2.87	3.38	3.42	3.37	2.83	2.46	2.62	2.12	2.42	3.03	2.90	2.47	2.06	2.24	2.05	2.03	1.95	2.02
Al_2O_3	14.53	11.86	14.68	11.81	14.91	15.84	14.92	16.00	16.41	13.43	12.97	13.29	14.39	16.26	17.95	15.06	17.20	16.55	14.40	14.35	14.98	16.99
FeO^T	11.45	11.21	11.44	11.73	9.94	11.61	12.20	11.83	11.36	11.94	12.56	11.80	12.16	12.51	11.45	11.21	9.26	10.51	11.35	11.50	10.93	11.14
MnO	0.13	0.15	0.11	0.16	0.18	0.17	0.17	0.17	0.21	0.25	0.20	0.19	0.19	0.22	0.20	0.20	0.16	0.35	0.21	0.20	0.20	0.25
MgO	7.64	12.33	7.17	12.33	6.05	6.96	7.96	7.26	4.33	10.97	12.16	11.24	8.51	4.38	3.27	6.93	3.84	4.37	9.29	9.28	7.12	3.33
CaO	10.79	11.41	10.61	12.53	11.39	10.98	11.23	10.95	10.79	10.41	9.38	10.18	9.74	9.36	7.55	9.88	7.77	7.68	9.74	9.00	8.00	6.66
Na_2O	2.68	2.32	2.79	2.12	2.78	2.90	3.19	2.88	3.37	2.76	2.75	2.68	3.52	3.78	3.83	3.32	4.79	3.96	3.70	4.08	5.32	4.28
K_2O	0.93	0.85	0.94	0.68	1.11	1.10	0.77	1.09	1.09	1.07	1.15	1.01	1.40	1.46	1.99	1.96	2.57	2.32	1.43	1.49	2.27	2.30
P_2O_5	0.36	0.27	0.35	0.39	0.39	0.48	0.50	0.48	0.42	0.43	0.58	0.38	0.56	0.84	1.04	0.47	0.55	0.61	0.43	0.43	0.85	0.73
Total	98.73	99.08	98.70	99.03	100.09	99.34	99.75	99.67	99.62	98.57	98.53	98.60	98.42	98.99	99.62	100.66	98.80	98.63	98.74	98.54	98.49	98.78
Mg#	54	66	53	65	52	52	54	52	40	62	63	63	56	38	34	52	43	43	59	59	54	35
alkali index	0.075	0.068	0.077	0.062	0.077	0.087	0.087	0.087	0.091	0.086	0.088	0.081	0.108	0.111	0.118	0.107	0.145	0.125	0.111	0.121	0.162	0.129
norm qz																						
norm ne		2.76		4.68		3.12	5.38	3.58	0.48	5.83	5.57	3.94	7.75	3.15		3.31	6.71	1.64	9.19	10.43	15.99	
norm hy	2.34		3.65		10.26										5.97							1.46
Cs	1.14	1.59	1.15	0.47	0.47	0.67	1.06	1.3	2.23	0.47	0.37	0.22	0.45	1.37	1.99	0.8	1.47	0.85	0.54	0.72	0.75	0.43
Rb	22.5	21.1	22.9	14.9	25.8	25.8	13.1	26.5	32.3	19.8	24.1	23.6	31.1	43.8	40.2	51.1	67.6	46	39.2	41	49.1	48.6
Ba	198	261	218	212	271	296	261	288	248	436	360	287	379	452	526	368	776	1285	420	436	729	656
Th	2.98	3	3.16	3.38	3.93	3.57	3.36	3.51	3.43	3.7	5.12	4.25	4.46	5.96	6.99	6.77	9.45	8.49	7.36	7.54	9.87	9.11
U	0.79	0.85	0.8	0.92	0.93	0.98	0.93	0.95	0.93	1.05	1.37	1.12	1.22	1.56	1.83	1.76	2.38	2.25	2.52	2.07	2.66	2.33
Ta	1.8	1.8	1.9	2.3	2.1	2.7	2.4	2.6	3.8	3.1	3.8	2.9	3.4	4.2	5.5	3.4	4.8	4.9	4.4	4.5	5.9	5
Nb	28.4	27.2	28.5	35.1	31.6	41.5	39	41.5	34.6	49.6	61.7	48.1	59.4	66.7	95.6	55.9	76.7	78.5	71.6	73.5	95.6	85.3
La	21.4	20.5	22.4	26.6	26.5	29.7	29.6	28.9	24.9	32.3	42.7	31.8	38.3	51.1	59.2	40.1	58.7	57.9	47.5	49.4	74.3	64
Ce	45.4	42.3	47.4	55.1	55.6	60.9	60.9	59.9	52.9	64.1	83.4	61.4	77.1	102	118	79.8	110	111.5	89	91	140.5	123
Pb	1	7	7	4	4	2	4	3	1	3	3	2	3	4	1	8	11	8	7	2	4	7

Pr	5.74	5.16	6.05	6.67	6.7	7.25	7.29	6.98	6.45	7.41	9.48	6.92	8.61	12	13.1	9.23	12.2	12.55	9.57	9.85	15.8	13.95
Sr	503	429	503	499	514	868	808	881	482	573	700	482	744	845	865	571	919	819	721	735	1075	712
Nd	24	20.5	26	25.6	26.3	28.7	28.6	27	26.4	29.1	36.7	26.3	33.9	47	50.4	35.3	43.4	46.7	34.9	34.9	57.4	51.5
Zr	160	136	171	159	180	180	171	175	175	189	238	179	224	270	282	266	284	302	253	256	368	338
Hf	4	3.5	4.4	4	4.5	4.3	4	4.2	4.6	4.6	5.4	4.2	5.3	6	6.3	6.1	6.3	6.7	5.3	5.6	7.8	7.1
Sm	5.27	4.58	5.73	5.54	5.73	5.91	6.01	5.94	5.88	6.07	7.2	5.51	6.87	9.14	10.05	6.96	8.45	9.41	6.84	7.12	10.1	9.77
Eu	1.79	1.51	1.84	1.83	1.86	1.98	2.04	2	1.96	1.93	2.35	1.79	2.2	2.91	3.2	2.07	2.9	2.79	2.24	2.38	3.22	3.35
Gd	5.38	4.58	5.46	5.21	5.65	5.56	5.65	5.61	6.01	5.95	6.33	5.49	6.56	8.47	9.1	6.64	6.73	7.91	6.45	6.33	8.67	8.99
Tb	0.77	0.67	0.83	0.76	0.81	0.78	0.77	0.76	0.88	0.83	0.94	0.78	0.9	1.12	1.29	0.94	0.95	1.16	0.92	0.93	1.24	1.24
Dy	4.32	3.87	4.3	4.26	4.6	4.17	4.17	4.21	4.79	4.84	5.29	4.54	4.76	6.26	6.98	5.15	5.38	6.28	4.9	5.15	6.56	7.29
Y	20.8	19.3	20.8	18.9	22.2	19.7	19.4	18.9	22.8	21.7	23.7	21.3	23.6	29.2	34.8	25.6	24.5	28.5	24.3	24.8	29.7	35.2
Ho	0.83	0.7	0.85	0.79	0.84	0.79	0.78	0.78	0.9	0.87	0.95	0.84	0.91	1.19	1.35	0.98	0.96	1.12	0.93	0.99	1.19	1.41
Er	2.17	1.94	2.2	1.91	2.23	1.92	2.03	1.85	2.36	2.28	2.3	2.06	2.37	3.2	3.63	2.64	2.54	2.87	2.48	2.69	3.1	3.67
Yb	1.63	1.57	1.75	1.51	1.79	1.62	1.47	1.51	1.77	1.81	1.85	1.82	1.77	2.49	2.81	2.11	1.99	2.52	2.08	2.18	2.57	3.26
Lu	0.24	0.21	0.25	0.2	0.26	0.23	0.2	0.22	0.26	0.25	0.27	0.28	0.27	0.34	0.4	0.29	0.27	0.37	0.32	0.33	0.38	0.48
Cr	450	620	420	600	400	240	280	220	100	490	420	450	330	80	10	260	60	80	350	350	240	40
V	291	298	274	327	357	275	279	270	321	234	214	208	246	208	132	244	163	155	185	189	149	85
Ni	183	231	169	206	120	112	127	99	57	252	281	235	162	44	13	104	39	57	197	220	144	22
Sc	26	30	25	32	27	19	19	17	23	24	19	23	22	14	9	20	12	11	19	20	13	10

Table 2: Major and trace element composition (in wt.% and ppm units, respectively) of basalts from the Dunedin Volcano. Includes Mg# [molar 100 $\times$ Mg/(Mg+Fe^T)], alkali index [(Na_2O+K_2O)/SiO_2], and CIPW normative distinction between silica-saturated (qz-norm), transitional (hy-norm) and critically silica undersaturated (ne-norm) basalts (CIPW norms calculated assuming $Fe^{3+}/Fe^T = 0.85$).

sample	$^{87}Sr / ^{86}Sr$	± 2σ	$(^{87}Sr / ^{86}Sr)_{initial}$	$^{143}Nd / ^{144}Nd$	± 2σ	$(^{143}Nd / ^{144}Nd)_{initial}$	$^{208}Pb / ^{204}Pb$	± 2σ	$^{207}Pb / ^{204}Pb$	± 2σ	$^{206}Pb / ^{204}Pb$	± 2σ
DVB5b	0.70347	0.00001	0.70344	0.51288	0.00001	0.51287	39.091	0.005	15.647	0.002	19.307	0.001
DVB5a	0.70400	0.00001	0.70397	0.51285	0.00002	0.51284	39.088	0.003	15.658	0.001	19.293	0.001
DVB7	0.70329	0.00001	0.70327	0.51287	0.00002	0.51286	39.474	0.003	15.666	0.001	19.793	0.001
DVB8a	0.70377	0.00001	0.70374	0.51283	0.00002	0.51282	39.085	0.003	15.653	0.001	19.278	0.001
DVB2a	0.70297	0.00001	0.70295	0.51293	0.00001	0.51292	39.486	0.003	15.686	0.001	19.806	0.001
DVB4a	0.70317	0.00001	0.70315	0.51289	0.00001	0.51288	39.515	0.004	15.666	0.001	19.876	0.001
DVB10	0.70282	0.00001	0.70280	0.51294	0.00001	0.51292	39.547	0.003	15.658	0.001	20.075	0.001
DVB1c	0.7028	0.00001	0.70277	0.51292	0.00001	0.51291	39.670	0.004	15.667	0.001	20.227	0.001
DVB6	0.70290	0.00001	0.70288	0.51292	0.00001	0.51291	39.622	0.004	15.652	0.001	19.348	0.001
DVB1a	0.70288	0.00001	0.70285	0.51295	0.00001	0.51294	39.727	0.003	15.675	0.001	20.265	0.001
DVB3	0.70290	0.00001	0.70287	0.51292	0.00001	0.51291	39.695	0.003	15.664	0.001	20.176	0.001
DVB4d	0.70319	0.00001	0.70315	0.51287	0.00002	0.51285	39.309	0.004	15.657	0.001	19.628	0.001

Table 3: Sr, Nd and Pb isotopic compositions of basaltic rocks from the Dunedin Volcano. Initial ratios for Sr and Nd isotopic compositions are age-corrected at 13 Ma.

phase	type	amount of crystals removed from whole rock to achieve equilibrium (%)				Fo Ol Mg#Cpx An Pl Usp Timt	Temperature (°C)	Pressure (Mpa)	Melt water content (wt.%)	Oxygen fugacity (ΔFMQ; log units)	
		ol	cpx	pl	timt						
olivine	type 1			-		81-87	1180-1286				
	type 2			-		73-81	1134-1222				
clinopyroxene	type 1	5				61-82	1142-1186	498-789	1.9-3.1		
	type 1 mantles	2-5	2-4			65-81	1120-1158	423-754	2.5-3.3		
	type 2 (green cores)	2-5	4-6	0-10		43-69	1074-1128	351-693	0.8-1.8		
	type 3 (relic cores)			-		78-88	1209-1237	853-1059	2.5-3.5		
	type 4	0-5				68-84	1152-1197	532-808	2.5-3.3		
	type 4 mantles	0-5	0-3			69-83	1173-1202	585-774	2.6-3.4		
	Cr-recharge zones			-		74-87	1164-1208	579-907	2.5-3.3		
	overgrowth rims	5	2-6			63-81	1131-1175	381-691	1.9-3.1		
plagioclase	type 1 (cores)	5	10-20			43-68	1028-1094		1.8-3.0		
	type 1 (mantles)	3	5-15			60-84	1065-1123		1.4-3.0		
	type 2	2-4	10-15			40-78	1054-1096		1.4-2.2		
	type 3 (An-rich cores)					71-88					
titanomagnetite	High-alkali	5				0.44-0.79				-0.97	0.53
	Mid-alkali	0-5				0.58-0.91				-1.87	0.03
	Low-alkali	0-5				0.59-0.95				-2.18	-0.50
titanomagnetite-ilmenite	High-alkali									-0.26	0.12
	Low-alkali									-1.74	-1.13

Table 4. Summary of crystallization conditions estimated on the basis of experimentally calibrated thermometers, barometers, hygrometers and oxy-barometers for the different crystal populations in basaltic rocks of the Dunedin Volcano. Listed amounts of crystals have been used to model equilibrium melt compositions by subtracting them from whole rock compositions, in order to attain equilibrium between each crystal type and whole rock compositions. In each sample, mineral composition removed from the whole rock represents the average of crystal core compositions from the same sample. Further details on thermobarometry and mineral-melt equilibria in text.

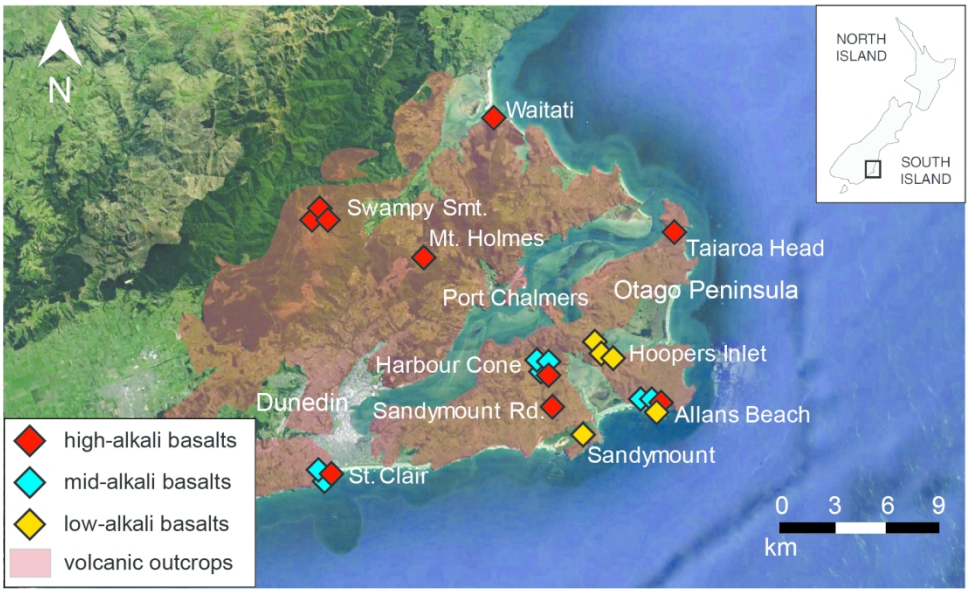

Fig. 1. Satellite photo of the Dunedin Volcano with sample locations and outlines of volcanic outcrops. Base image from Google Earth, Landsat, Copernicus, DigitalGlobe.

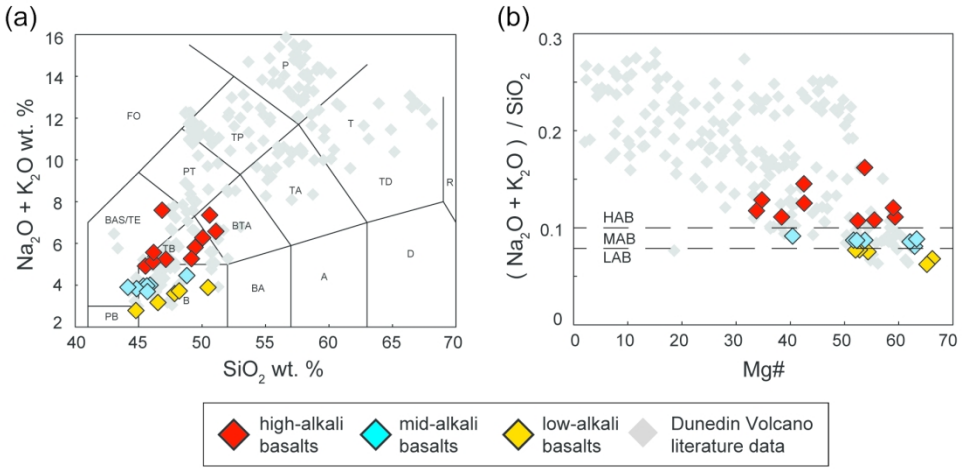

Fig. 2. Chemical classification of Dunedin Volcano basalts. (a) Total alkalis vs silica (TAS) classification (Le Maitre et al., 2002) of high-, mid-, and low-alkali basalts from this study. Literature whole rock compositions from Scott et al. (2020a) are plotted for comparison. (b) Alkali index [$(Na_2O+K_2O)/SiO_2$] vs. Mg# [molar 100 × Mg / (Mg + Fe^T)] diagram, used as criteria for classification of low-, mid-, and high-alkali basalts.

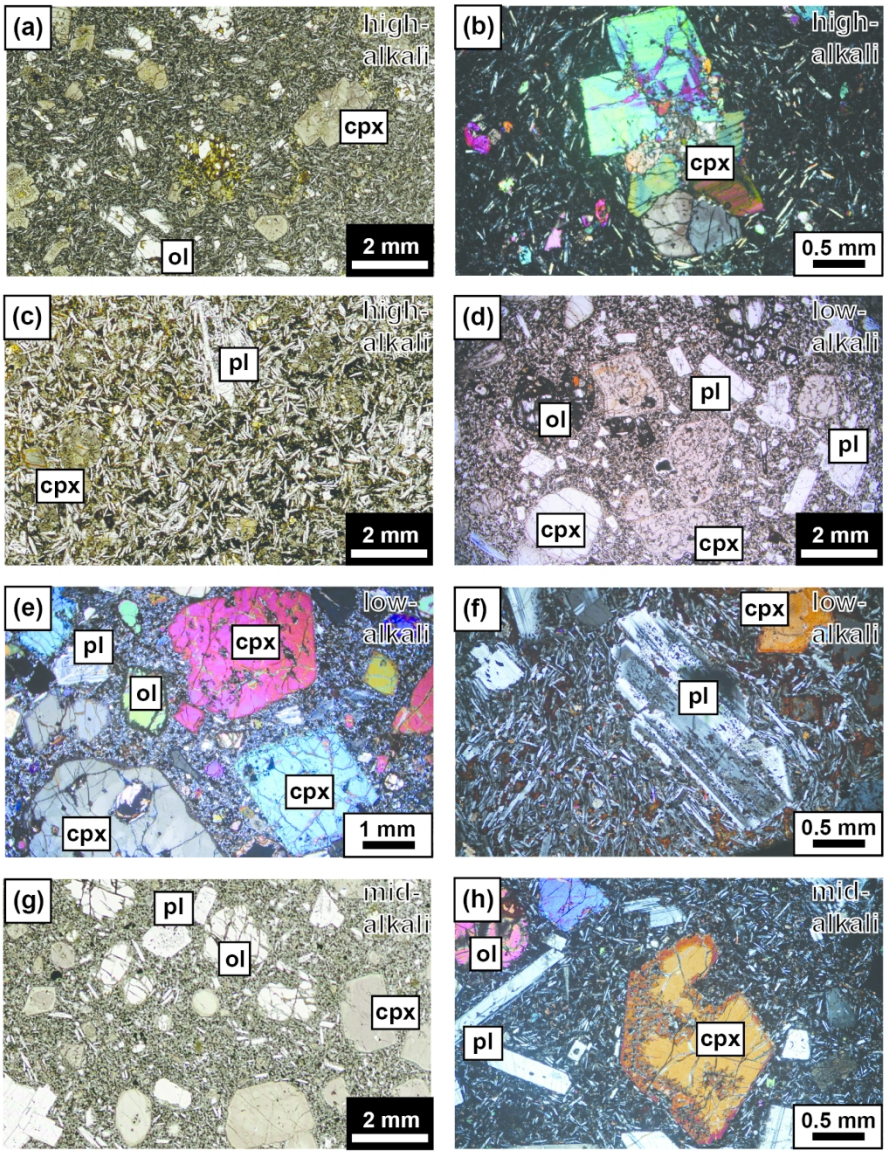

Fig. 3. Representative thin section photomicrographs in plane-polarised light (PPL) and cross-polarised light (XPL) of eruptive products at Dunedin Volcano. (a) High-alkali basalt (sample DVB1a) with main phenocryst assemblage including olivine, clinopyroxene and subordinate titanomagnetite, in a groundmass of plagioclase, clinopyroxene, titanomagnetite, and minor olivine (PPL) and (b) glomerocryst of clinopyroxene with prominent sector (hourglass) and oscillatory zoning (XPL). (c) High-alkali basalt (sample DVB2c) with clinopyroxene and plagioclase phenocrysts, in a groundmass of abundant plagioclase, clinopyroxene, and titanomagnetite (PPL). (d) Low-alkali basalt (sample DVB5b) with phenocrysts of light grey cores and pink clinopyroxene crystals, olivine, plagioclase, and titanomagnetite, with plagioclase crystals displaying sieve-textured mantles, in a groundmass of plagioclase, clinopyroxene, olivine and titanomagnetite (PPL). (e) Large clinopyroxene crystals in low-alkali basalt (sample DVB7) display either patchy interiors and/or patchy overgrowth rims. Light grey cores are recognizable by low birefringence, have more homogeneous interiors and resorbed inner rims (XPL). (f) Plagioclase phenocrysts in low-alkali basalt (sample DVB5a) with resorbed cores and sieve-textured mantle (XPL). (g) Mid-alkali basalt (sample DVB4a) with similar textural features to LABs, with a phenocryst assemblage of clinopyroxene with either pink or grey cores, plagioclase with

resorbed interiors, olivine and titanomagnetite, in a groundmass made by the same phase assemblage (PPL). (h) Large clinopyroxene crystal with homogeneous interior and patchy overgrowths in a mid-alkali basalt (sample DVB4c) (XPL).

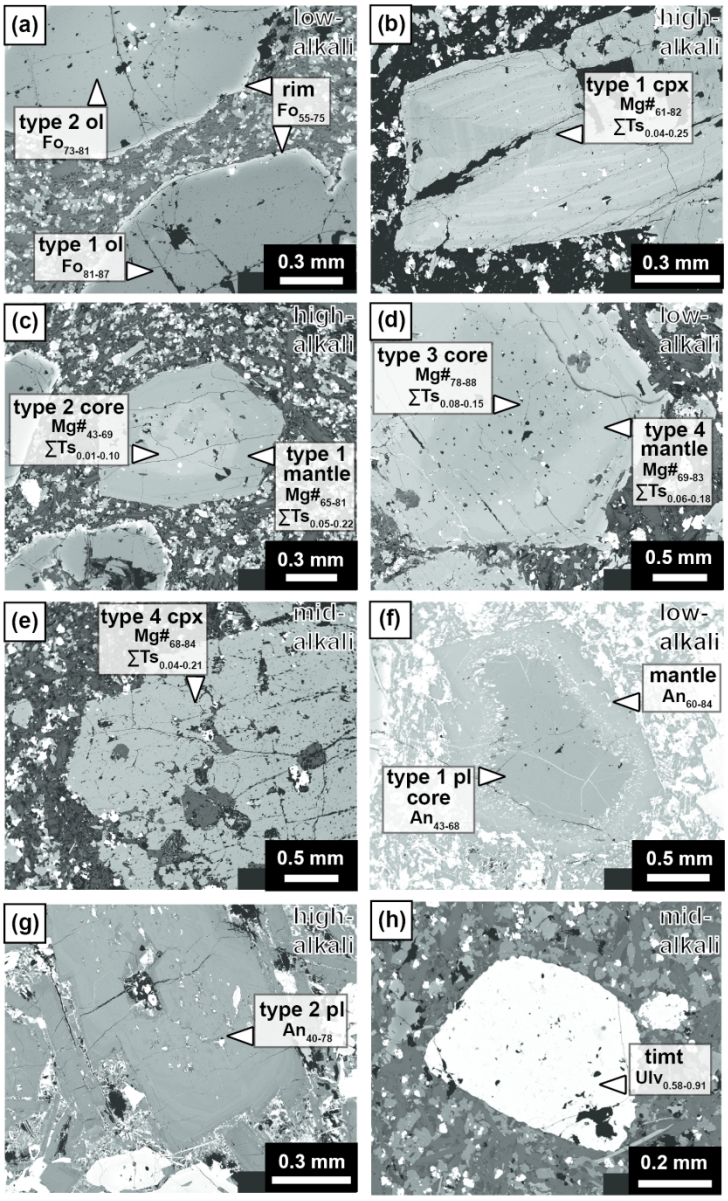

Fig. 4. Backscattered electron (BSE) photomicrographs of main phenocryst types from high-, mid-, and low-alkali basalts at Dunedin Volcano. (a) Olivine crystals from low-alkali basalt sample DVB5b, including darker type 1 Fo-rich olivine, sharing same compositional features as olivine from high-alkali basalts, along with brighter type 2 Fo-poor olivine. (b) Clinopyroxene type 1 in high-alkali basalt sample DVB1b showing oscillatory and sector (hourglass) zoning. A dark (Mg and Cr-rich) band (Cr-recharge zone) is overgrown by a brighter (Al and Ti-rich) rim. (c) Green clinopyroxene resorbed core type 2, overgrown by type 1 zoned mantle in high-alkali basalt sample DVB2c. (d) Mg- and Cr-rich clinopyroxene resorbed type 3 core from low-alkali basalt sample DVB5a, overgrown by mantle having clinopyroxene type 4 mantle, a darker Cr-recharge zone and a brighter overgrowth rim. (e) Uniform clinopyroxene type 4 in mid-alkali basalt sample DVB4a. (f) An-poor resorbed core, overgrown by an almost euhedral An-rich rim, in low-alkali basalt sample DVB5b. (g) Plagioclase crystal with oscillatory zoning and An content decreasing towards the rim (type 2) from high-alkali basalt sample DVB4d. (h) Titanomagnetite phenocryst from mid-alkali basalt sample DVB2b.

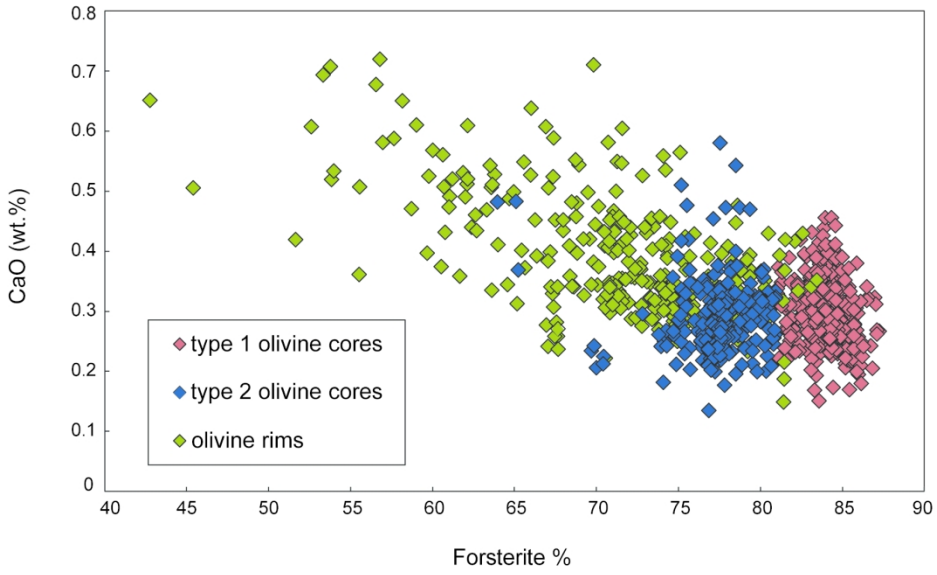

Fig. 5. Compositional characterization of olivine phenocrysts in the Dunedin Volcano. Type 1 olivines have unzoned to normally zoned forsterite-rich compositions (Fo_{81-87}), while type 2 crystals are unzoned to inversely zoned with forsterite-poor compositions (Fo_{73-81}), and rim compositions of both olivine types have the lowest forsterite contents (Fo_{55-75}).

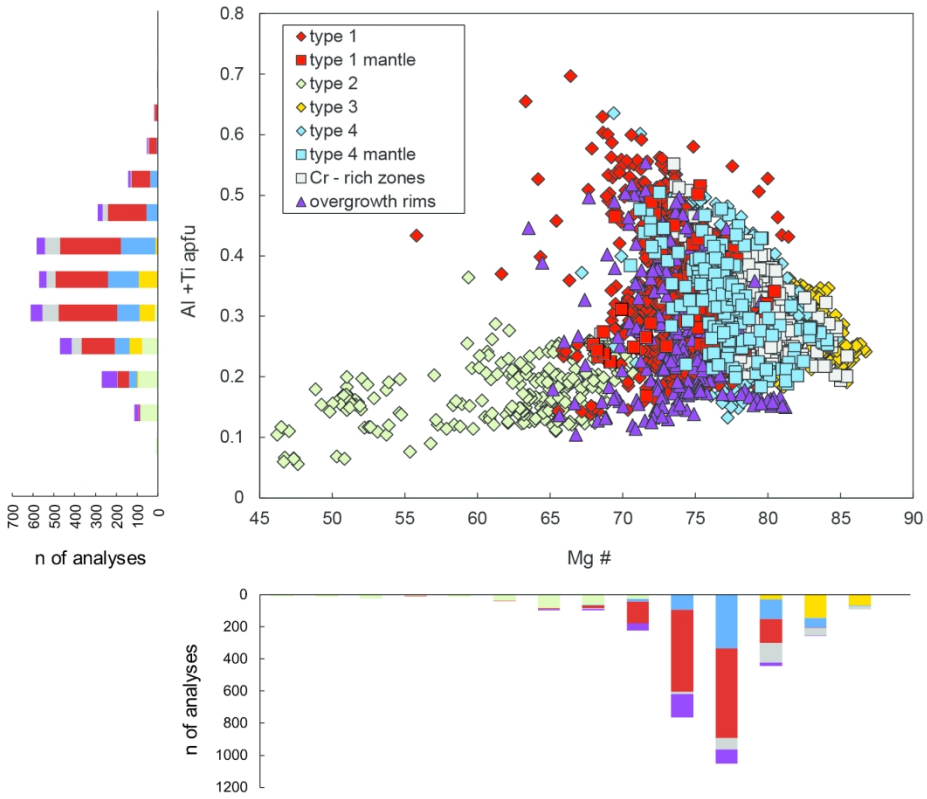

Fig. 6. Compositional characterization of clinopyroxene phenocrysts in basaltic rocks of the Dunedin Volcano in Al+Ti (apfu: atoms per formula units) vs. Mg# [molar 100 × Mg / (Mg + FeT)] compositional space, including frequency histograms.

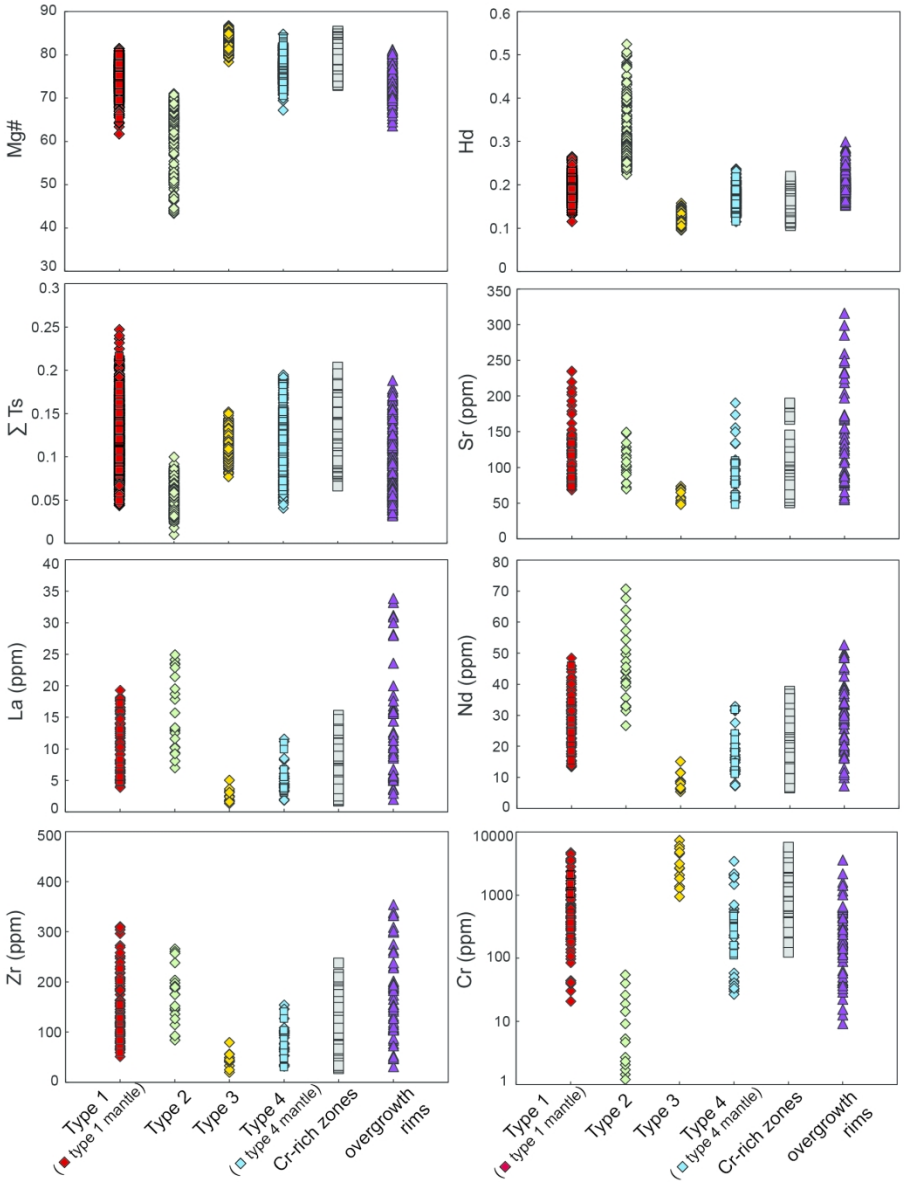

Fig. 7. Compositional variations of selected major elements, end-member components and trace elements in clinopyroxene populations in basaltic rocks of the Dunedin Volcano. Note that the scale for Cr is logarithmic, due to the very large variations in the abundance of this element (Mg# [molar 100 × Mg / (Mg + Fe^T)]; Hd: Hedenbergite; ∑Ts: CaTi-Tschermak + CaFe-Tschermak + CaCr-Tschermak).

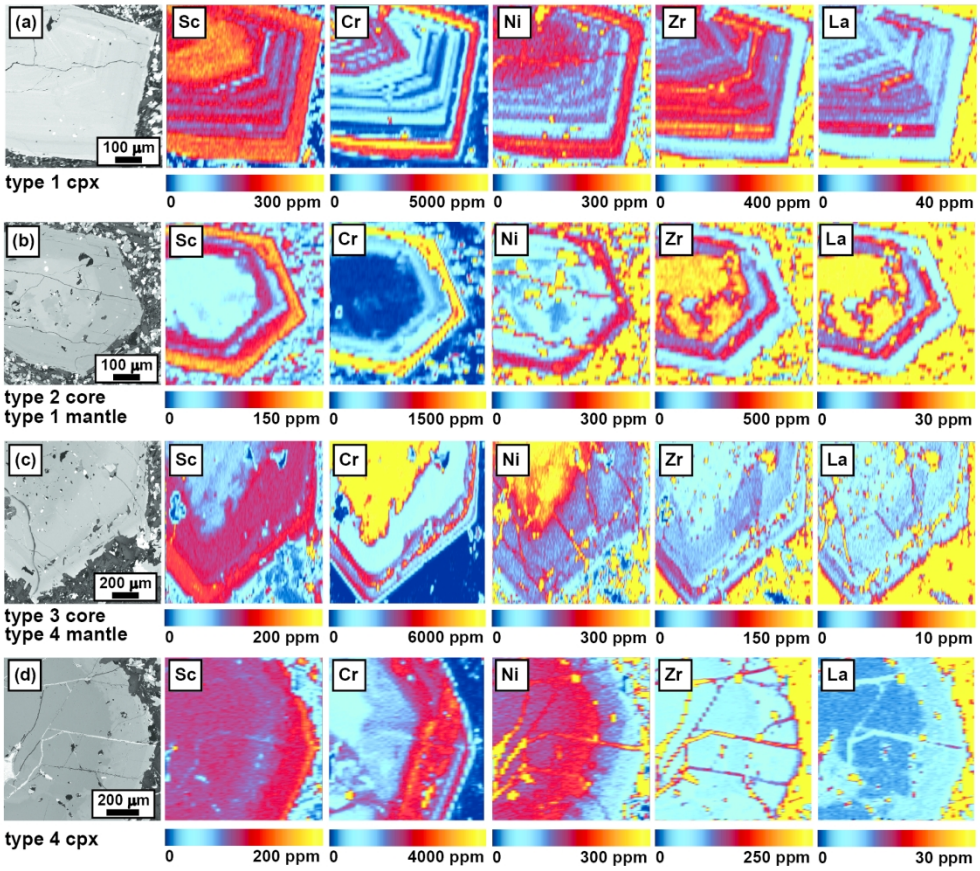

Fig. 8. Laser ablation inductively coupled plasma mass spectrometry (LA-ICP-MS) trace element maps of clinopyroxene populations in basaltic rocks of the Dunedin Volcano. Selected trace element concentrations are shown with cool-warm colour scales. The maps are quantitative for clinopyroxene and semi-quantitative for other phases (inclusions and groundmass). (a) Type 1 clinopyroxene, characterised by oscillatory and sector (hourglass) zoning, with La and Zr enrichments in prism sectors. Oscillatory zoning determines large variations in Sc, Zr and La. A prominent Cr-rich zone is also evident, corresponding to a darker (diopside-rich) growth horizon in the BSE photomicrograph. (b) Green core clinopyroxene (type 2), characterised by low abundances of Cr, Ni, and Sc, and high abundances of Zr and La. The green core is overgrown by a type 1 zoned mantle, displaying large variations in Sc, Zr and La. The crystal also features a Cr-rich zone towards the crystal outer rim, also enriched in Ni. (c) Mafic resorbed core (type 3) enriched in diopside and compatible trace elements, overgrown by a titanaugitic type 4 mantle, uniform in composition and relatively poor in Zr and La, and then a Cr- rich zone. (d) Type 4 clinopyroxene, showing faint core to rim zoning. Cr increases in the outer interior and inner rim of the crystal, whereas Ni shows an overall decrease from core to overgrowth rim.

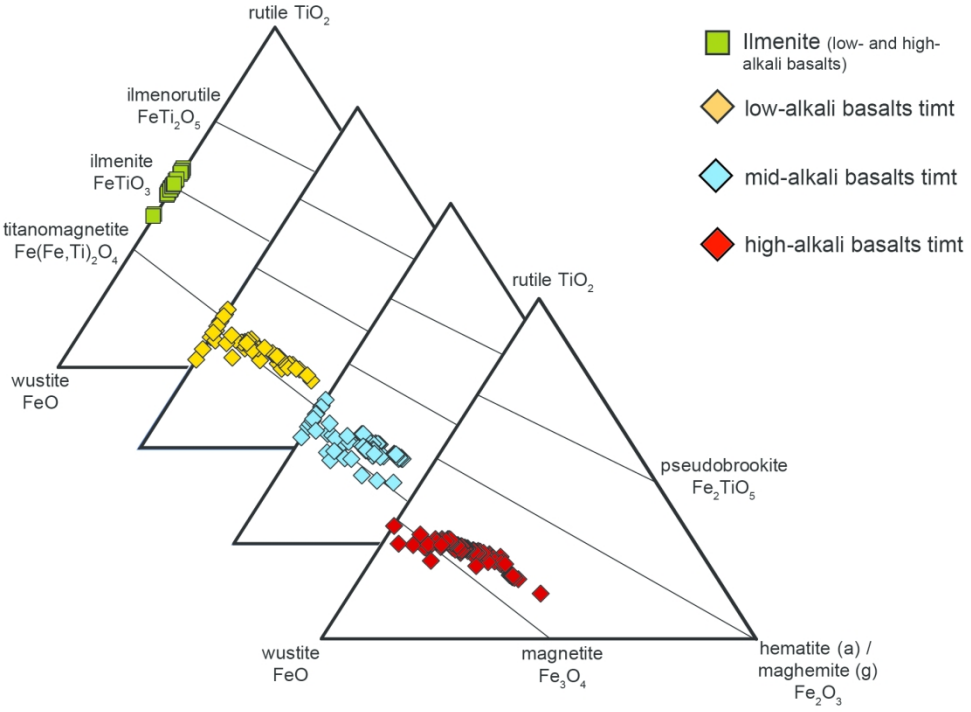

Fig. 9. Chemical classification of Fe-Ti oxide phenocrysts in Dunedin Volcano high-, mid- and low-alkali basalt samples.

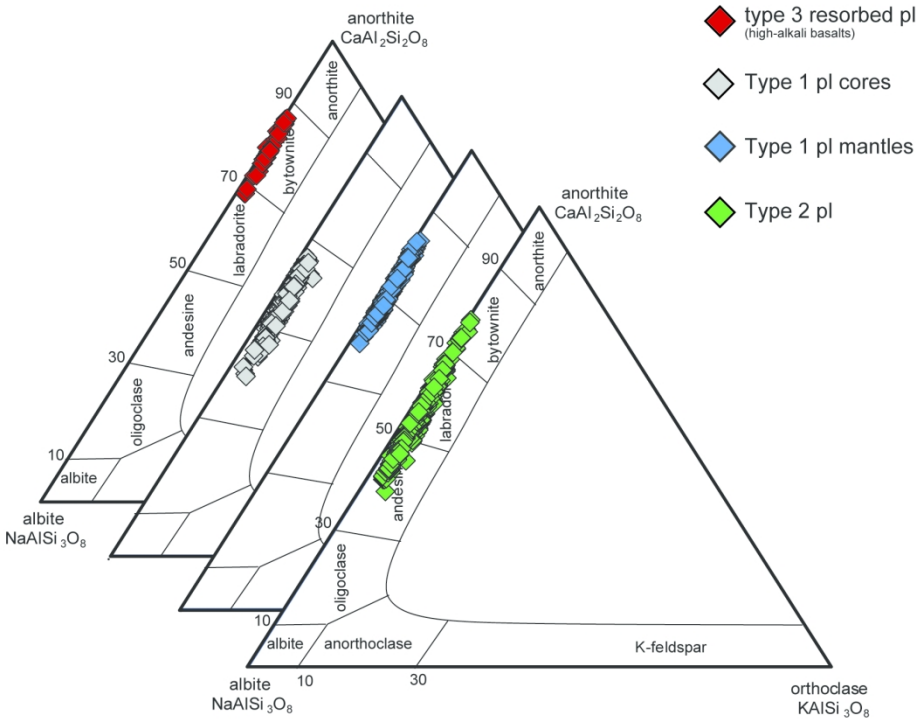

Fig. 10. Compositional classification of plagioclase phenocrysts in Dunedin Volcano basaltic samples, plotted in terms of relative proportions of Anorthite, Albite and Orthoclase components.

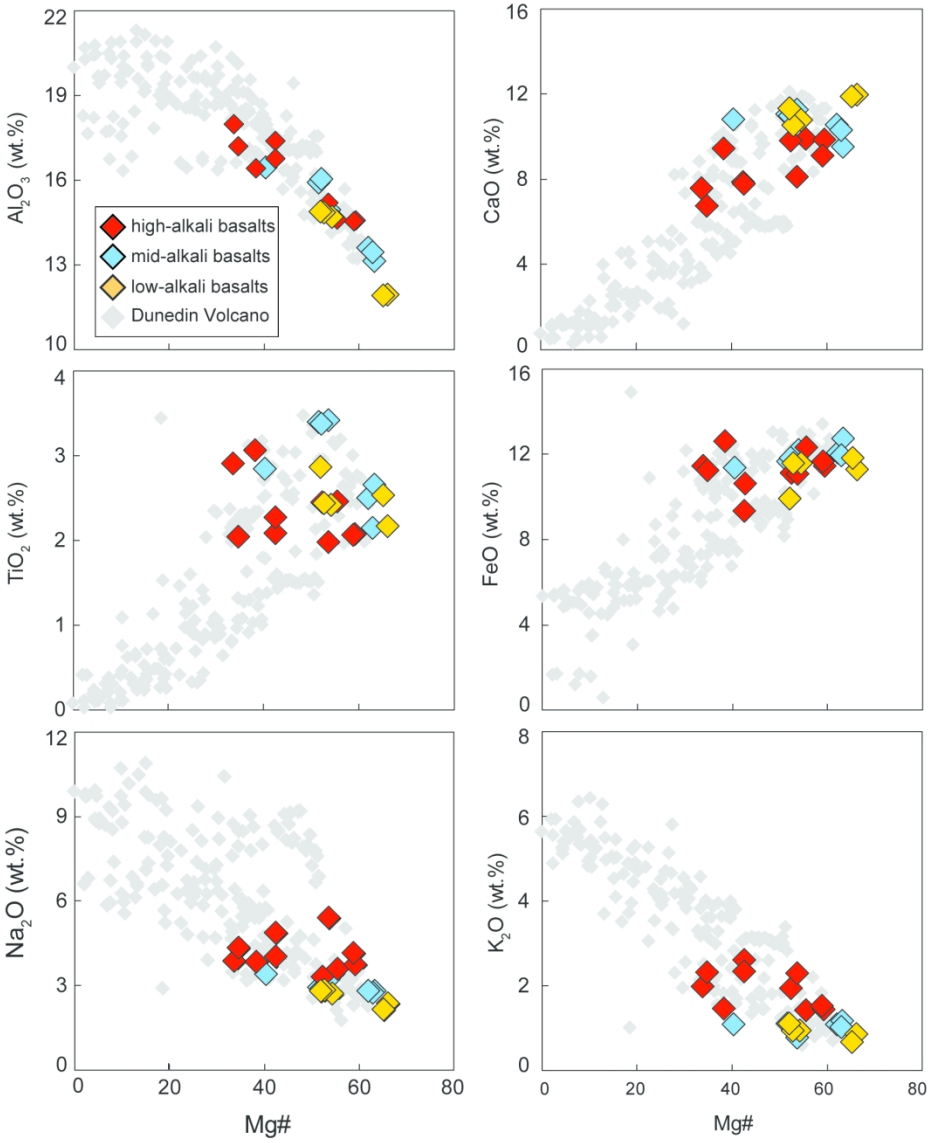

Fig. 11. Selected major elements vs. Mg# variation diagrams for Dunedin Volcano whole rock data. Literature data from Scott et al. (2020a) are shown for comparison.

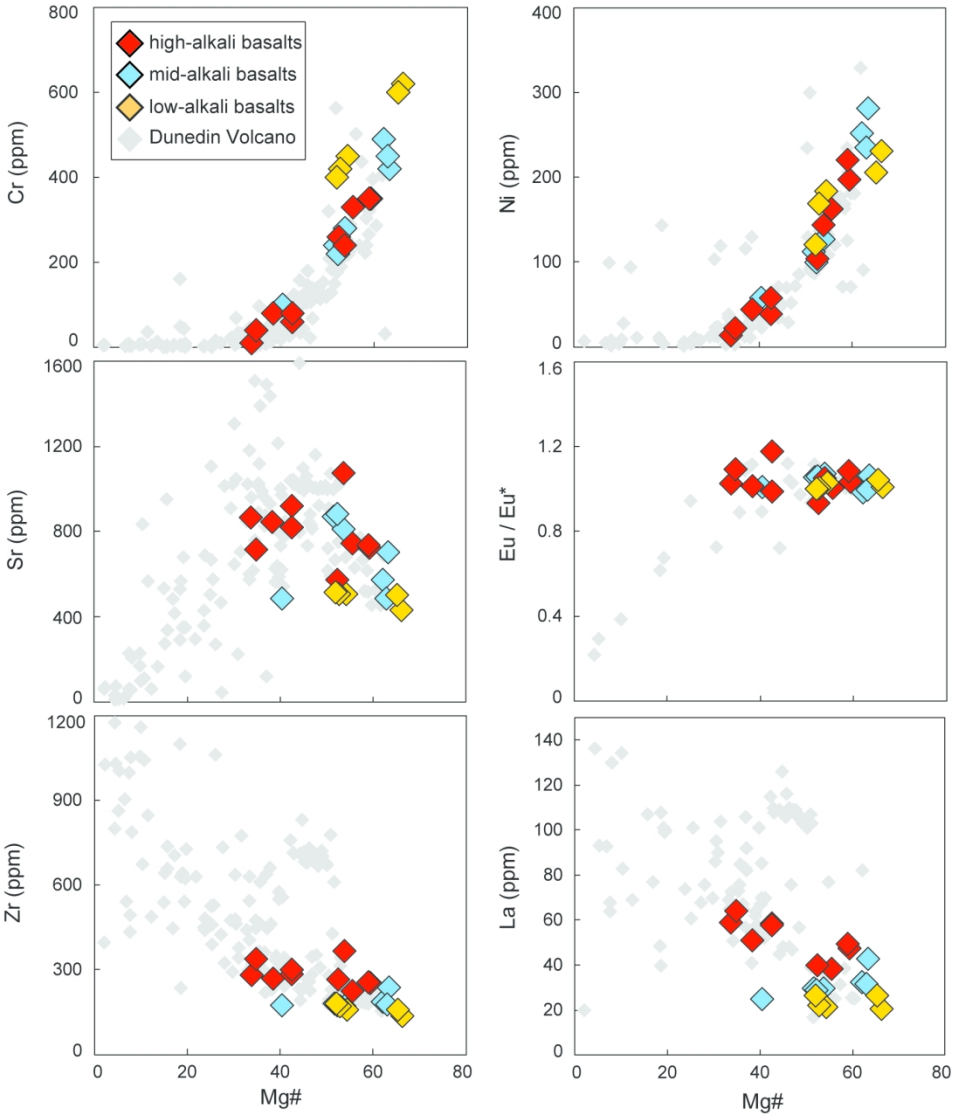

Fig. 12. Selected trace elements vs. Mg# variation diagrams for Dunedin Volcano whole rock data. Literature data from Scott et al., 2020a are shown for comparison.

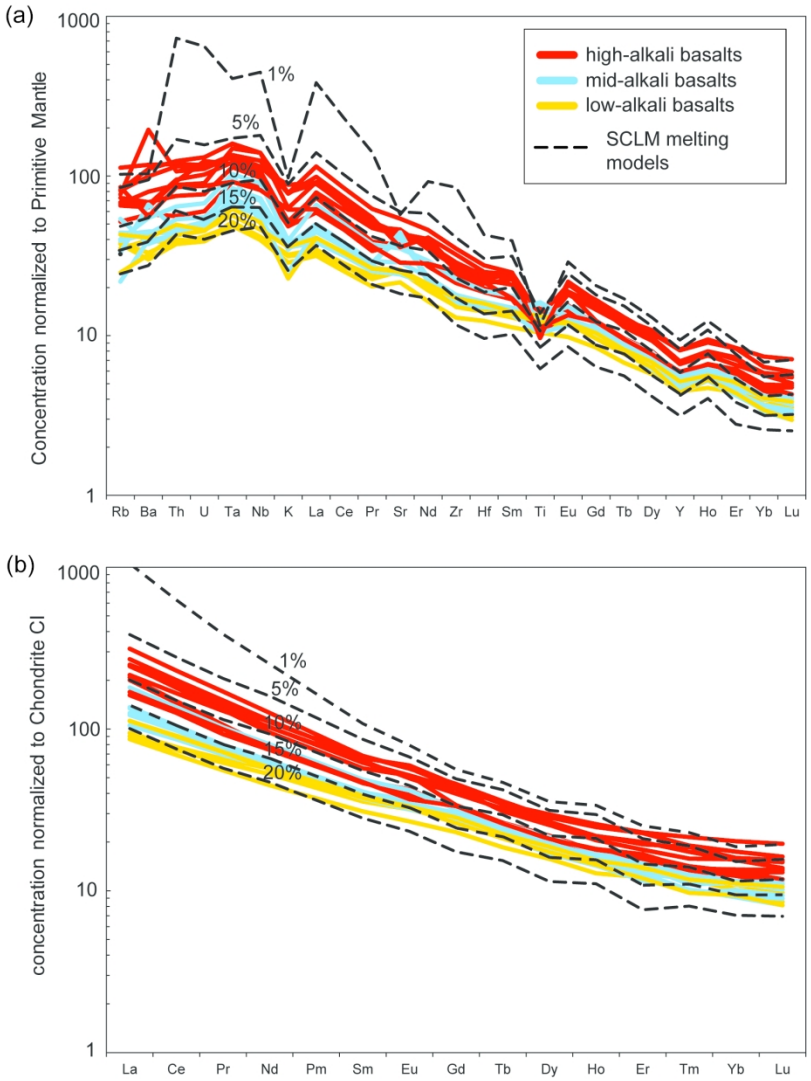

Fig. 13. (a) Primitive mantle normalised extended element plot for basaltic rocks of the Dunedin Volcano. Primitive mantle normalization values are from McDonough & Sun (1995). (b) Chondrite normalised REE plots for basaltic rocks of the Dunedin Volcano. Data normalised to chondrite CI of McDonough & Sun (1995). Results of non-modal batch melting models of metasomatised lithospheric mantle are shown with labels indicating extent of partial melting (%) (further details in text and Table S9).

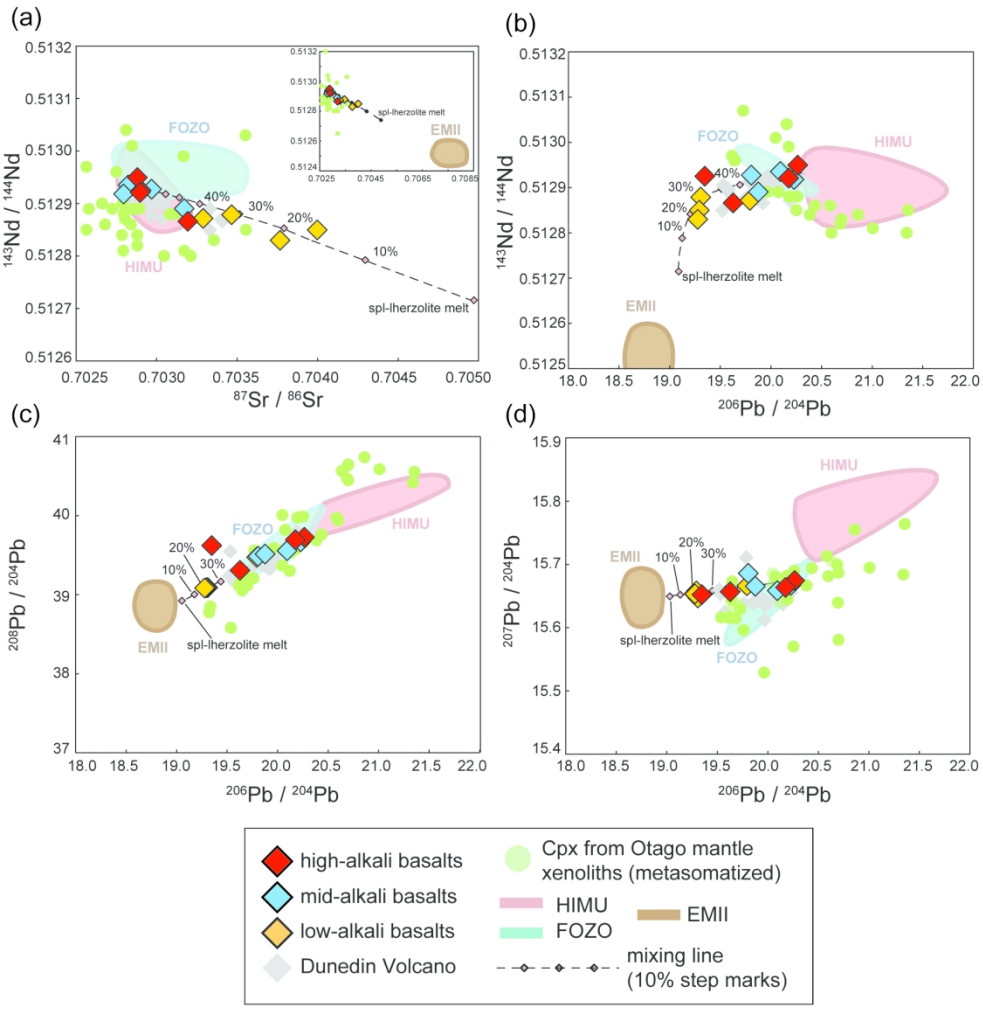

Fig. 14. Isotopic compositions of whole rocks from this study. Literature data from Scott et al. (2014a, 2014b, 2020a). HIMU and FOZO (young-HIMU) isotopic compositional fields are from Stracke et al. (2005), EMII fields are from Hart (1988) and Hart et al. (1992). Mixing lines between high- and mid-alkali basalts (sample DVB1a) and the hypothetical EMII-like composition of the asthenospheric mantle source (Table S9) are shown with 10% step mixing marks.

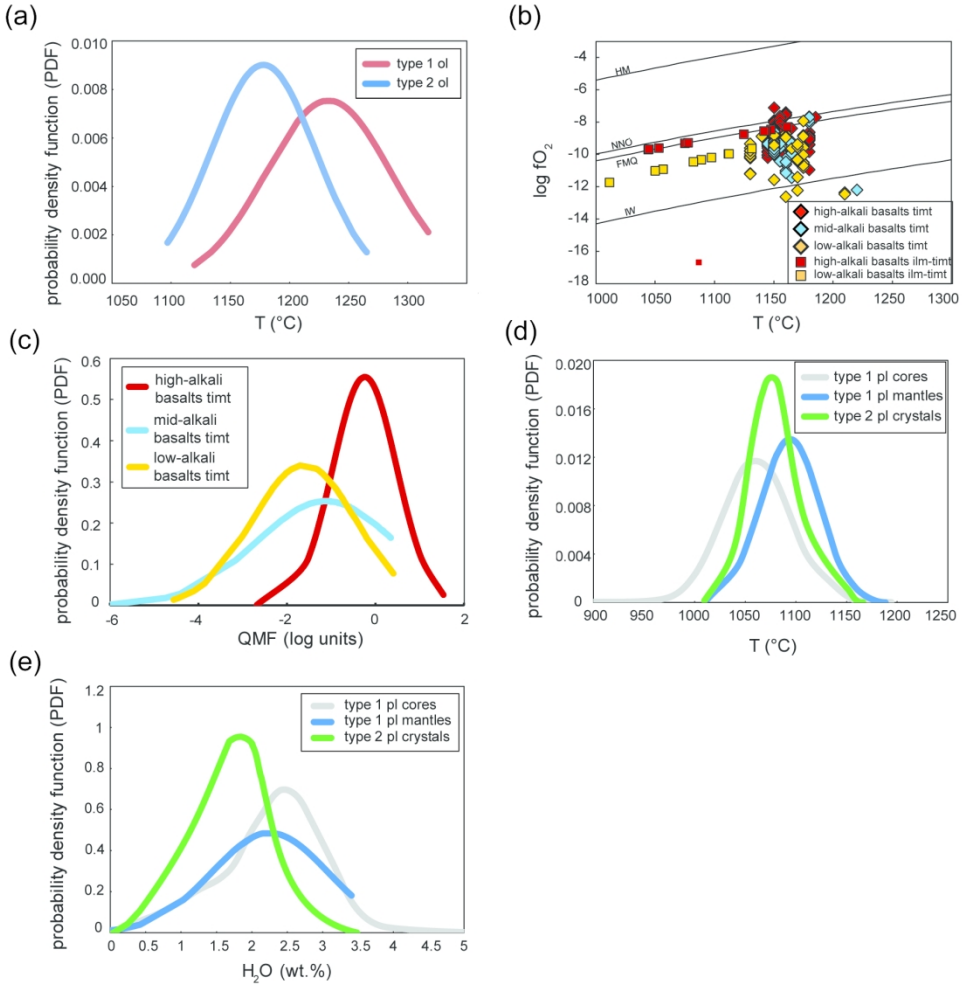

Fig. 15. (a) Probability density functions (PDF) of olivine-based temperature estimates calculated with the model of Pu et al. (2017). PDF represent the relative likelihood of the sample having a certain temperature value. (b) Temperature vs. fO_2 for oxide phenocrysts calculated with the model of Aryaeva et al. (2018). (c) PDF of oxygen fugacity estimates are expressed as log units above and below the Fayalite-Magnetite-Quartz (FMQ) buffer. (d) Plagioclase-based temperature calculated with the model of Putirka (2005). (e) Melt-H_2O contents estimated for melts in equilibrium with plagioclase phenocrysts by using the model of Putirka (2005).

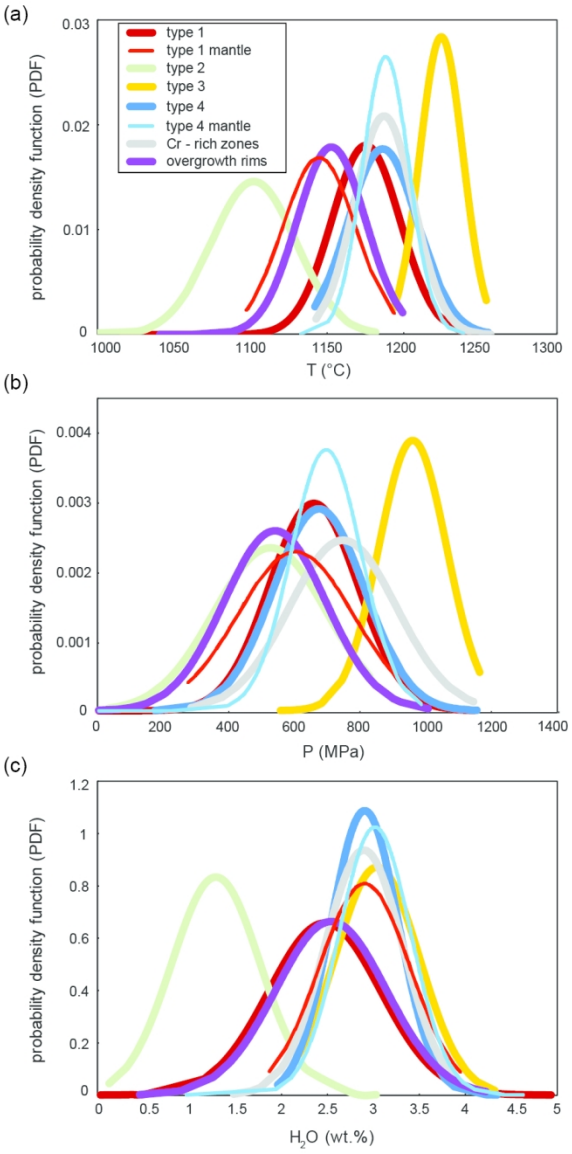

Fig. 16. (a) Probability density functions (PDF) of clinopyroxene-based temperature and (b) pressure estimates obtained using the thermobarometer of Putirka et al. (2003). (c) Melt-H_2O contents equilibrium with clinopyroxene have been estimated using the model of Perinelli et al. (2016).

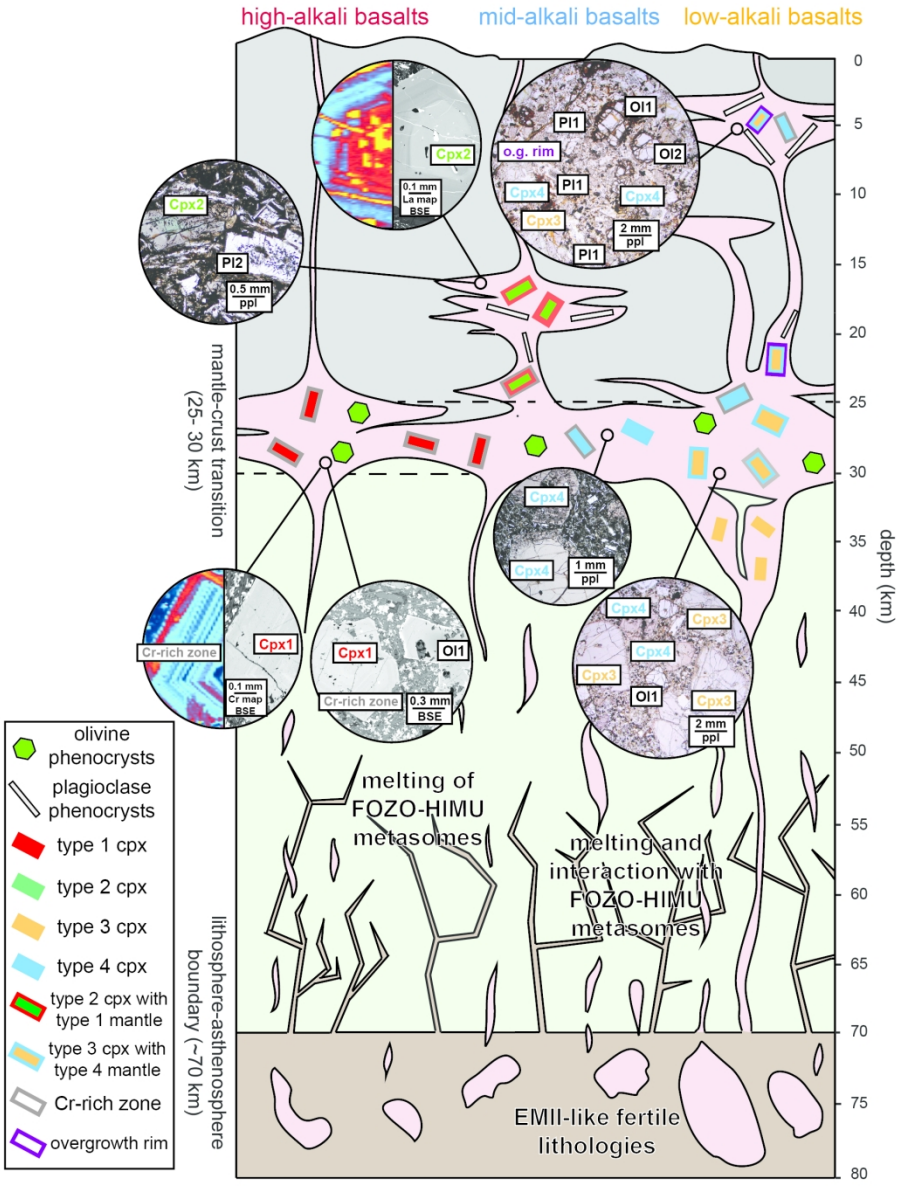

Fig. 17. Schematic representation of the complex plumbing system envisaged for the Dunedin Volcano. Different clinopyroxene types are distinguished according to the colour legend, while no colour distinctions are made for olivine and plagioclase crystals. Inset BSE photomicrographs and trace elements maps display the main textural features of low-, mid-, and high-alkali basalts. From left to right, higher degrees of interaction between asthenospheric derived melts and the lithospheric mantle generate peripheral high-alkali basalts. The increasing petrographic complexity of the crystalline cargo, with clinopyroxene green core type 2 and plagioclase type 2 from high- and mid-alkali basalts indicates the increasing development of the plumbing system at middle crustal depths, in the central sectors of the Dunedin Volcano. To the right, the central area of the volcano where low- and mid-alkali basalts were erupted, displays more complex mantle to crust pathways, fed by inputs of asthenosphere-derived EMII-like melts.

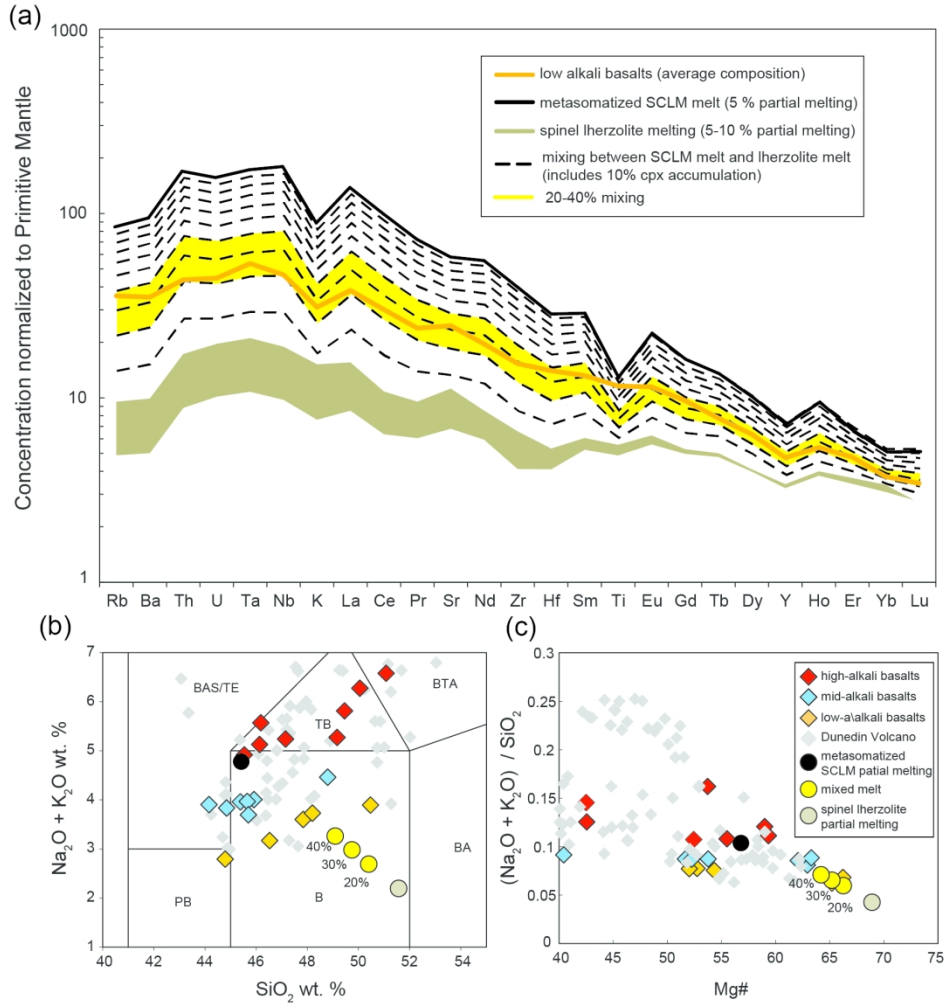

Fig. 18. Fertile peridotite partial melting and interaction model between the asthenospheric melts and the lithospheric wall-rock, aimed at reproducing the hypothesised asthenospheric mantle-derived primary magma, responsible for the EMII-like signature of low-alkali basalts at Dunedin Volcano. Interaction is best simulated by mixing the products of 5-10% lherzolite partial melting with 20-40% of the metasomatised lithospheric mantle melt (5% degree of partial melting), considering entrainment of 10% excess clinopyroxene in the resulting magma after interaction. (a) Primitive mantle normalised trace element concentrations of low-alkali basalts (averaged composition), SCLM-derived melt (as in Fig. 14a), fertile peridotite melt and mixed melt (dashed lines every 10% step of mixing; yellow field defines 20-40% mixing interval). (b) Total Alkali vs Silica (Le Maitre et al., 2002) plot and (c) alkali index [(Na_2O + K_2O)/SiO_2] vs Mg# display major element compositions of the primary magmas reconstructed for the Dunedin Volcano and the mixed magmas at 20%, 30% and 40% of lithospheric contribution. Further details in text and Table S9.